

AN ABSTRACT OF THE THESIS OF

AUGUSTINE J. SMITH for the degree of DOCTOR OF PHILOSOPHY

in PHYSICS presented on September 14, 1977

Title: TIME-OF-FLIGHT STUDIES OF HIGH RYDBERG STATES IN
ATOMIC LITHIUM EXCITED BY ELECTRON IMPACT

Redacted for privacy

Abstract approved: _____

Carl A. Kocher _____

A thermal beam of lithium atoms excited to high Rydberg states by pulsed electron impact has been studied by time-of-flight analysis. Near the end of a 35-cm field-free flight path, the excited atoms pass through a pair of electric field plates before entering an excited-atom detector. Electric field ionization was used for detection as well as state selection. Time-of-flight spectra obtained with applied electric fields up to 5 kV/cm are similar to the transit-time distribution for a non-decaying thermal beam, and yield lifetimes which are consistent with the presence of high angular momentum states in the beam. Angular-momentum-mixing cross sections were estimated to be of the order 10^{-13} cm^2 , by fitting observed transit-time distributions in the presence of introduced target gases with a model in which all angular momentum substates are equally likely, and in which arbitrary angular momentum changes are allowed.

With He, Ne, Ar, H₂, and N₂ introduced as target gases at pressures up to 4×10^{-4} Torr, cross sections for the scattering of the Rydberg atoms were obtained. These cross sections were typically 10^{-14} cm², apparently independent of the Rydberg electron state, and inversely proportional to the excited-atom velocity. These observations are in agreement with calculations based on a free core-ion deflection model, for which this study appears to be the first experimental verification. Measured cross sections for Rydberg atom interactions with NH₃ were found to be about 10^{-12} cm² and consistent with previous measurements and a theory in which the Rydberg atom is ionized after gaining energy from thermally excited rotational levels of the target molecule. The experimental technique of this study suggests a new method for slow ion investigations.

Time-of-Flight Studies of High Rydberg States in
Atomic Lithium Excited by Electron Impact

by

Augustine J. Smith

A THESIS

submitted to

Oregon State University

in partial fulfillment of
the requirements for the
degree of

Doctor of Philosophy

June 1978

APPROVED:

Redacted for privacy

Assistant Professor of Physics

in charge of major

Redacted for privacy

Chairman of Department of Physics

Redacted for privacy

Dean of Graduate School

Date thesis is presented _____ September 14, 1977

Typed by Clover Redfern for _____ Augustine J. Smith

ACKNOWLEDGMENT

I welcome this opportunity to express my sincere gratitude to all those who contributed to this thesis. It has been my privilege to work with Dr. Carl A. Kocher, an excellent thesis adviser and an equally good teacher. With pleasure I acknowledge his guidance, encouragement and help throughout this research and in the preparation of the thesis. I thank Professor David S. Burch for carefully reading the manuscript and Professor Charles W. Drake for the generous loan of equipment. I am indebted to the faculty of the Physics Department for many useful discussions, and to the technical staff for frequent assistance during the course of this work. I am also grateful to Alyson MacDonald for clerical assistance and to Linda Johnson and June Yee for moral support. This work was supported in part by Research Corporation. An Un-sponsored Research Grant from the O. S. U. Computer Center was very valuable in data analysis. The International Atomic Energy Agency, in collaboration with the National Science Foundation, provided me with the initial opportunity to study at O. S. U. Finally, I wish to express my appreciation to all my friends who have helped make my stay in the United States a pleasant one.

TABLE OF CONTENTS

Chapter	Page
1. INTRODUCTION	1
2. PROPERTIES OF HIGH RYDBERG ATOMS	8
2.1 Energy Levels	8
2.2 Field Ionization	11
2.3 Radiative Lifetimes	18
2.4 Excitation	26
2.5 Collisions	31
2.6 Detection	37
3. THEORY OF THE EXPERIMENT	39
3.1 Time-of-Flight Spectra with Applied Electric Fields	39
3.2 Ionization Probability in High Rydberg Collisions with Neutral Atoms	46
3.3 Ion-Atom Scattering	50
3.4 Model for Time-of-Flight Distributions with Introduced Target Gases	59
4. APPARATUS	66
4.1 Vacuum System	66
4.2 Atomic Beam Oven	70
4.3 Electron Gun	72
4.4 State Selector	73
4.5 Excited-Atom Detector	75
4.6 Signal Electronics	78
4.7 Preparations for a Run	81
5. EXPERIMENTAL PROCEDURES	83
5.1 Preliminary Measurements	83
5.2 Time-of-Flight Spectra	88
5.3 Lifetime and Collision Measurements	89
6. RESULTS, ANALYSIS AND INTERPRETATION	93
6.1 Lifetime Measurements	93
6.2 Determination of Collision Cross Sections	104
6.3 Angular-Momentum-Mixing Collisions	126
6.4 Summary of Conclusions	142
6.5 Suggestions for Further Study	144
BIBLIOGRAPHY	146
APPENDIX	151

LIST OF TABLES

Table	Page
1. Measured ionization-gauge correction factors f for target gases used in this experiment and for air.	69
2. Experimental and calculated values of σv for the five target gases.	123
3. Experimental values of $\ln F_{\max}$, obtained from the maxima of channel-by-channel ratio intercepts.	132
4. Angular-momentum-mixing cross sections $\sigma^{\Delta l}$ calculated from the complete model, using the three decay models for the $n = 30$ state of lithium (Figure 33) and observed values of $\ln F_{\max}$.	138

LIST OF FIGURES

<u>Figure</u>	<u>Page</u>
1. A high Rydberg atom in an external electric field.	12
2. Field ionization thresholds for hydrogen.	15
3. Variation of hydrogenic lifetimes with n and l .	19
4. Radiative decay rates for lithium.	22
5. The vacuum system.	67
6. The atomic beam oven and electron gun.	71
7. Electric field plates and detector configuration.	74
8. Channeltron bias circuit.	76
9. Experimental configuration.	79
10. A detector used for dc measurements.	85
11. Lithium excitation function.	86
12. A typical time-of-flight spectrum.	90
13. Semi-log plot of time-of-flight spectra recorded at electric fields 0 and 2.8 kV/cm.	94
14. Survival probability and decay rates for high Rydberg lithium atoms at various electric fields.	97
15. Channel-by-channel ratios of time-of-flight spectra obtained at 0.5, 1.0 and 2.8 kV/cm.	100
16. Semi-log plot of time-of-flight recorded at several neon pressures.	105
17. Channel-by-channel ratios for neon at 0 V/cm.	108
18. Channel-by-channel ratios for neon at 200 V/cm.	109
19. Channel-by-channel ratios for neon at 1000 V/cm.	110

<u>Figure</u>	<u>Page</u>
20. Channel-by-channel ratios for helium at 200 V/cm.	111
21. Channel-by-channel ratios for argon at 200 V/cm.	112
22. Channel-by-channel ratios for nitrogen at 200 V/cm.	113
23. Channel-by-channel ratios for hydrogen at 200 V/cm.	114
24. Channel-by-channel ratios for ammonia at 0 V/cm.	115
25. Slopes of \ln [channel-by-channel ratios] for helium.	116
26. Slopes of \ln [channel-by-channel ratios] for neon.	117
27. Slopes of \ln [channel-by-channel ratios] for argon.	118
28. Slopes of \ln [channel-by-channel ratios] for hydrogen.	119
29. Slopes of \ln [channel-by-channel ratios] for nitrogen.	120
30. Slopes of \ln [channel-by-channel ratios] for ammonia.	125
31. Logarithm of ratios of counting rates as functions of helium pressure.	128
32. Intercepts $\ln F_{\infty}(p)$ of \ln [channel-by-channel ratios].	131
33. Three models for the variation of the radiative decay rate of lithium in the state with $n = 30$.	136
34. Fits of $\ln[F(t)]$ for neon data at 200 V/cm.	139

Appendix

A1. A sample of the computer printout for $\ln F(t)$ calculated by the complete model.	156
A2. Computer plot of $\ln F(t)$ shown in Figure A1.	157
A3. Computer plots of $\ln F(t)$ calculated by the restricted model.	158

TIME-OF-FLIGHT STUDIES OF HIGH RYDBERG STATES IN ATOMIC LITHIUM EXCITED BY ELECTRON IMPACT

1. INTRODUCTION

A high Rydberg (HR) state of an atom or molecule is one in which one electron is in an excited state characterized by a large value of the principal quantum number n . The structure of these atoms or molecules is very similar to that of the hydrogen atom, since, to a good approximation, the excited electron may be regarded as moving in the Coulomb potential of a singly charged core-ion. In the limit of large quantum numbers, classical mechanics agrees well with quantum mechanics. It is therefore permissible to use the Bohr theory of the hydrogen atom to describe the gross structure of HR atoms. In the Bohr theory, electrons are assumed to move in Keplerian orbits about a nucleus (or a core-ion, in the case of HR systems). The orbits are quantized by the requirement that the orbital angular momentum be an integral multiple of Planck's constant. Each orbit corresponds to a definite amount of total energy, given for the n^{th} orbit by

$$E_n = - \frac{13.6 \text{ eV}}{n^2}, \quad (1.1)$$

and has a mean radius of

$$r_n = n^2 a_0, \quad (1.2)$$

where $a_0 = 5.3 \times 10^{-9}$ cm is the radius of the first Bohr orbit for the hydrogen atom. Thus it is seen that HR atoms are very large in size and very weakly bound. For example, at $n = 30$, a HR atom is about 1000 times as large as a normal atom, but is held together by only 15 meV, which is less than the average thermal kinetic energy of an atom at 300°K. In fact a HR atom is so fragile that when it passes through an electric field, the opposing forces on the excited electron and the core-ion can ionize it, provided it is in a sufficiently high- n state. High fields can ionize states with lower values of n , and it will be shown in Section 2.1 that for a given field there is a critical quantum number n_c such that states with $n \geq n_c$ are ionized, whereas those with $n < n_c$ are not ionized in the field. This field ionization phenomenon can be used not only to discriminate between Rydberg states with different values of n , but also to detect these Rydberg states.

From an experimental point of view, an important characteristic of HR atoms is their ability to remain excited for relatively long periods of time (compared to the typical lifetime of a lower-lying atomic state). One can gain some insight into this phenomenon by looking at the lifetimes of hydrogenic states in spontaneous decay. The lifetime of a hydrogenic state with a fixed value of the angular

momentum quantum number l is approximately proportional to n^3 for low values of l , and to n^5 for high- l values (B4). Thus it is seen that HR states with large principal quantum numbers n can remain excited long enough to traverse macroscopic distances even when their velocities are only thermal (10^5 cm/sec). Hence atomic beams of HR atoms can be formed and studied experimentally.

The existence of HR atoms was first predicted in 1884, when Balmer proposed an empirical formula for the wavelengths of the lines in the hydrogen spectrum. Experimental verification came soon afterwards when, in 1886, Cornu observed Balmer emission lines through $n = 13$, and when Pickering in 1893 observed stellar transitions with n up to 31. In 1906, Woods detected lines with n as large as 51 in the absorption spectrum of sodium.

Stark ionization was first detected in 1930 by von Traubenberg, Gebauer and Lewin (T1), who observed the disappearance of Balmer lines in strong electric fields. Lanczos (L1), using a WKB-type method, was able to interpret the results of Ref. T1. In 1934 Amaldi and Segrè (A1) conducted the first collision experiments involving HR atoms. They studied the shifts of high Rydberg lines in the absorption spectrum of sodium and potassium, due to rare gas collisions at high pressures. To explain these results, Fermi (F1) used a low energy electron scattering parameter, the scattering length, and thereby introduced the idea that in collisions the HR electron behaves

essentially as a free electron. This point of view still dominates theoretical studies of HR collisions.

The current interest in HR studies started in the early 1960's. Kardashev (K1), in 1959, predicted that recombination processes for interstellar hydrogen should lead to a well resolved spectrum. Such lines, with $n \cong 100$, were subsequently observed by Hoglund and Metzger (H1) using microwave techniques. In 1964 Riviere and Sweetman (R1) demonstrated the formation of HR atoms following charge exchange between fast protons and hydrogen atoms, and also the detection of HR atoms using field ionization. Today, field ionization techniques are widely used in HR studies. Apart from the charge exchange method used in Ref. R1, various other methods, such as electron impact excitation, dissociative excitation of molecules, and photoexcitation employing tuneable dye lasers, have been used in the production of HR atoms.

Several investigations of HR states of atoms and molecules have recently appeared in the literature. Motivation for these studies derives from various interests, among which may be listed applications of high Rydberg atoms in laser development, laser-induced isotope separation, energy deposition in gases, plasma diagnostics, physical-chemical analysis, and some basic atomic physics such as the determination of fundamental constants to improved accuracy. However, the intrinsic interest in the properties of these highly

excited states remains the primary motivation for their study.

These recent studies have led to a better understanding of the basic properties of HR atoms. For example, ionization of HR atoms in collisions with polar and electronegative molecules are well documented, and in collisions with electrons and neutral atoms and molecules the orbital angular momentum of the HR electron has been observed to change, the latter being inferred from changes in the lifetimes of the HR atom. Field ionization and radiative decay of HR atoms are also quite well understood. A review of these properties will be given in Chapter 2.

This thesis describes an experimental study of lithium atoms excited to high Rydberg states by electron impact. The method of study involves obtaining the transit-time distribution (time-of-flight spectrum) for a group of atoms traversing a 35-cm flight path after the atoms have been excited by an electron pulse of 5.5 μ sec duration. This technique is used because time-of-flight (TOF) spectra contain information concerning the velocity distribution in the atomic beam, in-flight radiative decay rates, and cross sections for collisions experienced by the atoms while in transit, as well as the velocity dependences of these cross sections. Lithium was chosen as the element of study because: 1) it has a low ionization potential; 2) highly excited lithium atoms have a closed shell core structure; 3) lithium can be obtained commercially in a high state of purity; and 4) it is

easy to form a beam of lithium atoms, using an atomic beam oven.

The results of these TOF measurements may be summarized as follows. TOF spectra obtained with applied electric fields up to 5.0 kV/cm yield lifetimes of high Rydberg lithium atoms (Li^*) which indicate that the atoms are predominantly in high angular momentum states, whereas electron impact is expected to excite s, p, and d states most efficiently. Spectra obtained with introduced target gases (helium, neon, argon, hydrogen and nitrogen, at pressures up to 4×10^{-4} Torr) yield total cross sections for the deflection of high Rydberg atoms during elastic collisions with these target gas species. The observed cross sections are apparently independent of the principal quantum number n of the high Rydberg state and are inversely proportional to the excited-atom velocity. Cross sections for angular momentum mixing are also obtained from these collision measurements.

A model is proposed which assumes that in HR collisions with neutral gas atoms, the core-ion and the very weakly interacting excited electron interact independently. Localized collisions between a target atom and the Rydberg electron lead to changes in the orbital angular momentum quantum number ℓ of the latter, whereas those collisions which primarily involve the core-ion lead to deflections of the HR atom. The model allows for in-flight radiative decay and for arbitrary ℓ -changes in ℓ -mixing processes. The predictions of this

model are consistent with the experimental results. To the best of the author's knowledge, the results presented in this thesis constitute the first experimental evidence supporting the localized core-ion interaction model for HR atoms.

Chapter 2 will be devoted to a review of the recent literature and the properties of HR atoms. No attempt has been made to write a comprehensive review. Instead, the author has included in Chapter 2 those studies which seemed relevant to this thesis. In Chapter 3, theoretical expressions are derived for the expected HR time-of-flight spectra, with applied electric fields and with admitted target gases. An expression for the total HR scattering cross section is also derived, and the HR collision model discussed. Chapters 4 and 5 contain a description of the experiment (apparatus and procedures). The observed time-of-flight spectra are presented in Chapter 5, and the experimental results are discussed in Chapter 6.

2. PROPERTIES OF HIGH RYDBERG ATOMS

In this chapter a review of the properties of high Rydberg (HR) atoms is given. The areas covered include energy levels, field ionization, radiative decay, collision processes, and methods for the production and detection of HR atoms. For each topic covered a review of recent literature is also given. Three excellent review articles on HR states have been published: Kleppner (K2), gives a historical perspective, while Stebbings (S1), discusses the basic properties, and Il'in (I1) reviews field ionization studies.

2.1 Energy Levels

High Rydberg states are characterized by a single electron excited to a high value of the principal quantum number n . The HR electron moves in the potential of a core-ion which has total charge $+e$. HR states are therefore expected to resemble the corresponding states of atomic hydrogen. However, the interaction between the excited and core electrons tends to modify the hydrogenic nature of HR states. The major contribution to this effect is the polarization of the core in the field of the outer electron. Thus, the energy levels of a state with a given n are no longer degenerate, as they are in the case of the hydrogen atom. Quantum defect theory may be used to describe the nature of HR energy levels. In this theory the binding

energy of the n^{th} principal quantum state is written in a manner similar to that in which hydrogenic levels are expressed:

$$E_n = -13.6/n^{*2} \text{ eV.} \quad (2.1)$$

Here n^* is an effective quantum number given by $n^* = n - \delta_\ell$, where δ_ℓ is the quantum defect of the ℓ^{th} angular momentum state. As indicated by the notation used, δ_ℓ is independent of n , depending only on ℓ . This is a major result of quantum defect theory. Quantum defects generally tend to be small numbers which provide a measure of the differences between energy levels of the hydrogen atom and those of many-electron atoms; they are largest for s and p states, becoming progressively smaller for higher ℓ -values. Quantum defect theory has been discussed by Seaton (S8).

For lithium, δ_ℓ for low values of ℓ may be obtained from tabulated energy levels (M1). For higher- ℓ values there are no such tabulations; however δ_ℓ can be obtained from theoretical considerations. The major contributing factor to quantum defect for these higher- ℓ values is polarization of the core ion. Edlén (E1) has developed formulae for calculating quantum defects for high ℓ which will be discussed in Section 3.1.

In recent experiments, Gallagher, Edelstein and Hill (G1, G2), have measured d-f-g-h splittings for sodium atoms in HR states

($11 \leq n \leq 17$). Their experimental procedure consisted of exciting sodium atoms (in a cell) to nd states using two laser photons: $3s$ to $3p$, then $3p$ to nd . A microwave signal then mixed the nd and nf states. The nd to $3p$ or the nf to $3d$ decay photons were monitored. The observed signal was corrected for nd cascades which occurred even when microwave power was not applied. The d to g and d to h transitions were observed by multiphoton resonances. The results indicate that the f , g and h fine-structure splittings are very nearly hydrogenic. Quantum defects for d and f states were also obtained.

Freeman and Kleppner (F2) have argued that high- ℓ quantum defects are due mostly to core-ion polarization by the excited electron. They have shown that the perturbation is of the form

$$V_{\text{pol}} = -\frac{1}{2} \alpha_D \left\langle \frac{1}{r^4} \right\rangle - \frac{1}{2} \alpha_Q \left\langle \frac{1}{r^6} \right\rangle, \quad (2.2)$$

where α_D and α_Q are dipole and quadrupole polarizabilities of the core-ion, and where r is the radial coordinate of the electron.

This perturbation leads to the quantum defect of the ℓ^{th} state

$$\delta_\ell = \frac{3}{4} \alpha_D \ell^{-5} + \frac{35}{16} \alpha_Q \ell^{-9}. \quad (2.3)$$

Using Equation 2.3 and the results of Reference G1 for sodium,

Freeman and Kleppner obtained the values 1.0015(15) and 0.48(15),

in units of a_0^3 and a_0^5 , for α_D and α_Q respectively. These values, however, are different from static polarizabilities, because of non-adiabatic effects.

2.2 Field Ionization

High Rydberg atoms have a tendency to ionize in electric fields. This phenomenon can be understood by a simplified one-dimensional model of a HR atom in a uniform electric field of magnitude F . The hydrogen atom is used as a model for the HR atom. As shown in Figure 1, the potential energy of the electron at a distance z from the nucleus is given by

$$V(z) = -\frac{e^2}{z} - eFz. \quad (2.4)$$

Here $e = 4.8 \times 10^{-10}$ esu is the charge of the electron. The potential energy has a maximum at $z = \sqrt{e/F}$ which is easily seen to be

$$V_{\max} = -2\sqrt{e^3 F}. \quad (2.5)$$

If Stark shifts are neglected, the state whose energy lies at the top of the barrier is seen to have a critical quantum number n_c given by

$$E_{n_c} = -\frac{13.6 \text{ eV}}{n_c^2} = -2\sqrt{e^3 F}. \quad (2.6)$$

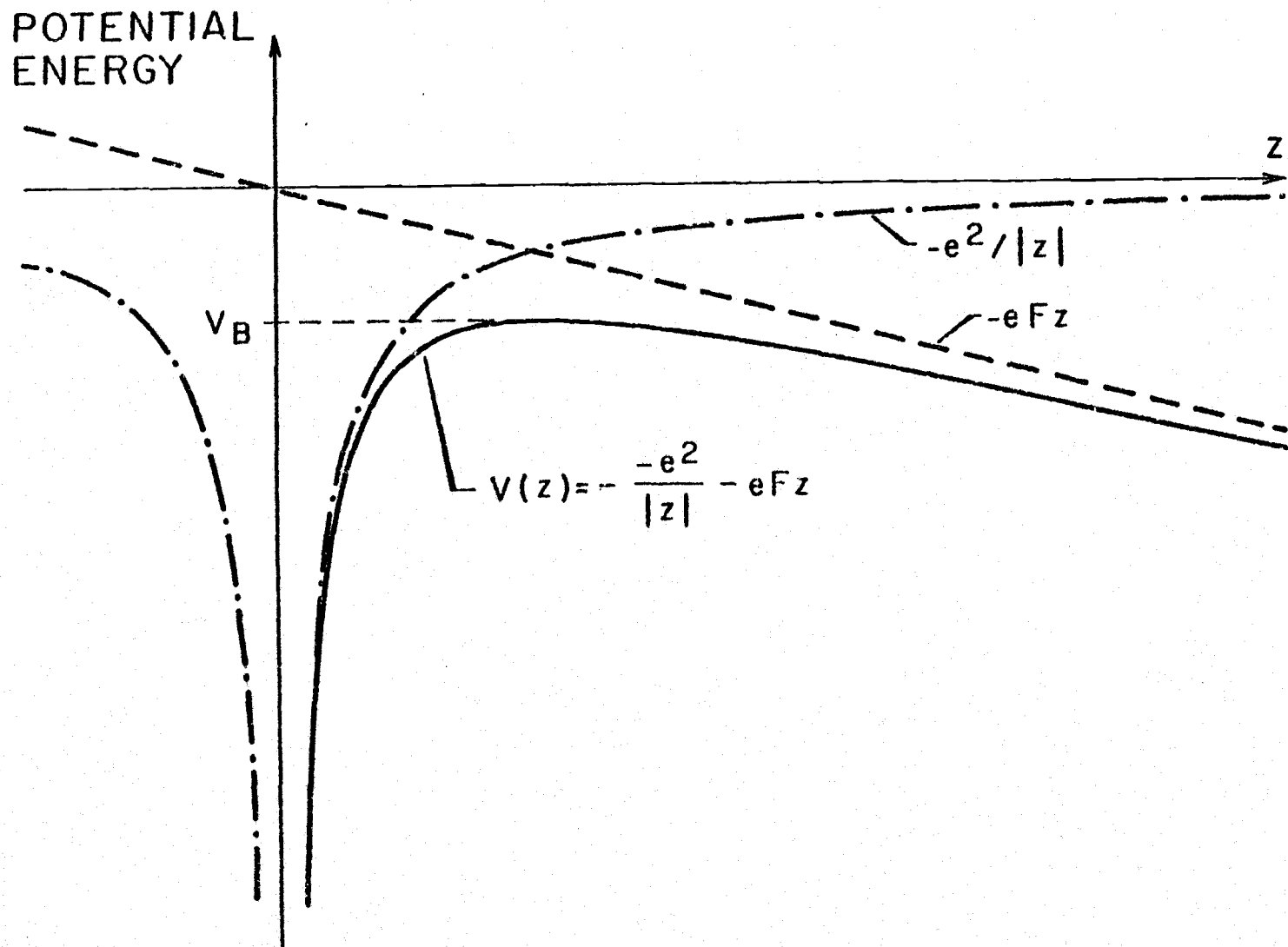


Figure 1. Contributions to the potential energy $V(z)$ at $x = y = 0$ for a hydrogen atom in an external field. V_B denotes the relative maximum of $V(z)$.

Those states with energies above the barrier are ionized in the field F , while states with energies below the top of the barrier may tunnel through it with a probability per unit time which decreases rapidly with decreasing energy. Levels lying closest to the top of the barrier have the highest tunnelling probabilities. From Equation 2.6, a critical field at which the state with quantum number n becomes ionized may be written as

$$F_c = \frac{F_0}{n_c^4}, \quad (2.7)$$

where F_0 is a constant which will be discussed presently.

A more accurate picture of field ionization would require calculation of quantum mechanical ionization probabilities for an atom in an electric field. This in turn requires a knowledge of the exact Stark energy levels and the time development of the Schroedinger equation. The Stark problem is separable in parabolic coordinates (ξ, η, ϕ) , as shown for instance by Landau and Lifshitz (L2). The equivalent η -potential has a barrier, and the solution of the Schroedinger equation leads to the parabolic quantum numbers n , n_1 , n_2 , and m , which satisfy the relation $n = n_1 + n_2 + |m| + 1$. Perturbation theory is used in Reference L2 to derive the energy shifts up to second order in the field strength. However, the method breaks down at very high fields. Rice and Good (R2), using a

WKB-type approach, calculated the correct Stark energy levels of hydrogen by requiring the wave functions to be a minimum at the outer classical turning point for fixed values of the electric field. They constructed a wave packet with states having the same values of the quantum numbers n_2 and m , but having a range of energies ΔE about E . In this manner it was shown that the probability of the electron remaining near the nucleus decreased exponentially with time, with a decay rate

$$\tau^{-1} = \frac{\Delta E}{\hbar} . \quad (2.8)$$

Similar calculations had been done earlier by Lanczos (L1), who restricted his calculations to a single dimension.

Bailey, Hiskes and Riviere (B1) have used the formulae derived in References L1 and R2 to compute field ionization probabilities for all Stark substates of hydrogen for $n = 2$ to $n = 7$, and for the extreme components ($n_1 = n - 1, n_2 = 0$ and $n_1 = 0, n_2 = n - 1$, with $m = 0$), for $2 \leq n \leq 25$. A plot of these ionization probabilities as a function of the electric field strength is shown in Figure 2, which depicts a very sharp onset of ionization and extremely large ionization probabilities above threshold for pure Stark substates. This threshold behavior is the basis for the use of field ionization for state selection in HR atoms.

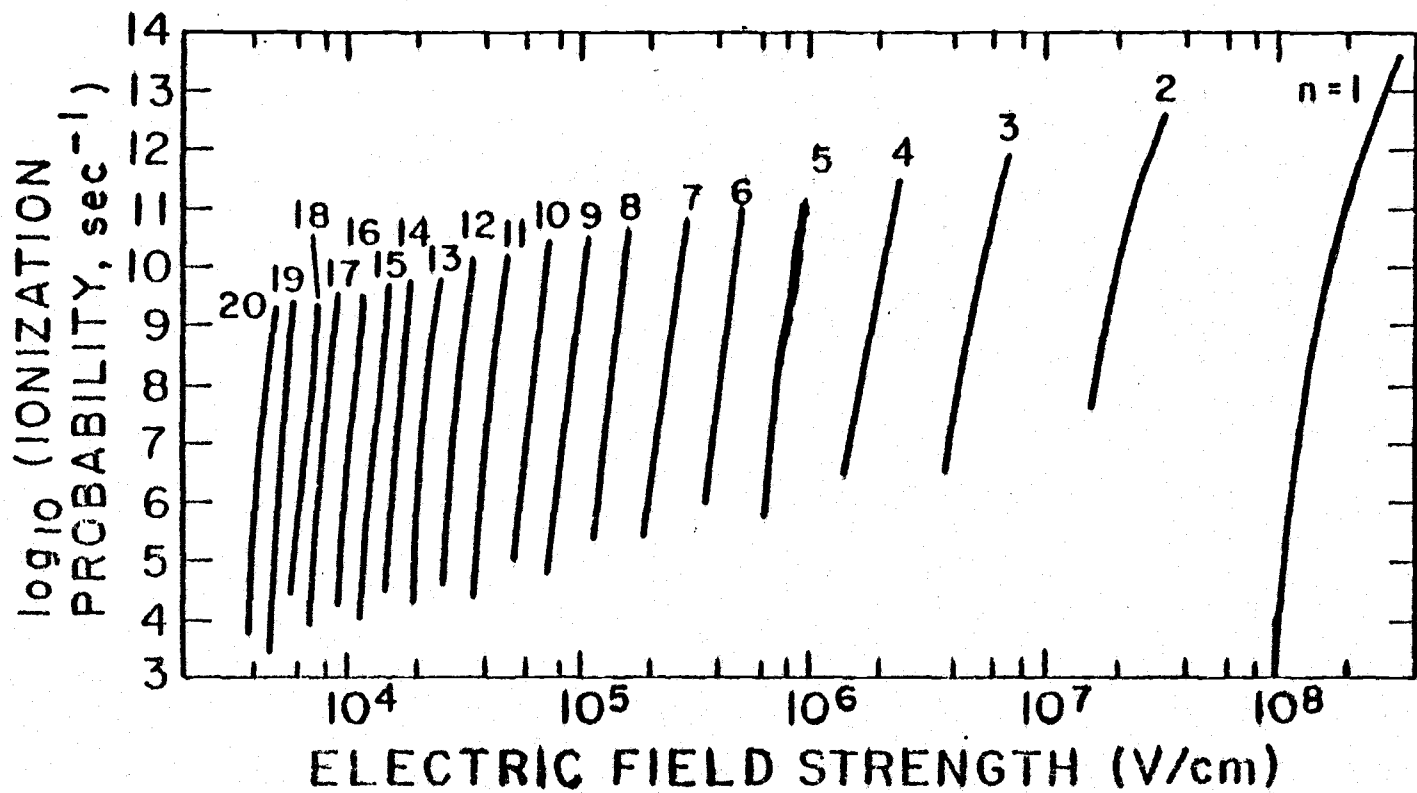


Figure 2. Ionization thresholds for the central Stark states of a hydrogen atom in an external electric field (from Bailey, Hiskes and Riviere, Ref. B1).

Riviere and Sweetman (R1) observed the ionization of a fast beam of hydrogen atoms in states with principal quantum numbers $n = 9$ to $n = 22$ in electric fields up to 1.2×10^5 V/cm. The HR hydrogen atoms were produced by passage of fast protons (kinetic energies up to 100 eV) through a neutral gas cell. The resulting charge exchange process yields hydrogen atoms in HR states. They obtained the differential rate of ionization by modulating the high voltage supply to their electrodes with an 800 Hz signal. Maxima in the differential rate of ionization curves were interpreted as being due to the ionization of states with successive principal quantum numbers. Individual substates of a given n were not resolved. The positions of the maxima compared well with the thresholds for the central components calculated by the Rice and Good method.

Il'in et al. (I1, I2, I3) have also obtained field ionization spectra for helium as well as for hydrogen. They used charge exchange between H^+ or He^+ and neutral atoms to produce HR atoms, which were studied by a field modulation technique similar to that of Reference R1. Because the angular momentum substrates of helium are not degenerate, the Stark effect in helium is quadratic at low fields, becoming linear in strong fields. Il'in explained that this effect leads to a narrower field ionization spectrum for helium than that for hydrogen. He has also noted that the experimentally measured critical ionizing fields for a state with principal quantum number n

could be written as

$$F_c = \frac{F_o}{n^\beta}, \quad (2.7)$$

where F_o depends somewhat on the field geometry, and where β is experimentally very nearly equal to 4. This is in agreement with the simplified derivation at the beginning of this section (Equation 2.7). This rule has been verified in several other field ionization studies (B3, R1, R3, S2). Bayfield and Koch (B2) have listed the values of the constant F_o and the exponent β which have been observed. In the experiment to be described in Chapter 5, the value $F_o = 6.4 \times 10^5$ kV/cm, which is appropriate for a beam containing all possible Stark substates, is adopted.

The experimental technique for state selection involves ionization of selected states (those with $n \geq n_c$) in a beam of HR atoms. The ions are removed from the beam to allow study of the remaining neutral system. If very high ionizing fields are used, all the HR states in a beam may be ionized, provided they are in high enough n -states. In this case, counting the resulting ions would yield a HR atom count if the detector efficiency is known. In the present experiment both detection and state selection by electric field ionization are employed.

2.3 Radiative Lifetimes

Radiative decay rates for excited atoms are proportional to the cube of the transition energy and the square of the transition matrix element. An expression for hydrogenic decay rates will be given shortly. The wave functions for a distant HR electron are expected to have little overlap with those of lower electronic states. Consequently the transition matrix elements for initial HR states are smaller than those for lower lying initial states. Hence HR states have longer lifetimes. If transitions are possible to several lower levels, then those to the lowest lying state, having the maximum transition energy, tend to dominate. Also, for a given n -state, low- ℓ substates decay more rapidly than substates with higher values of ℓ , because electrons in higher ℓ -states penetrate the core to a smaller extent. This fact is used in the present study to identify the presence of high angular momentum states in a beam of HR lithium atoms.

For hydrogen the theory of radiative decay in the absence of fields has been discussed by Bethe and Salpeter (B4). Hiskes, Tarter and Moody (H2) have performed extensive calculations of the lifetimes of hydrogen, using zero-field as well as Stark wave functions. Figure 3 shows the variation of hydrogenic lifetimes with n and ℓ . The lifetimes of the states of HR atoms with core structure, having a maximum value of $\ell = n - 1$, may be obtained from this figure.

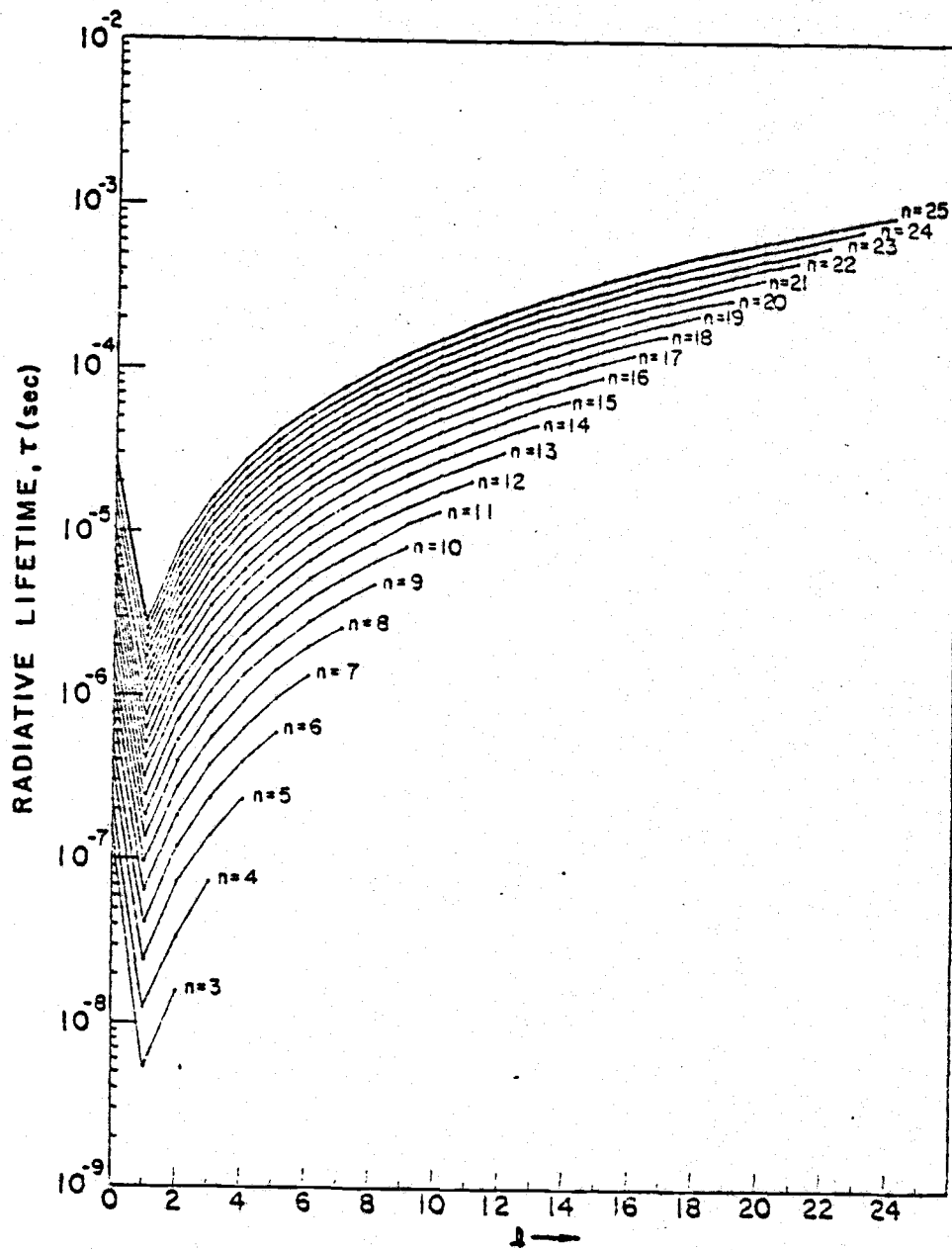


Figure 3. Radiative lifetimes for the hydrogen atom in the absence of external fields (from Hiskes, Tarter and Moody, Ref. H2).

These states, which correspond to the circular orbit states of the Bohr theory, penetrate the core to the smallest extent and are therefore most nearly hydrogenic. Because of core penetration, HR states other than those with the maximum l are expected to have non-hydrogenic lifetimes. However, Gallagher, Edelstein and Hill (G3, G4) measured the lifetimes of sodium atoms in various high Rydberg s and d states with $5 \leq n \leq 13$ and p states with $4 \leq n \leq 7$, and found them to be consistent with an $n^*{}^3$ dependence. This is seen to be similar to the n^3 dependence of the lifetimes of hydrogenic states with fixed values of n and (low) l (B4). The experimental technique of Gallagher et al. (as on page 10) involved a two-photon excitation of the (3s to 3p, then 3p to ns, nd) sodium Rydberg states, followed by observation of the ns to 3p or nd to 3p fluorescence. This leads directly to the ns and nd lifetimes. To obtain the np lifetimes, they monitored the nd-np-ns-3p cascade. Since the np state is the one which has the longest lifetime in this series, its decay determines the overall rate after long times.

Lundberg and Svanberg (L3), using a delayed coincidence technique, measured the lifetimes of Rb states 8s, 9s, 8d, and 9d, as well as Cs 10s to 12s states. The observed lifetimes were in good agreement with those calculated by the Bates and Damgaard (B5) method, which uses a Coulomb approximation to the potential of the atom. Stebbings et al. (S4) obtained values of high Rydberg Xe

lifetimes (24f to 28f) and found that they were nearly hydrogenic. These authors noted that the lifetimes were very sensitive to residual electric fields. For example the 25f lifetime was observed to vary from 8 μ sec to 24 μ sec when the field was increased from 0 to 25 V/cm. This effect was attributed to Stark-induced mixing of l -substates. There are no data available for the lifetimes of lithium atoms with $n \geq 10$, since the lifetimes of these states have not been measured (M4). However, the decay rates for lithium atoms in low n - and l -states can be extracted from a table of transition rates compiled by Wiese, Smith and Glennon (W1). Figure 4 shows these decay rates, together with their extrapolation to higher n -values. Based on the experimental values of the lifetimes for sodium, rubidium, and cesium (alkali sequence), extrapolated decay rates for lithium are expected to be quite accurate. Also shown in Figure 4 are the decay rates for states of maximum l ($= n-1$). The plotted circular-orbit decay rates are obtained from the expression

$$\Gamma_n = \frac{\Gamma_0}{5n}, \quad (2.9)$$

which may be derived from the formula for hydrogenic decay rates, given in Reference B4, in the limit of large n .

The radiative transition rate from an initial (n, l) state to a final $(n', l-1)$ state of the hydrogen atom is

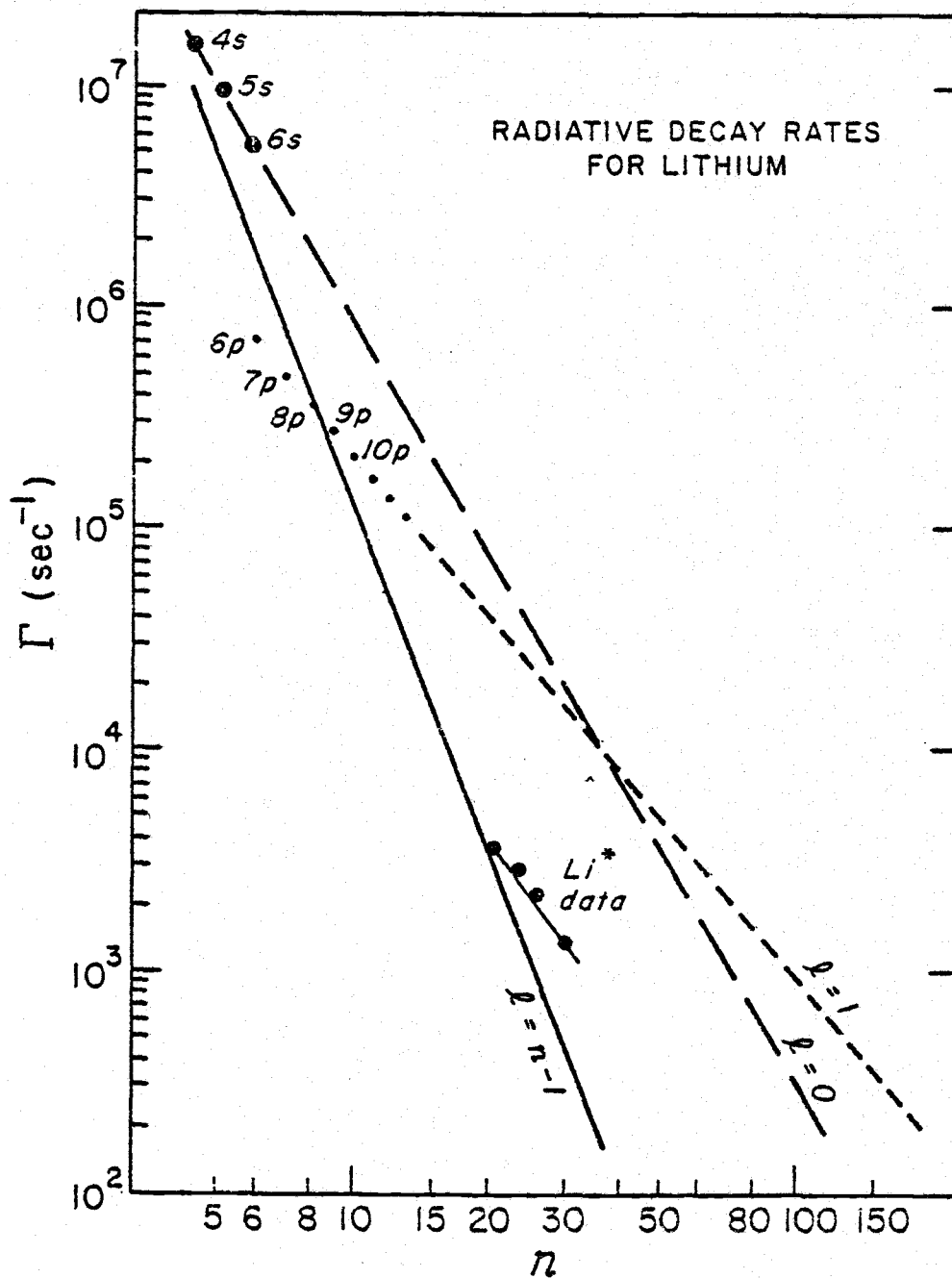


Figure 4. Radiative decay rates for lithium (dots, measured; lines, extrapolated). The Li* data points will be discussed in Section 6. 1.

$$\Gamma_{n'l-1, nl} = \frac{4}{3} \frac{e^2 a_o^2 W_{n'n}^3}{\hbar c^3} |\langle n'l-1 | \vec{r} | nl \rangle|^2, \quad (2.10)$$

where c is the velocity of light, \vec{r} is the position operator of the electron, a_o is the Bohr radius, and e is the charge of the electron. The transition energy $W_{n'n}$ is given by

$$W_{n'n} = \hbar c \text{Ryd} \left(\frac{1}{n'^2} - \frac{1}{n^2} \right), \quad (2.11)$$

where $\text{Ryd} = 109677.58 \text{ cm}^{-1}$ is the Rydberg constant for hydrogen.

Substitution of hydrogenic wave functions, $rR_{nl}(r)Y_{lm}(\theta, \phi)$, into Equation 2.10 easily yields for the square of the matrix element

$$\begin{aligned} |\langle n'l-1 | \vec{r} | nl \rangle|^2 &= \sum_{m'} |\langle n'l-1, m' | \vec{r} | nl m \rangle|^2 \\ &= \frac{l}{2l+1} (R_{nl}^{n'l-1})^2. \end{aligned} \quad (2.12)$$

Here

$$R_{nl}^{n'l-1} = \int_0^\infty R_{nl} R_{n'l-1} r^3 dr, \quad (2.13)$$

and $rR_{nl}(r)$ and $Y_{lm}(\theta, \phi)$ are associated Laguerre functions and spherical harmonics, respectively, and m is the magnetic quantum number. The integral in Equation 2.13 is given in Reference B4. If

the values $n' = n - 1$ and $l = n - 1$, which are appropriate for radiative decay from circular orbit states, are substituted into the expression for $R_{nl}^{n'l-1}$, the result is

$$R_{n,n-1}^{n-1,n-2} = \frac{1}{4(2n-3)!} \sqrt{(2n-1)!(2n-3)!} \frac{[4n(n-1)]^n}{(2n-1)^{2n-1}} \times \left\{ F[0,0,2(n-1); 4n(n-1)] - \frac{1}{(2n-1)^2} F[-2,0,2(n-1); 4n(n-1)] \right\}. \quad (2.14)$$

Here

$$F(\alpha, \beta, \gamma; x) = \sum_{\nu=0}^{\infty} \frac{\alpha(\alpha+1)\dots(\alpha+\nu-1)\beta(\beta+1)\dots(\beta+\nu-1)}{\gamma(\gamma+1)\dots(\gamma+\nu-1)\nu!} x^\nu \quad (2.15)$$

is the hypergeometric function. The $\nu = 0$ terms of the hypergeometric series for Equation 2.14 are the only non-vanishing ones.

The square of the radial integral is therefore given by

$$(R_{n,n-1}^{n-1,n-2})^2 = \frac{(2n-1)!}{16(2n-3)!} \frac{[4n(n-1)]^{2n+2}}{(2n-1)^{4n+2}}. \quad (2.16)$$

Substitution of Equations 2.11, 2.12 and 2.16 into 2.10 leads to the circular orbit decay rate

$$\Gamma_{n-1,n} = C \left(\frac{1}{(n-1)^2} - \frac{1}{n^2} \right)^3 \frac{n-1}{(2n-1)} \frac{(2n-1)!}{16(2n-3)!} \frac{[4n(n-1)]^{2n+2}}{(2n-1)^{4n+2}}, \quad (2.17)$$

where

$$C = \frac{4}{3} \frac{e^2 a_0^2 (\text{Ryd})^3}{\hbar^4 c^3} = 2.6759 \times 10^9 \text{ sec}^{-1}$$

is a constant, and the ℓ -subscripts for Γ have been dropped for clarity. Equation 2.17 easily simplifies to

$$\Gamma_{n-1, n} = C 2^{4n+1} (n-1)^2 \frac{[n(n-1)]^{2n-4}}{(2n-1)^{4n-1}}. \quad (2.18)$$

Finally the large- n limit of 2.18 gives the desired decay rate as

$$\Gamma_{n, n-1} = \frac{\Gamma_0}{n^5},$$

which is the same as Equation 2.9 with $\Gamma_0 = 4C = 1.07 \times 10^{10} \text{ sec}^{-1}$.

From the discussion in this section it can be seen that hydrogenic decay rates vary approximately as $1/n^3$ for low- ℓ values and as $1/n^5$ for high- ℓ states. If all the ℓ -substates of a given n are occupied, then the state decays with a statistically averaged decay rate given by (B4)

$$\Gamma_{\text{ave}} = \sum_{\ell=0}^{n-1} \left(\frac{2\ell+1}{n^2} \Gamma_{n\ell} \right) \propto n^{-4.5}, \quad (2.19)$$

where

$$\Gamma_{nl} = \sum_{n'l'} \Gamma_{n'l',nl}$$

is the total decay rate out of an initial (n, l) state to all possible final states.

2.4 Excitation

Electron impact excitation, charge transfer collisions, and photo-excitation are the processes most frequently employed in the production of HR atoms and molecules. Some examples of experiments in which these techniques have been used will now be discussed.

In electron impact excitation a beam of atoms or molecules is bombarded by a transverse beam of electrons in an excitation region. Ions, HR atoms or molecules, as well as dissociation fragments (in the case of molecules), can be formed. The charged particles are removed from the beam by weak electric or magnetic fields. Čermák and Herman (C1) produced highly excited states of the noble gases, with an undetermined n -distribution, by electron impact. Kupriyanov (K3, K5) also formed HR states of H, H₂, He, Ne, Ar, Kr, and Xe by electron bombardment of hydrogen and the noble gases, and of C, O and N by bombardment of CO and N₂. He measured the excitation function for the rare gases, and found the shapes to agree with theoretical predictions of Massey and Burhop (M3).

Electron impact excitation of molecules can lead not only to excitation but also to dissociation, with one or more of the fragments in HR states. Because the released energy (the difference between excitation and dissociation energies) goes into increasing the kinetic energy of the fragments, this method of production leads to non-thermal HR beams. Dissociative excitation of N_2 by electron impact was used by Kocher and Fairchild (K8) and by Smyth, Schiavone and Freund (S5) to produce HR nitrogen atoms.

A comprehensive theory of electron impact excitation is not available. Vainshtein (V1) has calculated, in the Born approximation, the cross sections σ^{ex} for several transitions of hydrogen and sodium for excitation by electron impact. His tabulated results include those for the hydrogenic transitions $1s$ to ns , np and nd , and $(n-1)s$ to ns , np and nd for $2 \leq n \leq 9$, together with those for sodium transitions $3s$ to np for $3 \leq n \leq 7$. The σ^{ex} -values are typically of atomic size ($\approx 10^{-16} \text{ cm}^2$). Vainshtein also gives analytical empirical formula for σ^{ex} as functions of the incident electron energy.

Fano (F4) has suggested that excitation by electrons should lead primarily to low- l states, unless the exciting electron energies are within a fraction of 1 eV above or below the ionization threshold. In the case of near-threshold excitation, the incident and excited electrons become closely correlated, as they move away from the ion

core with very low velocities. This low velocity of the electrons enables them to exchange sufficient angular momentum to attain high- l excitation.

The distribution of n in electron bombardment was measured by Shibata, Fukuyama and Kuchitsu (S6) for helium. They estimated that n was in the range $16 \leq n \leq 40$ for an incident electron kinetic energy of 100 eV. Schiavone, Donohue, Herrick and Freund (S3) observed n -values in the range 20 to 80 for helium excited by 100-eV electrons. The HR production cross section was found to be $3 \times 10^{-20} \text{ cm}^2$, and the excitation cross section for a given n range has a $1/n^3$ dependence. In the experiment to be described in Chapter 5, electron impact is used to produce a beam of HR lithium atoms.

The technique of charge exchange involves passage of fast ions through a region containing neutral atoms. In the resulting collisions some ions capture electrons into high- n states. Ions may be removed from the beam by weak electric and magnetic fields. A brief review of the theory of charge exchange collisions is given by Fedorenko, Akudinov and Il'in (F5). For hydrogen, the cross section for charge transfer is a function of the effective charge of the colliding particles, the n and l quantum numbers of the state being formed, and the relative kinetic energies of the particles. At large relative energies, charge exchange into s states is preferred and the

cross section for the process has a $1/n^3$ dependence.

Riviere and Sweetman (R1) used charge exchange collisions of 100-eV protons in hydrogen or rare gas atoms to produce H^* , with n ranging from 9 to 23. Il'in, Oparin, Serenkov, Solov'ev and Fedorenko (I2) studied the formation of He^* ($9 \leq n \leq 17$) during charge exchange of 30- to 180-keV He^+ with Ne, Na and Hg. They verified that the production cross section varied as n^{-3} . Il'in et al. (I4) also studied the formation of H^* ($9 \leq n \leq 16$) by charge exchange in alkali vapors (Li, Na, K and Cs) and gases (Ne, He, Ar and H_2). In both cases their results are in agreement with an n^{-3} dependence of the production cross section.

Bayfield, Khayrallah and Koch (B3) studied the production of fast HR hydrogen atoms ($13 \leq n \leq 28$) from charge exchange collisions between 7 to 60 keV protons and atomic hydrogen. They found that the fraction of electron transfer collisions producing high Rydberg atoms is not very different from those found in rare gas targets (e. g. , argon). The observed cross section had a maximum at 30 keV. The total cross section for electron transfer was found to have the values $0.25 \times 10^{-20} \text{ cm}^2$, $19.6 \times 10^{-20} \text{ cm}^2$ and $6.6 \times 10^{-20} \text{ cm}^2$ at the incident electron energies 7 keV, 30 keV and 60 keV, respectively.

While electron impact and charge transfer collisions produce HR atoms in a range of principal quantum number n ,

photo-excitation can produce pure high Rydberg states. In general a two-step process is required, since available laser photons are ordinarily not sufficiently energetic to excite the HR states of most atoms directly. Stebbings, Latimer, West, Dunning and Cook (S4) excited Xe atoms first to a metastable 3P_0 state by electron impact, from which state the atoms were raised to np ($11 \leq n \leq 16$) and nf states ($8 \leq n \leq 40$) by means of a tunable dye laser. The apparent violation of the selection rule $\Delta l = \pm 1$ was explained as being due to the fact that either the initial or final state, or both, should really be described by a superposition of states.

Gallagher, Edelstein and Hill (G1) excited ns and nd states of sodium with n in the range 5 to 17, using two tunable-dye-laser photons. The first laser excited the $3p$ state, from which the ns and nd states were pumped. A similar procedure was used by Ducas, Littman, Freeman, and Kleppner (D1) to produce s and d states of sodium with n in the range 27 to 37.

In a variation of this technique proposed by Littman, Zimmerman, Ducas, Freeman, and Kleppner (L4), it is possible to populate levels which are normally inaccessible from a ground state by a photon transition because of the selection rule $\Delta l = \pm 1$. There is no selection rule with respect to the quantum numbers n_1 and n_2 ; in the presence of an electric field all possible Stark states can be excited. For atoms other than hydrogen, there is no l -degeneracy;

and each Stark state connects adiabatically to a single angular momentum state. Thus if one excites the atom in an electric field in which the first-order Stark structure is resolved and then one reduces the field to zero, states with any desired l can be populated.

2.5 Collisions

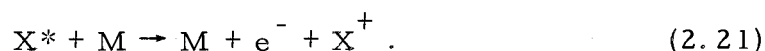
Because of their very large sizes, HR systems are expected to have enormous cross sections (on an atomic scale) for various processes. The geometric cross section for a state with principal quantum number n is

$$\sigma^{\text{geom}} = \pi n^4 a_0^2, \quad (2.20)$$

which, at $n = 30$, is more than 10^5 times a typical atomic cross section. Previous measurements of HR cross sections have yielded values which are larger as well as values which are smaller than geometric, depending on the process that was being investigated. These studies have identified two kinds of HR collision processes, ionization and angular momentum mixing. In collisions between HR systems and polar or electronegative molecules, rotational excitation energy of the molecule can be transferred to the HR system, which can therefore be ionized. When there is insufficient transferable energy to ionize the HR atom or molecule, such as in collisions

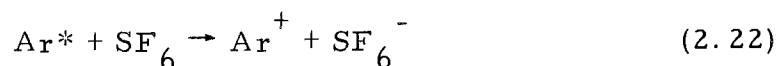
with electrons and atoms, the angular momentum of the Rydberg electron can change. These processes can be understood qualitatively in the following manner. The distant HR electron can participate in localized collisions with other particles, during which the core ion is not affected. If enough energy is transferred to the HR electron to overcome its binding, then ionization occurs. If the electron is simply deflected in its path, it might acquire a new orbit with a different value of angular momentum but with no change in energy or principal quantum number. Studies of collisional ionization and angular momentum mixing will now be reviewed.

Kupriyanov (K3) produced various HR atoms and molecules by electron impact excitation and detected them by collisional ionization followed by mass and charge analysis. The HR species H^* , H_2^* , He^* , Ne^* , Ar^* , Kr^* and Xe^* were studied. Cross sections for the above ionization processes were not given, and the n -distribution of the HR states excited was unknown. Hotop and Niehaus (H3), using similar experimental techniques, obtained cross sections for reactions of the type



In their measurement, $X = He, Ne, \text{ or } Ar$ and $M = H_2O, NH_3, SO_2, \text{ or } C_2H_5OH$. The observed cross sections were of the order of 10^{-12} cm^2 . They also found the cross section for the formation of

SF_6^- in the reaction



to be $(1.7 \pm 0.1) \times 10^{-12} \text{ cm}^2$. The velocity dependence of the ionization cross section was not given. The n-dependence was also not given, since the n-distribution of the HR states was not determined. Kupriyanov (K4, K5) estimated the cross section for scattering of Ar^* by H_2 to be at least $0.4 \times 10^{-13} \text{ cm}^2$, and for C^* and O^* by CO to be $2 \times 10^{-13} \text{ cm}^2$ and $1.5 \times 10^{-13} \text{ cm}^2$ respectively. Since he suggests that these cross sections are in agreement with those obtained in Reference H3, it is not clear whether Kupriyanov's cross sections are for HR deflections or for processes of the type in Equation 2.21.

To explain the results cited in the last paragraph, Matsuzawa (M2) proposed a mechanism in which the high Rydberg electron is ionized after gaining energy from the molecule in a rotationally excited state at room temperature. The calculated and experimental cross sections are in reasonable agreement. Matsuzawa employs a model in which the excited electron participates in a localized interaction with a dipolar or quadrupolar molecule; the core ion merely looks on. Fermi had earlier used a similar technique in order to explain the shifts of high series terms of the absorption spectrum of

sodium and potassium, observed by Amaldi and Segrè (A1).

West, Foltz, Dunning, Latimer and Stebbings (W2) measured absolute cross sections for ionization of Xe atoms in well-defined high Rydberg nf states during collisions with the electronegative molecule SF_6 . Their cross sections are of the order 10^{-11} cm^2 for $25 \leq n \leq 40$, and their data support the idea of SF_6 interactions with the Rydberg electron which are independent of the core ion. They have also extended these measurements to include polar molecules SO_2 , H_2S , NH_3 , and H_2O (F3). For these measurements the Xenon atoms were first excited to the 3P_0 metastable state by electron impact and then photoexcited to selected HR states. West et al. used Matsuzawa's theory to interpret their results.

Koch and Bayfield (K6) found charge exchange cross sections in the merged beam collision of H^* and N^* to be in the range $(1 \text{ to } 8) \times 10^{-9} \text{ cm}^2$. The HR atoms were in principal quantum states $44 < n < 50$ and had relative kinetic energies $0.4 \leq W \leq 61 \text{ eV}$. The observed cross sections were an order of magnitude larger than geometric for the maximum $n (= 50)$ in their beam.

Gallagher, Edelstein, and Hill (G5, G6) have investigated collisions between sodium atoms in nd states ($5 \leq n \leq 15$) and helium, neon and argon atoms. Their method consisted of a two-photon excitation of sodium nd states in a collision cell also containing the rare gas. As a result of the collisions, the d levels were mixed with

all substates for which $\ell > 2$, of the same n . The s and p states were energetically far removed from the other angular momentum states and were therefore not appreciably mixed. The mixture of $\ell \geq 2$ levels was observed to decay with an effective lifetime

$$\tau_{\text{eff}} = \frac{1}{n^2 - 4} \sum_{\ell=2}^{n-1} \left(\frac{2\ell+1}{\tau_{n\ell}} \right)^{-1} \quad (2.23)$$

which was much longer than the nd lifetimes. They extracted from their results a statistical average lifetime

$$\tau_{\text{av}} = \frac{1}{n^2} \sum_{\ell=0}^{n-1} \left(\frac{2\ell+1}{\tau_{n\ell}} \right)^{-1} \quad (2.24)$$

and found it to vary as $n^{4.55(6)}$, in excellent agreement with the Bethe and Salpeter prediction (Equation 2.19) for the n -dependence of τ_{av} for the hydrogen atom. The ℓ -changing cross sections were extracted by fitting the data to a two-state decay model; the two states consisted of the initial d state and the reservoir of $\ell > 2$ states. These cross sections increase sharply with increasing n for $5 \leq n \leq 10$, and then decrease with n for $10 < n \leq 15$, and were of order 10^{-13} cm^2 . Their results are well accounted for by Olson's close coupling calculation (Ol), which uses low-energy electron scattering lengths of the noble gases to obtain ℓ -mixing cross sections. This theory (and its agreement with experiment) confirms the idea that ℓ -mixing is due to the interaction between the

HR electron and the rare gas atom. At lower n -values the probability of finding the electron anywhere in its orbit is high, so that the passage of the target atom within the orbit automatically leads to ℓ -mixing. Hence the ℓ -mixing cross section for low n reflects the size of the atom, having an n^4 dependence, as in Equation 2.20. For higher n -values the electron cloud becomes more diffuse, and therefore the electron is less likely to collide with the target atom, leading to a decrease in cross section with increasing n . In another theoretical effort to explain the results of Gallagher et al., Gersten (G7) employed the impact parameter approach, a Breit-Fermi pseudo-potential to represent the interaction between a HR electron and a rare gas atom, and numerical integration to derive ℓ -changing cross sections which are in agreement with the experiment.

In HR electron collisions with a free electron, the angular momentum quantum number ℓ can change. Thus in electron impact excitation, if the atom is excited when it first enters the excitation region, further collisions with electrons may lead to ℓ -mixing. This process has apparently been observed by Freund et al. (F6).

The studies reviewed above deal with electron processes in which a HR atom may be ionized or its angular momentum changed. It is also possible for the HR atom to be merely deflected during collisions with other species. A search through recent literature has failed to reveal any investigations of collisional deflections of HR

atoms. The present experiment is the first study of this aspect of HR interactions. In contrast to the processes reviewed above, deflections appear to be a result of elastic collisions between the core-ion and an atom or neutral molecule. Evidence supporting this hypothesis will be presented in Chapter 6, and a deflection theory which anticipates some of this evidence will be presented in Chapter 3.

2.6 Detection

For detecting HR states, field ionization, surface ionization, collisional ionization, and optical detection techniques have been used. In the first three modes listed above, ions formed by the interaction of HR atoms with fields, or metal surfaces, or polar and electronegative molecules, are mass analyzed, collected in a Faraday cup, or counted by a single-particle detection system. For example, Kupriyanov (K3) ionized HR atoms by passing the beam of excited atoms through a chamber containing a target gas. By a subsequent mass analysis of the resulting ions, he was able to identify the formation of HR atoms of the rare gases. Hotop and Niehaus (H3) studied collisional ionization by a similar technique. Surskii and Kupriyanov (S6) and Kupriyanov (K7) have demonstrated the ionization of HR atoms near metal surfaces. Chaplik (C2) has pointed out that the mechanism for surface ionization of slow-moving, highly excited atoms is that of charge exchange between the metal and the atom. If the state of the

atom corresponds to the allowed band of the metal, then transition of the electron into the metal can occur. The atomic electron tunnels through the barrier created between the potential wells of the atom and the metal during the collision. Chaplik calculated the ionization probability for HR hydrogen atoms in s states, and Janev (J1) generalized his results to include ionization of arbitrary hydrogenic states.

Of the ionization techniques for HR detection, field ionization is probably the most widely used. Riviere and Sweetman (R1) and Il'in et al. (I4) used field ionization followed by a scintillation detector in HR studies of hydrogen and helium. Their experiments, as well as other aspects of field ionization, have been discussed earlier in Section 2.2.

When pure HR states are involved, monitoring the fluorescence as the atom decays to a lower lying level is an excellent means of detecting HR states. A major advantage of this optical method is its high specificity. Through the use of interference filters, the decay of a single HR state can be studied. Since the interference filters can be constructed for each narrow range of the optical spectrum, this technique is seen to be of wide applicability. Gallagher et al. (G4) measured nd and nf lifetimes of sodium directly, by observing the nd to $3p$ decay as a function of time after excitation. Their experiment was reviewed in Section 2.3.

3. THEORY OF THE EXPERIMENT

In this chapter a general expression for the HR transit-time distribution with applied electric fields and introduced target gases is derived. The ionization probability in a HR atom collision with a neutral atom is also discussed, and the cross section for HR deflection is calculated.

3.1 Time-of-Flight Spectra with Applied Electric Fields

In the absence of radiative decay and collision-induced state changes, the time-of-flight (TOF) spectrum of a beam of HR atoms is determined by the initial velocity distribution in the beam. From simple kinetic theory considerations, it can be shown that the velocity distribution in an atomic beam is (R4)

$$g(v)dv \approx v^3 \exp(-\frac{1}{2}mv^2/kT)dv, \quad (3.1)$$

where $g(v)dv$ is the probability that an atom has a velocity in the range dv at v ; m is the atomic mass, $k = 1.3805 \times 10^{-16}$ erg deg⁻¹ is the Boltzmann constant, and T is the Kelvin temperature inside the source. For a fixed flight path length L , Equation 3.1 may easily be converted to a transit-time distribution. If t is the transit time ($t = L/v$), and $f(t)dt$ is the probability that the transit time is in dt at t , then

$$f(t)|dt| = g(v)|dv|, \quad (3.2)$$

which gives

$$f(t) = g(v) \left| \frac{dv}{dt} \right|. \quad (3.3)$$

Since $\left| \frac{dv}{dt} \right| = L/t^2$, Equations 3.1 and 3.3 yield for $f(t)$ the expression

$$f(t) = \frac{\kappa}{t^5} \exp(-t_0^2/t^2), \quad (3.4)$$

where $t_0 = \sqrt{\frac{mL^2}{2kT}}$ and κ is a normalization constant. For a flight path length of 35 cm and a source temperature of about 770°K, t_0 for a lithium beam is 2.6×10^{-4} sec. The parameters used here are representative of the conditions during the experiment to be described in Chapter 5.

An unknown population $P(n, \ell)$ of HR states is produced in electron impact excitation. From previous experiments (Section 2.4), it is expected that

$$P(n, \ell) \propto n^{-3}. \quad (3.5)$$

This is an approximation which holds best for hydrogenic p states. If the excitation energy is far from the threshold value, predominantly low- ℓ states are expected (Fano, F4). These HR states with low ℓ -values tend to decay to low-lying non-Rydberg states. With the assumption therefore that each radiative decay removes an excited

atom from the beam, the following expression for the HR TOF spectrum may be written

$$N(t) = f(t) \sum_{n=n_{\min}}^{\infty} \sum_{\ell=0}^{n-1} P(n, \ell) e^{-\Gamma_{n\ell} t} \quad (3.6)$$

Here $N(t)$ is the relative probability that an excited atom has a transit time t , and $\Gamma_{n\ell}$ is the radiative decay rate of the (n, ℓ) state. The lower limit of the sum over n is determined by in-flight radiative decay. For lithium atoms at approximately 770°K having a typical velocity of 2×10^5 cm/sec, the minimum lifetime of a HR state which survives a 35-cm flight without radiative decay is of order 10^{-4} sec. From the extrapolated (n, ℓ) lifetimes of lithium in Figure 4, it is estimated that for $n \lesssim 20$ there is no significant contribution to the HR lithium beam. The numerical values used in this estimate of n_{\min} are appropriate for the present experiment.

In the presence of an electric field, the upper limit of the n summation (Equation 3.6) is determined by field ionization (Section 2.2). The effect of an electric field on a HR beam containing a distribution of n -levels, is essentially to remove all the HR states with $n > n_c$, where n_c is found from Equation 2.7:

$$n_c = \left(\frac{F_0}{F} \right)^{1/4} \quad (3.7)$$

Hence the transit-time distribution in the presence of an applied electric field is

$$N_F(t) = f(t) \sum_{n=n_{\min}}^{n_c} \sum_{\ell=0}^{n-1} P(n, \ell) e^{-\Gamma_{n\ell} t}, \quad (3.8)$$

where in the derivation of Equation 3.8 it has been assumed that the passage of an atom through the electric field is adiabatic and therefore that $P(n, \ell)$ is not significantly modified (except by the removal of states with $n > n_c$). This assumption can be justified if it can be shown that the electric field as a function of time $F(t)$ varies slowly compared to the period of oscillation τ for a transition between various (n, ℓ) levels. The time dependence of the electric field arises from fringing at the edges of the field plates. The criterion for justification of the adiabatic approximation therefore becomes

$$\Delta t \gg \tau \approx \frac{\hbar}{\Delta E}, \quad (3.9)$$

where Δt is a characteristic time over which the electric field changes from zero to its steady state value between the plates, and ΔE is the energy separation between a pair of (n, ℓ) levels for

which adiabaticity is being tested. In the present experiment the electric field is provided by a pair of electric field plates which are at a distance of 1.0 cm apart, the atoms have a typical velocity of 2×10^5 cm/sec, and Δt is therefore approximately equal to 5×10^{-6} sec. The condition in Equation 3.9 may therefore be written as

$$\Delta E \gg \frac{\hbar}{\Delta t} = 1.3 \times 10^{-10} \text{ eV.} \quad (3.10)$$

The adiabatic criterion will now be tested for transitions between adjacent n -states as well as those between adjacent l -states with the same n . The energy separation between states with principal quantum numbers n and $n + 1$ is

$$\Delta E \approx \frac{27 \text{ eV}}{n^3}. \quad (3.11)$$

Substitution of Equation 3.11 into 3.10, leads to

$$n^3 \ll \frac{27}{1.3 \times 10^{-10}}, \quad (3.12)$$

which indicates that the passage of the atom through the electric field is adiabatic with respect to transitions between adjacent n -states, except for those in states with n larger than 5000. At a principal quantum number n , the zero-field level separation between two

adjacent ℓ -states with quantum defects δ_ℓ and $\delta_{\ell+1}$ is

$$\Delta E = -\frac{27 \text{ eV}}{2(n-\delta_\ell)^2} + \frac{27 \text{ eV}}{2(n-\delta_{\ell+1})^2}, \quad (3.13)$$

leading to

$$\Delta E \approx \frac{27 \text{ eV}}{3n} \delta, \quad (3.14)$$

where $\delta = \delta_\ell - \delta_{\ell+1}$. The adiabatic condition for adjacent ℓ -states is therefore

$$\delta \gg 4.8 \times 10^{-12} n^3. \quad (3.15)$$

For large n and ℓ , quantum defects are determined mainly by core polarization. Edlén (E1) has given an expression for the quantum defects of lithium states with $l \geq 3$, which is

$$\delta_\ell = 9(z-0.4)^{-4} h(n, \ell), \quad (3.16)$$

where

$$h(n, \ell) = \frac{3 - \ell(\ell+1)n^{-2}}{4(\ell - \frac{1}{2})\ell(\ell + \frac{1}{2})(\ell+1)(\ell + \frac{3}{2})} \quad (3.17)$$

and $z = 3$ is the atomic number for lithium. For the worst case of large values of both n and ℓ , the difference between $h(n, \ell)$ and $h(n, \ell+1)$ is of order $3/n^5$ for $\ell \approx n$, and the adiabatic condition for adjacent ℓ -states reduces to

$$\frac{1}{n^8} \gg \frac{(2.6)^4 \cdot 4.8 \times 10^{-12}}{27} \quad (3.18)$$

The above inequality indicates that the passage of the atom through the electric field can be non-adiabatic with respect to l -transitions, for states with principal quantum number n greater than 25. This failure of the adiabatic condition to apply to transitions between adjacent l -states does not, however, affect the outcome of the present experiment. Because the electric field plates are located at the end of the flight path, next to the detector, field-induced changes in l , and the accompanying changes in the radiative decay rates, do not significantly modify the HR content of the beam. Derivation of the adiabatic condition for adjacent l -states was included in this section for completeness.

An experimentally accessible quantity, independent of $f(t)$, is the ratio of two functions $N_{F'}(t)$ (Equation 3.8) at different electric fields F and F' :

$$R_{FF'}(t) = \frac{N_F(t)}{N_{F'}(t)} = \frac{\sum_{n=n_{\min}}^{n_c} \sum_{l=0}^{n-1} P(n, l) e^{-\Gamma_{nl} t}}{\sum_{n=n_{\min}}^{n'_c} \sum_{l=0}^{n-1} P(nl) e^{-\Gamma_{nl} t}} \quad (3.19)$$

It will be shown in Chapter 6 that measurements of this quantity can lead to a determination of radiative decay rates.

3.2 Ionization Probability in High Rydberg Collisions with Neutral Atoms

In this section it will be shown that ionization is of negligible probability in a high Rydberg lithium atom (Li^*) collision with a rare gas atom (helium, neon and argon) or with a neutral molecule of hydrogen or nitrogen. These gas species, together with ammonia, were used as target gases in the present experiment. (The interaction of NH_3 can lead to ionization by the Matsuzawa-type process discussed in Section 2.5; NH_3 is excluded from the analysis of this section.) For the sake of simplicity, this derivation is carried out using classical mechanics, which in the limit of large quantum numbers (such as large n for HR states), agrees with quantum mechanics. In an elastic collision between a HR electron and a neutral atom, there can be no energy exchange if the atom is treated as an infinitely heavy and stationary target. However, energy can be transferred to the HR electron as a result of the motion of the target atom during the collision. In classical theory, the orbit radius of the HR electron is changed by an insignificant amount (compared to the size of the radius) during a localized collision with an atom. This is because the size of the collision region is small compared to the

orbital radius of the electron. The electronic orbital velocity can, however, change.

Qualitatively, it can be argued that a change in the direction of the electron's velocity can result in a new electronic orbit, with a different value of the angular momentum quantum number l . A change in the magnitude of the electronic velocity v , on the other hand, can lead to an increase in its kinetic energy and possibly to ionization. The total energy E of the electron is the sum of its kinetic and potential energies:

$$E = \frac{1}{2} mv^2 - \frac{e^2}{r} . \quad (3.20)$$

Here m and e are the electron's mass and charge, and r is its radial distance from the core ion. Ionization occurs if the final velocity v_f of the electron is such that the total energy is positive, i. e., if

$$v_f > \sqrt{\frac{2e^2}{mr}} . \quad (3.21)$$

For $r = n^2 a_0$, the Bohr radius of the electron, Equation 3.21 can be written as

$$v_f > \sqrt{2} v_n \quad (3.22)$$

where $v_n = \frac{\alpha c}{n}$ is the initial orbital velocity of an electron in the

$$v_f \approx u_i + v_n . \quad (3.24)$$

Substitution of Equation 3.24 into 3.22 leads to a condition for ionization

$$u_i > (\sqrt{2} - 1)v_n . \quad (3.25)$$

For a Maxwell-Boltzmann distribution of target gas atom velocities

$$g(u_i) = 4\pi \left[\frac{M_t}{2\pi kT} \right]^{3/2} u_i^2 \exp\left(-\frac{M_t u_i^2}{2kT}\right), \quad (3.26)$$

the probability of ionization P is

$$P = \int_{(\sqrt{2}-1)v_n}^{\infty} g(u_i) du_i , \quad (3.27)$$

which is less than 10^{-14} for states with n below 80. If ionization does not occur but the principal quantum number changes by one during the collision, then

$$u_i > v_n / n . \quad (3.28)$$

This relation may be derived by a procedure similar to that by which Equation 3.25 was obtained. If the lower limit of the integral in Equation 3.27 is replaced by v_n/n , one finds a probability of 0.3 that n changes by unity, at an n -value of at least 60 and for an

argon target. Thus it has been established that in an elastic collision between a HR electron and an atom with thermal energies, the principal quantum number n can change (provided n is high enough), but the electron will remain bound.

3.3 Ion-Atom Scattering

When HR atoms in a beam are allowed to collide with target atoms, loss of excited atoms from the beam can result from ionization, radiative decay, and deflection. Ionization has been shown to be of negligible probability in Section 3.2. In the present section the deflection of HR atoms will be studied. Since alkali photo-absorption to high- n states has been observed even with large numbers of rare gas atoms present within the Rydberg orbit (A1), it is reasonable to suppose that target atoms which penetrate the outer electron cloud can interact directly with the core-ion.

Ion collisions produce no significant change in the electron wave function, as the momentum transferred to the ion is small compared with the orbital momentum of the electron. Such ion-atom encounters can, however, lead to the deflection of the HR atom out of the beam. When a slow ion and a slow atom having polarizability α_p approach each other, the atom becomes polarized in the Coulomb field of the ion. The induced dipole moment of the atom then interacts with the field of the ion to produce an attractive force between the two

particles. The interaction potential has an asymptotic form

$$V(r) = \frac{\alpha e^2}{2r^4}, \quad (3.29)$$

where r is the separation between the atomic and ionic centers. The differential and effective cross sections for this process will now be derived.

An experimentally accessible quantity is the cross section $\sigma(\theta_0)$ for scattering into angles greater than the angle θ_0 subtended by the detector at the source. The angle θ_0 is estimated from the geometry of the experimental setup to be of order 1° . Classical mechanics can be applied to the analysis of such measurements, as long as the scattering angles remain sufficiently large. At very small scattering angles, quantum theory must be used for the analysis. The critical angle θ_c below which classical theory is no longer valid is (Hasted, H5)

$$\theta_c \approx \frac{\lambda}{2r_0} = \frac{\pi h}{mv_r r_0}, \quad (3.30)$$

where m and λ are the mass and the de Broglie wavelength of the incident particle, and where v_r and r_0 are the relative velocity and distance of closest approach of the interacting particles. The values $v_r \approx 2 \times 10^5$ cm/sec and $r_0 \approx 10^{-7}$ cm, the square

root of typical cross sections, are appropriate for the present experiment, which uses a beam of Li atoms. With these values, $\theta_c \approx 0.3^\circ$, which is within a factor of 3 of θ_0 . Thus quantum scattering effects may still be important in the present experiment. However, since quantum corrections are expected to be small, they are not considered in the following analysis.

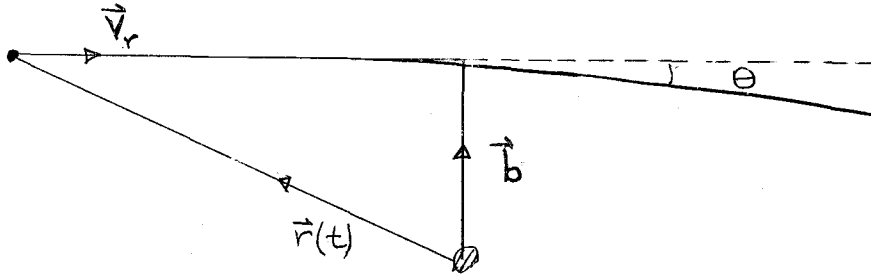
The collision between two particles interacting via a central force can always be reduced to an equivalent one-particle motion about the center of mass (c.m.). The mass of the equivalent one particle is the reduced mass

$$\mu = \frac{m_1 m_2}{m_1 + m_2}, \quad (3.31)$$

and its velocity is the relative velocity of the two particles

$$\vec{v}_r = \vec{v}_1 - \vec{v}_2, \quad (3.32)$$

where m_1 and m_2 are the masses and \vec{v}_1 and \vec{v}_2 are the velocities of the interacting particles. In the collision between a HR electron and an atom, depicted below, b will denote the impact parameter and $\vec{r}(t)$ the relative position of the equivalent particle.



In the small-angle approximation, the trajectory of the incident particle is

$$\vec{r}(t) = \vec{v}_r t + \vec{b}, \quad (3.33)$$

where the time t is chosen to be 0 at the point of closest approach. The impulse $\Delta\vec{p}$ derived from this collision is

$$\Delta\vec{p} = \int_{-\infty}^{\infty} -\vec{\nabla}V(r)dt, \quad (3.34)$$

where $r = |\vec{r}(t)|$. The component of $\Delta\vec{p}$ perpendicular to the direction of initial motion is

$$\begin{aligned} |\Delta\vec{p}|_{\perp r} &= \int_{-\infty}^{\infty} \frac{2\alpha_p e^2 b}{(v_r^2 t^2 + b^2)^{3/2}} dt \\ &= \frac{3\pi\alpha_p e^2}{4v_r b^4}; \end{aligned} \quad (3.35)$$

the parallel component vanishes. The scattering angle $\theta(b)$, which is a function of the impact parameter, is given in this approximation

by

$$\theta(b) = \frac{|\Delta \vec{p}|}{|\vec{p}|}, \quad (3.36)$$

where $\vec{p} = \mu \vec{v}_r$ is the initial momentum. The differential cross section--the number of particles scattered into solid angle $d\Omega$ at θ per unit time, divided by the incident intensity--is

$$\frac{d\sigma}{d\Omega} = \frac{b}{\sin \theta} \left| \frac{db}{d\theta} \right|. \quad (3.37)$$

Calculation of b and $db/d\theta$ as functions of θ from Equations 3.35 and 3.36 yields a cross section

$$\frac{d\sigma}{d\Omega} = \left(\frac{3\pi\alpha_p e^2}{64\mu v_r^2} \right)^{1/2} \theta^{-5/2}. \quad (3.38)$$

Both the scattering angle θ and the differential cross section $d\sigma/d\Omega$ (Equations 3.36 and 3.38) are in the center of mass reference frame. They are related to measured quantities through a center-of-mass to laboratory frame transformation. The transformation equations are given by Goldstein (G8), who shows that the scattering angles θ and θ_L in the center-of-mass (c.m.) and laboratory (lab) frames, respectively, are related by

$$\tan \theta_L = \frac{\sin \theta}{\cos \theta + m_1/m_2}. \quad (3.39)$$

The differential cross sections are related by

$$\frac{d\sigma}{d\Omega}|_{\text{lab}} = \frac{d\sigma}{d\Omega}|_{\text{c.m.}} \frac{\sin \theta}{\sin \theta_L} \frac{d\theta}{d\theta_L} \quad (3.40)$$

For small angles, Equations 3.39 and 3.40 may be approximated by

$$\theta_L \approx \frac{\theta}{1 + m_1/m_2} \quad (3.41)$$

and

$$\frac{d\sigma}{d\Omega}|_{\text{lab}} \approx \frac{d\sigma}{d\Omega}|_{\text{c.m.}} \left(\frac{m_1 + m_2}{m_1} \right)^2 \quad (3.42)$$

Substitution of Equations 3.31, 3.41 and 3.42 into Equations 3.38 yields

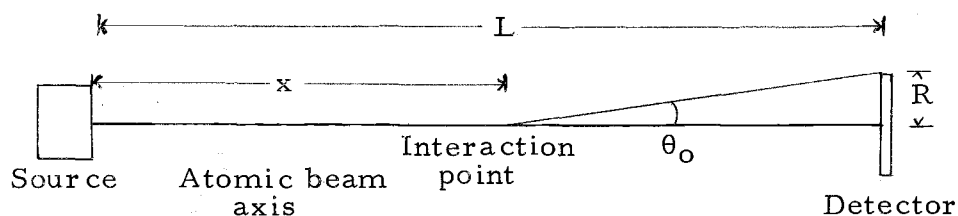
$$\frac{d\sigma}{d\Omega}|_{\text{lab}} \approx \left(\frac{3\pi\alpha_p e^2}{64m_1 \theta_L^5} \right)^{1/2} \frac{1}{v_r} \quad (3.43)$$

The effect of the center-of-mass to laboratory frame transformation in this case has been to replace the reduced mass by the incident particle mass m_1 .

The HR source and detector arrangement used in the present experiment is illustrated in the diagram below. The differential cross section in Equation 3.43 is integrated over scattering angles θ_L , from θ_0 , the half angle subtended by the detector at the interaction point, to some larger value θ' . This gives the cross section σ_x for scattering of atoms out of the beam from a point which is at a

distance x from the detector:

$$\sigma_x(\theta_o) = \int_{\theta_o}^{\theta'} \frac{d\sigma}{d\Omega} \Big|_{\text{lab}} 2\pi \sin \theta_L d\theta_L. \quad (3.44)$$



$$\theta_o \approx \frac{R}{L-x}$$

The cross section σ_x is then integrated over all the interaction locations along the beam to give an effective cross section $\sigma(v)$.

The effective cross section for an infinitesimal beam length dx is

$$d\sigma = \sigma_x \frac{dx}{L}, \quad (3.45)$$

which yields

$$\sigma(v) = \int d\sigma = \frac{1}{L} \int_0^L \sigma(\theta_o = \frac{R}{L-x}) dx. \quad (3.46)$$

Finally, performance of the integrations in Equations 3.44 and 3.46 gives

$$\sigma(v) = \frac{1}{v_r} \left(\frac{\pi^3 \alpha_p e^2 L}{3m_1 R} \right)^{1/2}. \quad (3.47)$$

Because θ' is large, it does not appear in Equation 3.47.

The collision frequency may now be found by integration over the Maxwell-Boltzmann velocity distribution $d^3 \vec{n}_0 / d^3 \vec{v}_2$ for the target gas. With the use of Equation 3.32, the cross section may be written as

$$\sigma(|\vec{v}_1 - \vec{v}_2|) = \frac{K}{|\vec{v}_1 - \vec{v}_2|}. \quad (3.48)$$

If P is the population of excited atoms in the beam at time t , the loss of population for atoms with relative velocity v_r in a short distance $dx (= v_r dt)$, is $P\sigma v_r dt$. When averaged over all target atom velocities, the fractional loss of probability becomes

$$\frac{dP}{P} = - \left[\int \frac{d^3 \vec{n}(\vec{v}_2)}{d^3 \vec{v}_2} d^3 \vec{v}_2 \frac{K}{|\vec{v}_1 - \vec{v}_2|} |\vec{v}_1 - \vec{v}_2| \right] dt. \quad (3.49)$$

The quantity in square brackets is the gas kinetic collision frequency. This integral is simplified by the $1/v_r$ dependence of σ ; it yields immediately

$$\frac{dP}{P} = -[Kn_0]dt, \quad (3.50)$$

where n_o is the target gas density. At a constant pressure Equation 3.50 predicts an exponential rate of signal loss:

$$P = P_o e^{-Kn_o t}, \quad (3.51)$$

where $K = \sigma v_r$, P_o is the initial population, and t is the flight time.

In the absence of radiative decay and collision-induced changes of state, the scattering cross sections can be obtained from the TOF spectra. The procedure for doing this will be described in Section 6.2. If $R_p(t)$ is the ratio of a spectrum obtained at high pressure to that obtained at a lower pressure but at the same electric field, then it is expected that

$$R_p(t) = e^{-\gamma t}. \quad (3.52)$$

Experimentally γ/n_o is accessible, and from Equations 3.47, 3.48, 3.50 and 3.51 it is seen that

$$\sigma v_r = \gamma/n_o = \left(\frac{\pi^3 \alpha_p e^2 L}{3m_1 R} \right)^{1/2}. \quad (3.53)$$

Equation 3.53 allows comparison of σv_r obtained from the theory with that obtained from experiment (γ/n_o), provided the effect of scattering can be separated from radiative decay and collision-induced

state changes. That this is in fact the case will be shown in Section 6.3.

3.4 Model for Time-of-Flight Distributions with Introduced Target Gases

The shapes of time-of-flight spectra obtained with introduced target gases and applied electric fields should be governed by radiative decay, collisional state changes, deflections, and field ionization. A simple model is now proposed in an effort to explain the shapes of the TOF spectra for a beam of HR atoms, obtained with introduced target gases. No attempt is made at calculating the exact initial HR state distribution $P(n, \ell)$. Since excitation in the present experiment is well above threshold, predominantly low- ℓ states are produced initially. Modification of $P(n, \ell)$ takes place because of the effects listed above, as the excited beam proceeds from the excitation region to the detector.

It has been shown in Section 3.2 that the probabilities for state-changing collisions in which $\Delta n > 0$ are much smaller than those for which $\Delta n = 0$. It is therefore assumed in this model that the ℓ -changes constitute the major collision-induced internal state changes. A given (n, ℓ) state is both depleted and repopulated by ℓ -changing collisions with ground state lithium atoms and target gas atoms. A simple kinetic theory calculation shows that at the

experimental background pressure of approximately 2×10^{-6} Torr the contributions of these two processes are comparable.

In these $\Delta\ell$ collisions it is assumed that all available states are equally likely. No restrictions are put on the magnitude of $\Delta\ell$; in particular the selection rule $\Delta\ell = \pm 1, 0$ is assumed not to apply. This assumption will be discussed further in Section 6.3. It is thus seen that the rate at which a given (n, ℓ) state is populated depends on the degeneracy $(2\ell+1)$ of that state, as well as on the current population of the other states having the same n . The rate at which the ℓ -state gets depopulated depends not only on the population of that state, but also on the total number of substates having the same n . Thus, for excited lithium atoms having velocity v , the change in the (n, ℓ) population after passage through a small flight path dx is

$$dP_{\Delta\ell}(n, \ell, t) = \left\{ n_0 \sigma^{\Delta\ell} \left(\frac{2\ell+1}{n} \right) \sum_{\ell'=0}^{n-1} P(n, \ell', t) - n_0 \sigma^{\Delta\ell} P(n, \ell, t) \sum_{\ell'=0}^{n-1} \frac{2\ell'+1}{n} \right\} dx, \quad (3.54)$$

where \sum' implies that the summation does not include $\ell' = \ell$.

Equation 3.54 simplifies to

$$dP_{\Delta l}(n, l, t) = n_0 \sigma^{\Delta l} v \left[\frac{2l+1}{n} \sum_{l'=0}^{n-1} P(n, l', t) - P(n, l, t) \right] dt. \quad (3.55)$$

The change in $P(n, l, t)$ due to collisions which result in the deflection of the HR Li atoms out of the beam is

$$dP_s(n, l, t) = -n\sigma^s v P(n, l, t) dt. \quad (3.56)$$

Collisions which deflect excited atoms back into the beam are not considered in this model. That such collisions make a negligible contribution to the signal can be seen from solid angle considerations alone.

The excited Li atoms may also decay spontaneously in flight. Low- l states decay faster than high- l states. Cascade effects are not included in this model, but will be discussed in Section 6.1; thus an excited atom is assumed to decay to low-lying states not detectable in this experiment. The contribution to the change in $P(n, l, t)$ due to radiative decay may be written as

$$dP_{\Gamma} = -\Gamma_{nl} P(n, l, t) dt. \quad (3.57)$$

Equations 3.55, 3.56 and 3.57 are now added to give the basic differential equation for this model:

$$dP(n, \ell, t) = \left\{ -n_0 \sigma^{\Delta \ell} v \left[P(n, \ell, t) - \frac{2\ell+1}{n} \sum_{\ell'=0}^{n-1} P(n, \ell', t) \right] - n_0 \sigma^S v P(n, \ell, t) - \Gamma_{n\ell} P(n, \ell, t) \right\} dt \quad (3.58)$$

The experimental results to be described in Chapter 6 provide evidence that σ^S does not depend on n or ℓ . With this assumption $P(n, \ell, t)$ may be written as a product of two functions:

$$P(n, \ell, t) = e^{-n_0 \sigma^S vt} Q(n, \ell, t), \quad (3.59)$$

where the exponential factor describes scattering and Q depends on radiative decay and ℓ -changing collisions. Substitution of Equation 3.59 into Equation 3.58 gives a differential equation for Q :

$$dQ(n, \ell, t) = \left\{ \left[\frac{2\ell+1}{n} \sum_{\ell'=0}^{n-1} Q(n, \ell', t) - Q(n, \ell, t) \right] n_0 \sigma^{\Delta \ell} v - \Gamma_{n\ell} Q(n, \ell, t) \right\} dt. \quad (3.60)$$

In the Appendix a numerical method for solving 3.58 is fully described, together with model calculations with the restrictions $\Delta \ell = \pm 1$ or 0 . In Section 6.3 the predictions of these models are compared with observed TOF spectra. A two-state version of the unrestricted model will now be described in full. In this form the differential equations can be solved analytically and the solution aids

visualization of the physical processes leading to the observed spectra.

The two states to be labelled $|1\rangle$ and $|2\rangle$ are assumed to be ℓ -sublevels of the same principal quantum state n . State $|1\rangle$ is a low- ℓ state, such as an s and p state, which has a low degeneracy and decays radiatively with a decay rate Γ . State $|2\rangle$ is a high- ℓ state with a large degeneracy g , which has a negligible decay rate. The rates of change of the Q -functions for $|1\rangle$ and $|2\rangle$ are given by Equation 3.60. If $Q_1(t)$ and $Q_2(t)$ represent the Q -functions for states $|1\rangle$ and $|2\rangle$, then

$$\left. \begin{aligned} \frac{d}{dt} Q_1(t) &= -(\alpha_1 + \Gamma)Q_1(t) + \alpha_2 Q_2(t) \\ \frac{d}{dt} Q_2(t) &= \alpha_1 Q_1(t) - \alpha_2 Q_2(t) \end{aligned} \right\}, \quad (3.61)$$

where

$$\left. \begin{aligned} \alpha_1 &= n_o \sigma^{\Delta \ell} v \frac{g}{g+1} \\ \alpha_2 &= n_o \sigma^{\Delta \ell} v \frac{1}{g+1} \end{aligned} \right\}. \quad (3.62)$$

It is noted that $\alpha_1 \gg \alpha_2$ for large g .

The set of coupled differential equations in Equation 3.61 describes the loss of probability from state $|1\rangle$ by radiative decay, as well as the transfer of probability between states $|1\rangle$ and $|2\rangle$ by means of ℓ -changing collisions. Initially, all of the probability is in the low- ℓ state. Thus,

$$\left. \begin{aligned} Q_1(0) &= 1 \\ Q_2(0) &= 0 \end{aligned} \right\} \quad (3.63)$$

With these conditions, Equation 3.61 has solutions

$$\left. \begin{aligned} Q_1(t) &= \frac{\alpha_1 + \Gamma - \beta^-}{\beta^+ - \beta^-} e^{-\beta^+ t} + \frac{\beta^- - \alpha_1 - \Gamma}{\beta^+ - \beta^-} e^{-\beta^- t} \\ Q_2(t) &= \frac{-\alpha_1}{\beta^+ - \beta^-} (e^{-\beta^+ t} - e^{-\beta^- t}) \end{aligned} \right\} \quad (3.64)$$

with

$$\beta^\pm = \frac{1}{2} [(\alpha_1 + \alpha_2 + \Gamma) \pm \sqrt{(\alpha_1 + \alpha_2 + \Gamma)^2 - 4\alpha_2 \Gamma}]. \quad (3.65)$$

The observed signal is the sum of the populations in states $|1\rangle$ and $|2\rangle$. The associated Q-function Q_p is given by

$$\begin{aligned} Q_p(t) &= Q_1(t) + Q_2(t) \\ &= \frac{1}{\beta^+ - \beta^-} [(\Gamma - \beta^-) e^{-\beta^+ t} + (\beta^+ - \Gamma) e^{-\beta^- t}], \end{aligned} \quad (3.66)$$

where the subscript on Q_p denotes the presence of a target gas at pressure p . The p -dependence of Q_p is through the target gas densities n_0 in α_1 and α_2 . From the experimental transit-time distributions the quantity $F(t)$, which is the ratio of Q_p with and without target gas pressure, can be extracted. From Equations 3.66,

$F(t)$ is seen to be

$$F(t) = \frac{Q_p(t)}{Q_o(t)} = \left(\frac{\beta_o^+ - \beta_o^-}{\beta_p^- - \beta_p^+} \right) \frac{(\Gamma - \beta_p^-) e^{-\beta_p^+ t} + (\beta_p^+ - \Gamma) e^{-\beta_p^- t}}{(\Gamma - \beta_o^-) e^{-\beta_o^+ t} + (\beta_o^+ - \Gamma) e^{-\beta_o^- t}}, \quad (3.67)$$

where the subscript o indicates the absence of target gas. With the approximation $\alpha_2 \ll \alpha_1$, it is easily seen that

$$\beta^+ \approx \Gamma + \alpha_1 \quad \text{and} \quad \beta^- \approx \frac{\alpha_2 \Gamma}{\alpha_1 + \Gamma}, \quad (3.68)$$

so that

$$\beta^+ - \beta^- \approx \alpha_1 + \Gamma. \quad (3.69)$$

Substitution of Equations 3.68 and 3.69 into 3.67 easily yields

$$F(t) = \left(\frac{\alpha_o + \Gamma}{\alpha_p + \Gamma} \right) \frac{\Gamma e^{-(\alpha_p + \Gamma)t} + \alpha_p}{\Gamma e^{-(\alpha_o + \Gamma)t} + \alpha_o}. \quad (3.70)$$

Since α_2 does not appear in the result, the subscript 1 on α_1 has been dropped in Equation 3.70. This expression will be used in Section 6.4, where an approximate value of the ℓ -changing cross section will be determined.

4. APPARATUS

In the present experiment a beam of excited lithium atoms is produced by electron impact and studied by time-of-flight analysis. This requires an appropriate excited-atom source, a single-particle detection system, and digital electronics for time measurements. The various components will now be described.

4.1 Vacuum System

Figure 5 shows the layout of the apparatus. The outer vacuum chamber is nonmagnetic, of copper construction. The circular source chamber, about 32 cm in diameter and about 5 cm thick, fits snugly between the poles of a research electromagnet (Magnion model 128A). Electrical power to the magnet is provided by a high-current (up to 80 amps) power supply (Varian model V2900). Only nonmagnetic screws and bolts are used inside the source chamber. Greased Viton O-ring seals are used throughout. The system is evacuated by two silicone-oil diffusion pumps (Edwards Speedivac model QSB2) with thermo-electrically cooled baffles (Speedivac model DCB2A) to a base pressure of about 2×10^{-6} Torr. The pumps, with 5-cm pumping apertures, are suspended from the ends of cylindrical tubes attached to the source chamber. Since the pumping is accomplished through apertures of limited conductance, filling the

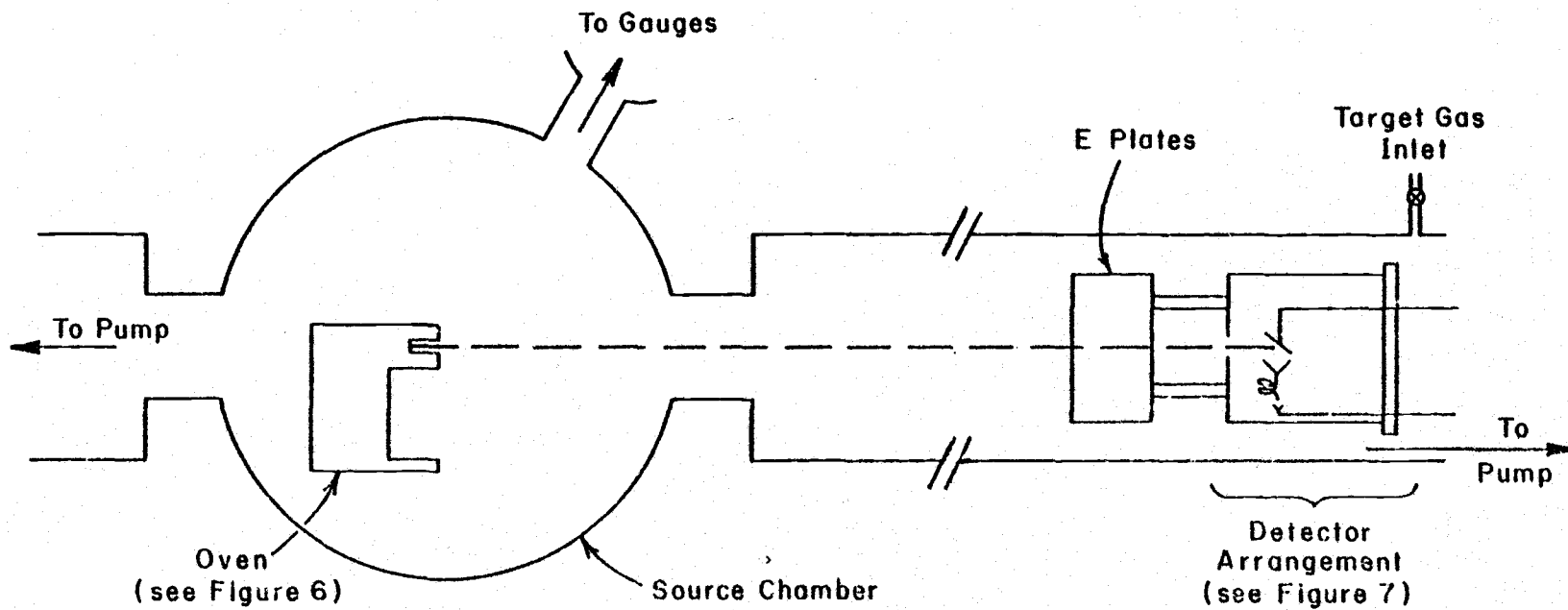


Figure 5. Layout of apparatus. (Not to scale.)

liquid nitrogen traps attached to the diffusion pumps reduces the base pressure by only a factor of about 2.

Target gases can be admitted through a Granville-Phillips Variable leak valve (Series 203). The variable leak valve is connected to the system by means of a T-type connection, so that when a different target gas is to be used, the gas inlet lines can be evacuated and refilled several times. This successive filling prevents excessive mixing of target gases. When let in, the target gas fills the entire chamber. Pressure is measured by a Bayard-Alpert-type ionization gauge (Veeco RG-75 gauge tube with RG-21X electronics) calibrated by a capacitance manometer (MKS Baratron model 310BHS-1 sensor with 170M-6B readout). The measured ionization-gauge correction factors f for various target gases are in good agreement with accepted values (Dushman D2), as shown in Table 1. After a run, Li deposits on chamber walls and on guard plates are wiped off with distilled water and then with acetone. (Li reacts with water, giving off hydrogen and soluble lithium hydroxide.) The source chamber is water cooled during operation.

Protective pressure and water interlocks are provided. If the cooling water to the two diffusion pumps is cut off or the pressure gets too high, the diffusion pumps are automatically turned off. A 30-second time-delay switch turns the system back on in case of a momentary power failure.

Table 1. Measured ionization-gauge correction factors f for target gases used in this experiment and for air. The Dushman and Young values are included for comparison.

$$f = \frac{\text{ionization gauge sensitivity for gas}}{\text{MKS Baratron gauge sensitivity}}$$

Gas	This Experiment	Dushman and Young*
He	0.15	0.13
Ne	0.27	0.20
Ar	1.00	1.00
H ₂	0.45	0.39
N ₂	0.78	0.84
NH ₃	0.72	--
air	0.67	--

* Obtained from Ref. D2.

Evacuation of the system follows a standard procedure. First, a mechanical pump (Cenco HYVAC 7) removes most of the air through a roughing valve above the main valves to the diffusion pumps. The high pressure lines of the diffusion pumps (forelines) are evacuated next. Electrical power is then applied to the oil heaters of the diffusion pumps, but their inlet valves are kept closed during this operation. The roughing line is valved off, the main valves to the diffusion pumps are opened, and the ionization gauge power supply is turned on, while evacuation of the fore-line by the mechanical pump is continued. The pressures in the roughing line (during pump-down) and in the forelines are monitored by thermocouple gauges (General Electric model MP 182088).

4.2 Atomic Beam Oven

Figure 6 shows the essential features and dimensions of the lithium oven and the electron gun. Construction of this molybdenum oven follows general oven design principles outlined by Ramsey (R4). The access plug (about 1 cm in height and of tapered construction) is bored and threaded from its top for easy removal. The removal hole is external to the sides of the plug that fits into the well. The cylindrical well has a 1-cm diameter and a 4-cm depth; the channel diameter is 3 mm. The oven is heated by means of Sylvania radio tube heaters of zig-zag geometry and made from tungsten wire, 0.013 cm thick. These heaters (six for the channel and 16 for the well) are coated with aluminum oxide and placed within ceramic tubes of 2 mm outer diameter. A well heater is 2.5 cm in length, while a channel heater is 5 cm in length. The heaters are interconnected by spotwelding to intermediate tantalum wires and then brought out to two pairs of terminals on a boron nitride terminal block mounted at the back of the oven. Combined cold resistances are 7Ω and 9Ω for the channel and well heaters, respectively. The heaters are controlled by separate power supplies, and under normal operating conditions these heaters together dissipate up to 120 W.

The mounting base plate for the oven is thermally insulated from the rest of the oven by long, thin stainless steel mounting

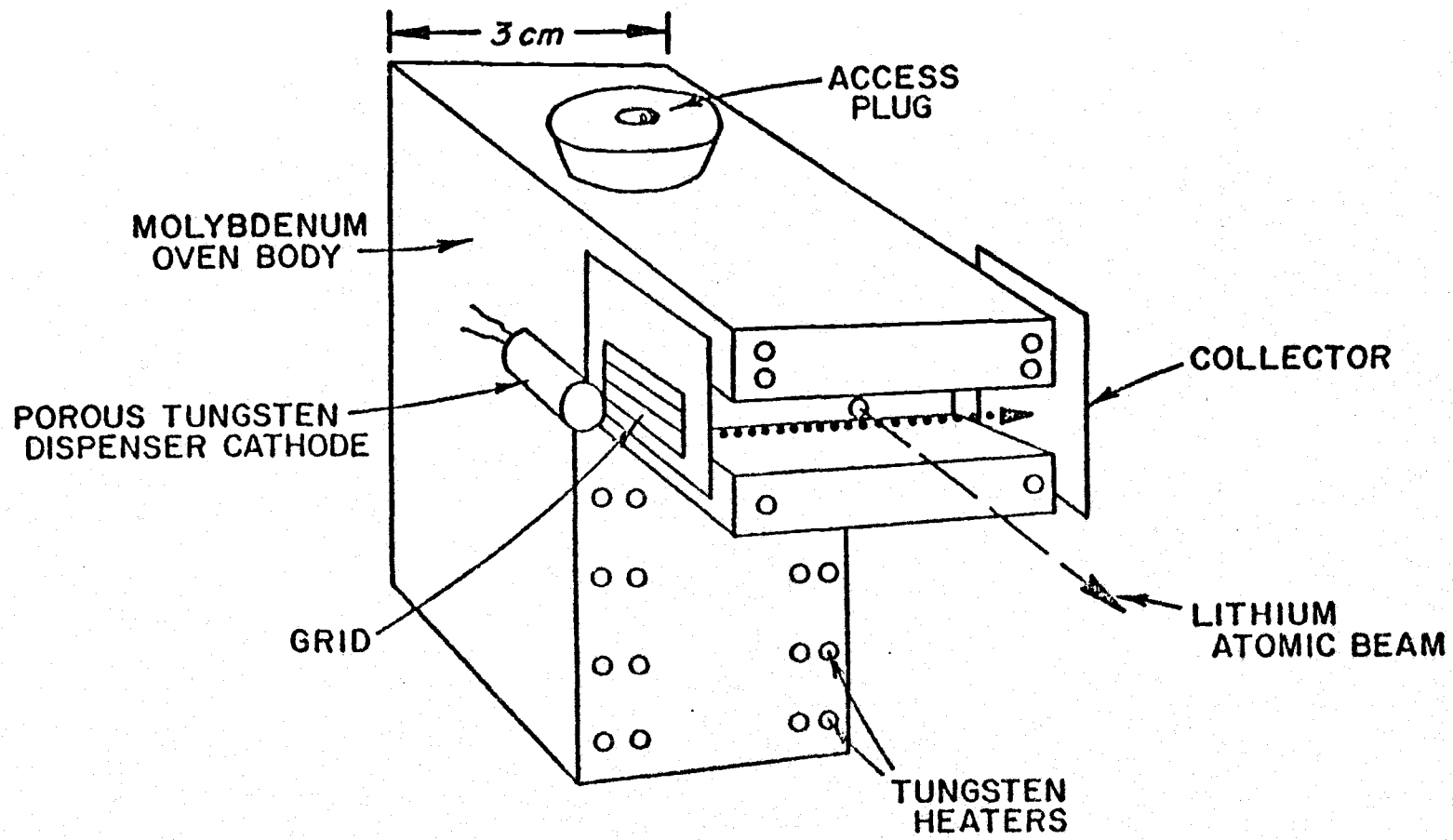


Figure 6. Atomic beam oven and electron gun configuration.

screws, and the base plate is isolated from the chamber by a slab of boron nitride. The operating temperature is about 500°C, monitored by a copper-constantan thermocouple inserted in a small hole at the back of the oven.

A full oven load consists of approximately 1 gm of Li. At an operating temperature of 500°C, a simple kinetic theory calculation shows that about 100 hours of running time should be expected for each full load. The actual number of days the experiment can be run is increased considerably, since the oven is kept at a standby temperature of 300°C when data are not being acquired. The vapor pressure of Li at 300°C is 10^{-6} Torr. When the oven is brought to operating temperature from shutdown or standby conditions, the channel is kept hotter than the well, so that it will not be blocked by condensed lithium. During normal operation, the channel is also kept at a higher temperature for the same reason. A copper shield around the oven is cooled by a copper stem which is externally maintained at liquid nitrogen temperature.

4.3 Electron Gun

The electron gun, also shown in Figure 6, includes a porous tungsten dispenser cathode (Philips type, manufactured by Spectromat), a grid, and a collector. The cylindrical cathode is 0.5 cm in diameter and 1 cm in length and is emissive on all of its surface

except an open end through which a coiled tungsten heater can be inserted. Up to 15 W of power can be dissipated in the heater. The following procedure was found to be the most effective for activating the cathode. The cathode is heated to and maintained at a high temperature for 5 min and then cooled to allow it to acquire a coating of lithium. It is then brought up slowly to the operating conditions of 4 V at 1 A on the heater. Lithium, having a low work function, interacts with the cathode material, making the latter several times more emissive. This is apparent from the fact that as the cathode's temperature is increased beyond the optimum value, its emissivity decreases. Under dc operation, with an accelerating potential of -120 V applied to the cathode, electron currents to the collector (at 20 V) of up to 10 mA have been measured. These electrode voltages are measured with respect to the oven, which is electrically grounded to the chamber walls.

4.4 State Selector

Electron impact excitation is non-selective with respect to the Rydberg states produced. Electric field ionization (Section 2.2) is used for state selection. Figure 7 shows the electric field plates and excited-atom detector configuration. Equal positive and negative potentials with respect to the chamber wall as ground are applied to the plates to ensure a zero potential on the atomic beam symmetry

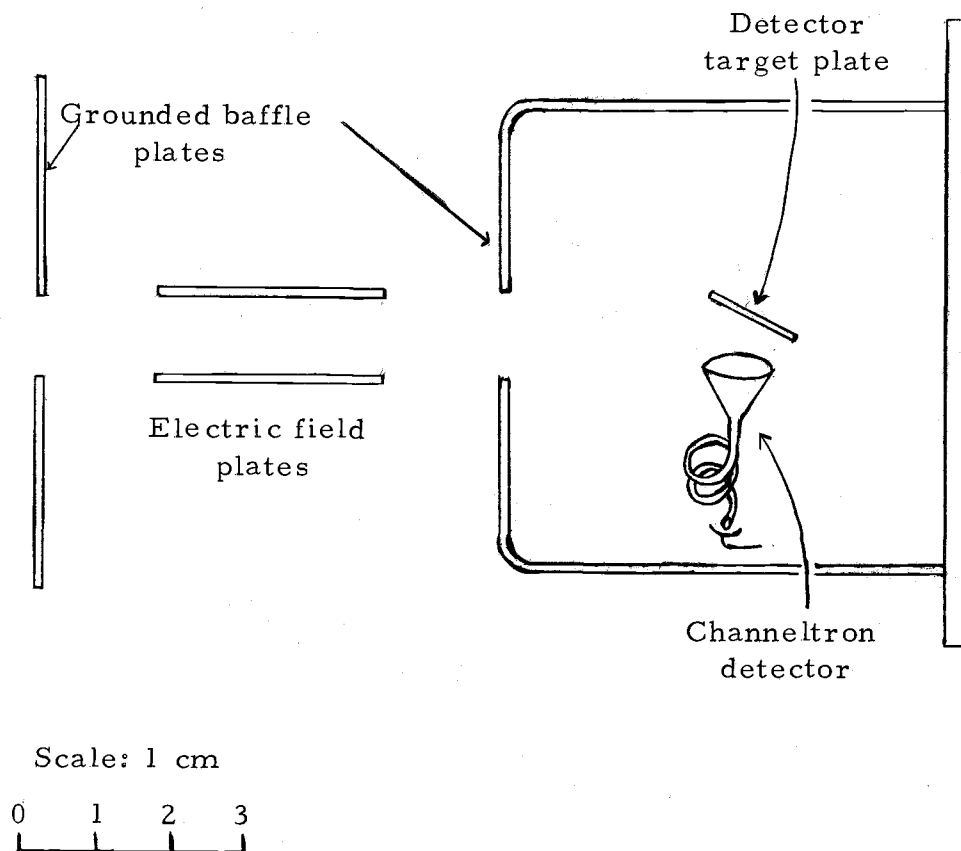


Figure 7. Excited-atom detector and electric-field-state selector. Diagram is nearly to scale.

axis. With the plates at a 1.0-cm separation, the resulting transverse field is nearly uniform over the 3-cm extent (along the beam) of the plates. Electric field strengths up to 5.0 kV/cm were employed with this setup.

In passing through the plates, all HR states with principal quantum numbers $n \geq n_c$, where $n_c = (F_o/F)^{1/4}$, are field ionized, as discussed in Section 2.2. The resulting ions and electrons are attracted out of the beam. In this manner a range of principal quantum numbers $n_{\min} \leq n \leq n_c$ is selected for study. The lower limit n_{\min} is determined by radiative decay along the 35-cm beam flight path as discussed in Section 3.1. As the electric field is turned up, it is expected that the observed signal should decrease as a result of the removal of HR atoms with large n -values.

4.5 Excited-Atom Detector

HR atoms which survive in the beam ($n_{\min} \leq n \leq n_c$) are ionized by an electric field ≈ 5 kV/cm between a 1-cm² copper target plate and the cathode of a continuous channel electron multiplier (Galileo Channeltron model 4028). The resulting ions are accelerated toward the input cone of the Channeltron and counted. The detector configuration is shown in Figure 7 and the Channeltron circuitry in Figure 8. The Channeltron (E2) is essentially a helical capillary tube (glass construction, 1 mm in diameter) with a cone-shaped cathode at

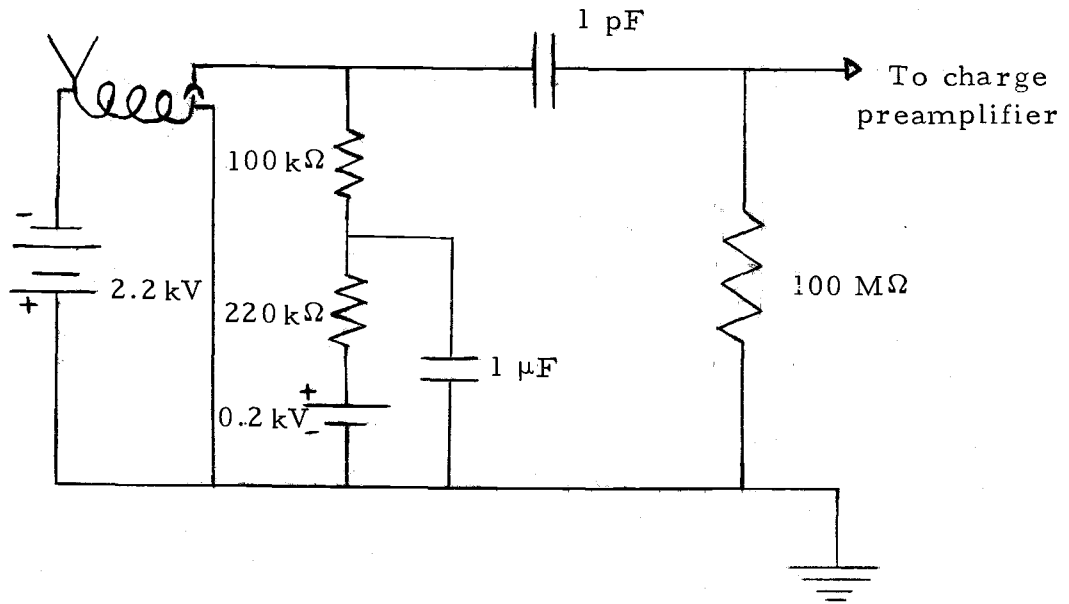


Figure 8. Channeltron circuit.

one end. The interior of the capillary tube is coated with a layer of special semiconducting metallic oxide with favorable secondary emission characteristics. A secondary electron emitted from the surface is accelerated axially by a potential difference applied at the ends of the tube. Since an electron is emitted with a transverse velocity (with kinetic energy of order 1 eV), it soon collides with the surface, creating secondary electrons. Electron multiplication occurs if on the average more than one secondary electron is generated for every collision. The result is a charge pulse at the collector (an external electrode 1 mm from the Channeltron end and biased positive with respect to it) for every ion that collides with the cone of the Channeltron. This charge pulse is typically 10^{-12} C. At a typical Channeltron operating voltage of 2.5 kV the electron gain is of order 10^7 . Under these conditions the Channeltron is gain saturated such that single charged particles entering the input mouth will initiate output pulses whose amplitude and shape are both uniform and independent of the character of the incident particle. The output pulse width is 20 nsec at a gain of 3×10^7 , and the pulse height distribution is approximately Gaussian with a full width at half maximum of 50% at a gain of 5×10^7 .

One advantageous characteristic of the Channeltron with respect to this experiment is that its electron gain is insensitive to pressure variations below 10^{-3} Torr (E2). Though this conclusion was arrived

at for a curved Channeltron, it has been checked and found to hold for the helical type. In this experiment the Channeltron pulse-height distribution was monitored and found to be independent of target gas pressures up to 4×10^{-4} Torr. Another advantage is that the semi-conducting metal oxide has a work function of approximately 4 eV. Thus, the channel has virtually no response to light of wavelengths longer than 1500 Å and essentially no background noise due to thermionic emission of electrons. The sensitivity is nearly 100% for charged particles. The Channeltron with no high voltage applied is not adversely affected by exposure to air.

4.6 Signal Electronics

The primary information obtained in the present experiment is in the form of time-of-flight spectra. Figure 9 shows a block diagram of appropriate electronic circuitry for acquisition of such data.

The current pulse from the Channeltron is converted into a voltage pulse by a charge-sensitive preamplifier (Hewlett-Packard model 5554A). This voltage pulse is amplified by a linear amplifier (Tennelec model TC 213) with an adjustable gain of up to 640. The amplified voltage pulse is fed through an integral discriminator which produces a shaped pulse (rectangular shape, 0.5-μsec duration, 4-V amplitude) if the input voltage pulse is larger than a selectable discrimination (threshold) voltage. The discriminator output is

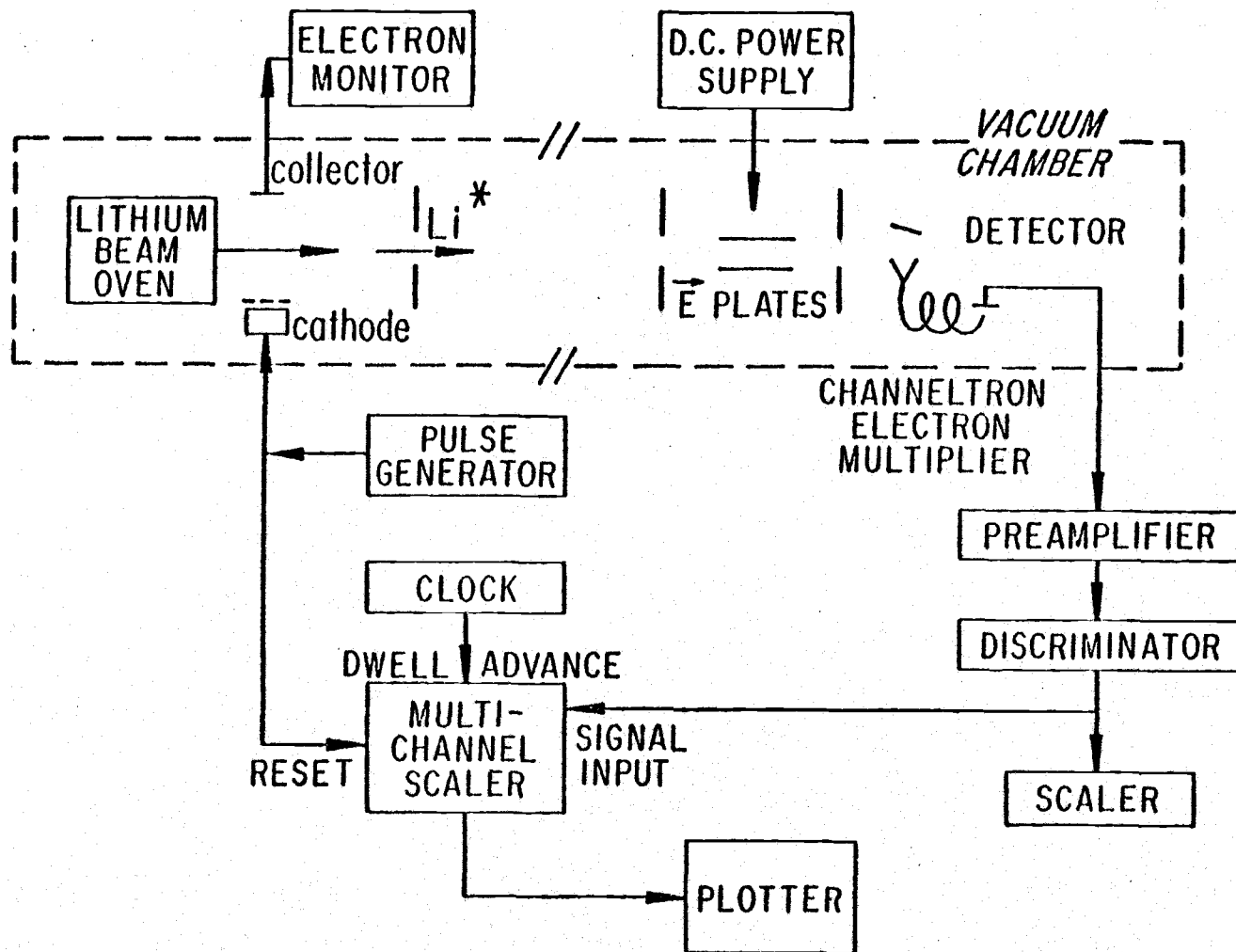


Figure 9. Experimental configuration.

monitored by a precision ratemeter (Tennelec model TC 590) and a six decade scaler (Tennelec model TC 550). The ratemeter monitors the discriminator output for long term drifts in the apparatus.

A simple procedure was used to discriminate against low-level noise from power supplies and various other electronic components. With the cathode pulse removed, the Channeltron at operating voltage, and the oven at operating temperature, the discriminator threshold was set at the lowest setting for which no counts were recorded on the scaler. The cathode pulse was then restored and the amplifier gain and Channeltron high voltage adjusted until the count rate became insensitive to further change in the parameters, over wide ranges. At these settings essentially all of the electronic pulses were being counted. The final high voltage and amplifier gain are such that the amplifier output pulses are not clipped.

The shaped pulses from the discriminator are also applied to the input of a pulse-height analyzer (Tracor-Northern model 1705) operated as a multichannel scaler. In this mode the input pulses are catalogued according to arrival time. The analyzer dwell time of $5.5 \mu\text{sec}/\text{channel}$ is externally derived from a pulse generator constructed in our laboratory. The address reset pulse is synchronized with the cathode pulse which excites the high Rydberg lithium states. The stored counts in each channel are displayed on an oscilloscope (Tektronix model 5103-N) which provides a live display of data during

acquisition. The analyzer memory may be printed out and punched onto paper tape by a Teletype model ASR-33 for processing afterwards on the CDC 3300 computer run by Oregon State University. An X-Y plotter can provide additional graphic display of the TOF spectra.

4.7 Preparations for a Run

Lithium oxidizes when exposed to air for long periods; long use and long exposure of the porous tungsten dispenser cathode does render it less emissive. A cathode will function well during the first run in which it is used and adequately during the second, after which it must be replaced. In the preparation of the system for a new run, the following sequence of events is adopted.

When the cover flange of the chamber is removed after a run, the chamber walls and various plates are wiped clean with distilled water and then with acetone. The Li beam oven is then cleaned by the scraping away of Li deposits, which tend to cause shorts between various electrodes if not removed. Care must be taken to avoid any contact with the oven heaters, which become brittle from operating at high temperatures over long periods of time. The resistances are checked and open circuits are repaired with care, or one might have to replace a whole series of heaters in the process of repairing a single break in the circuit. Next, the cathode and cathode heaters are replaced by spotwelding them to mounting posts provided for this

purpose. Lastly, a piece of lithium is cut out, simply pressed into shape and the unused metal stored in an evacuated desiccator. The well is then loaded and the plug pressed into place firmly to prevent the escape of lithium vapor around the sides of the well opening. The chamber is immediately covered, placed between the poles of the magnet and its evacuation started. Evacuation may take several days--up to 7 days--depending on how long the system had been exposed and on how clean it had been kept.

When the pressure is in the 10^{-6} range, the oven temperature may be brought up, very slowly at first. As the oven heats up, it emits vapors (including H_2O and organic), and care must be taken to keep the pressure well below 10^{-4} Torr. When the oven temperature is at its operating value, and the base pressure is down to 2×10^{-6} Torr, the cathode may be activated as described in Section 4.3. The Channeltron operating voltage is then applied, the discriminator threshold is set as described in Section 4.7, the cathode pulse characteristics (10-V amplitude, 10- μ sec duration, 870-Hz repetition rate) are established and the analyzer dwell-time pulse is applied. The system is then ready for the acquisition of time-of-flight spectra.

5. EXPERIMENTAL PROCEDURES

Time-of-flight spectra for a beam of excited atoms contain information about their initial velocity distribution, the initial population distribution, and in-flight modification of the population distribution by radiative decay and collision processes. In this chapter general procedures for obtaining TOF spectra are described. The precautions taken during acquisition of spectra with applied electric fields and introduced target gases are also discussed.

5.1 Preliminary Measurements

A preliminary investigation was carried out with a view to producing HR lithium atoms and observing their ionization in electric fields. For this run only, the exciting electrons were accelerated by means of a dc potential of up to 10 V on the cathode. The purpose of dc rather than pulsed mode was to ensure a continuous density of exciting electrons so that large numbers of Li atoms could be excited. The resulting Li* beam passed through a grounded aperture and a pair of electric field plates before entering a grounded detector aperture. The electric field plates are also grounded for zero-field measurements, ensuring a field-free flight path up to the detector aperture.

The detector in this run consisted of a biased copper plate of area approximately equal to 1 cm^2 , attached to an operational

amplifier as shown in Figure 10. The Rydberg atoms are surface-ionized at the target plate (Section 2.6), and the resulting ion current is measured.

Figure 11 shows the variation of the ion signal with cathode voltage, and the inset shows relevant parameters. The magnetic field focuses the exciting electrons and removes ions and electrons from the atomic beam. Since the first ionization potential of Li is 5.4 eV, the occurrence of an observed threshold for low electron currents at about 5.5 eV is very satisfying. The width of the threshold increases with increasing collector current, probably because of space charge effects in the electron beam. From retarding potential measurements the spread in energy of the exciting electrons has been observed to be about 3 eV when emission exceeds 10 mA. The reduction of the HR ion signal with increasing electric field will be discussed in Section 6.1.

The rate of escape of atoms from the oven (diameter of opening = 0.3 cm) is estimated to be 1.7×10^{17} atoms/sec, since the vapor pressure of lithium at 500°C is about 3.6×10^{-3} Torr. From the inverse square law, the rate at which ground-state atoms enter the detector aperture (35 cm from the source, 1 cm in diameter) is $\frac{dN}{dt} = 3.5 \times 10^{13}$ atoms/sec. For a typical counting rate integrated over all channels $\frac{dN^*}{dt} = 1 \times 10^3$ counts/sec, at a duty cycle of 1/100, the excitation probability is

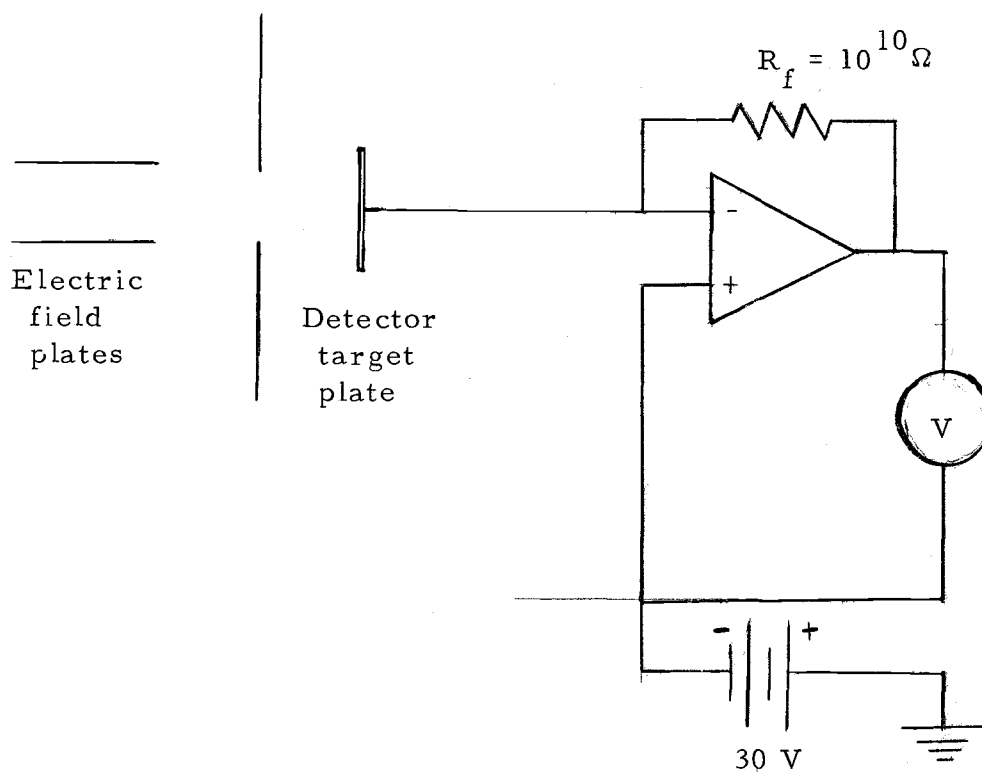


Figure 10. Detector and operational amplifier circuit for dc measurements. The 30 V bias appears on the detector target plate.

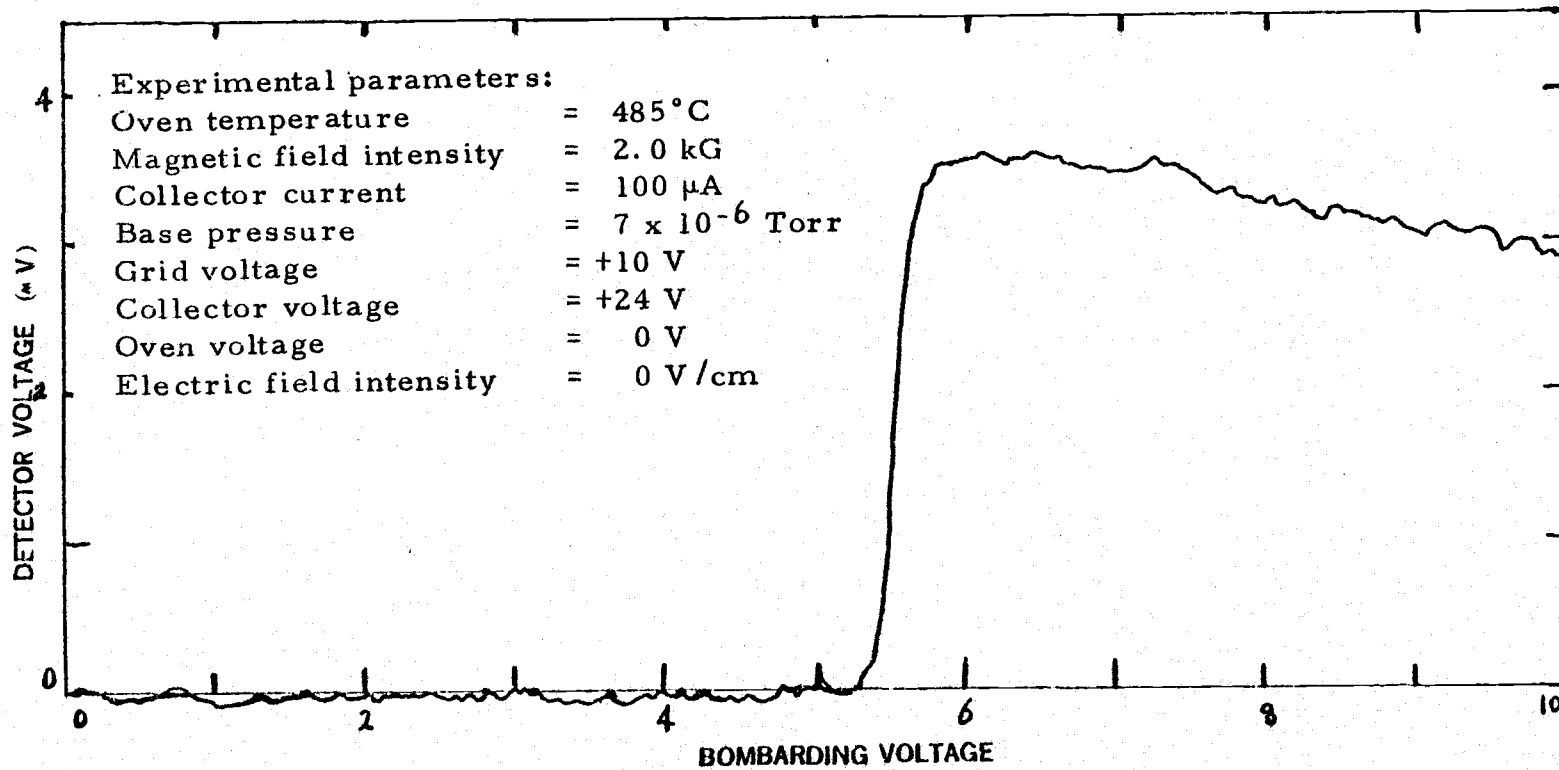


Figure 11. High Rydberg lithium excitation function. This curve was obtained directly as the output of the x-y plotter.

$$P_E = \frac{100 \, dN^*/dt}{dN/dt} \approx n_e \sigma^{\text{ex}} \Delta x. \quad (5.1)$$

Here n_e ($= 3 \times 10^8$ electrons/cm³) is the electron density at a collector current of 3×10^{-3} A and a bombarding voltage of 10 V; the length Δx of the excitation region is 0.7 cm. Hence the excitation cross section (summed over all n) is

$$\sigma^{\text{ex}} = 1 \times 10^{-17} \text{ cm}^2, \quad (5.2)$$

which is in reasonable agreement with an estimate of σ^{ex} for helium excited by 100-eV electrons (S3). If the cross section for excitation of the n^{th} level is

$$\sigma(n) = \frac{\sigma^0}{n^3} g(n), \quad (5.3)$$

(Section 2.4), where $g(n)$ is a degeneracy factor, then the total excitation cross section can be obtained by summing over all n ,

$$\sigma^{\text{ex}} = \sum_n \sigma(n) \approx \int_{n_{\text{min}}}^{n_{\text{max}}} \frac{g(n)\sigma^0}{n^3} dn. \quad (5.4)$$

The assumption that mostly p states are excited leads to

$$\sigma^{\text{ex}} \approx \frac{3}{2} \frac{\sigma^0}{n_{\text{min}}}. \quad (5.5)$$

Since $n_{\min} \approx 16$ (Section 5.2), Equations 5.5 and 5.2 imply

$$\sigma^0 \approx \frac{2}{3} \sigma_{\min}^{\text{ex}} n_{\min}^2 = 2 \times 10^{-15} \text{ cm}^2, \quad (5.6)$$

which is in reasonably good agreement with typical ground-state atomic cross sections.

5.2 Time-of-Flight Spectra

A beam of Li atoms from the oven is excited by a perpendicular beam of electrons from a pulsed electron gun. The cathode is pulsed with a repetition rate of 870 Hz, a pulse width of 10 μ sec, and a pulse amplitude of 10 V. A transverse magnetic field of order 1.5 kG focuses the exciting electrons and removes ions and electrons from the atomic beam. Electron currents to the collector are typically 10^{-4} to 10^{-3} A during the pulse. Maintaining the oven, collector, grid, and aperture baffle plate next to the oven at ground potential shields the Rydberg-atom production region from stray electric fields.

Near the end of a 35-cm flight path, the excited Li beam passes through a pair of electric field plates and a second grounded aperture before entering the excited-atom detector. In the detector the HR atoms are field-ionized, and the ions are counted by a continuous-channel electron multiplier (Channeltron). The Channeltron cathode

is usually biased at 2250 volts. The electric field between this cathode and the detector target plate is nonuniform and ranges up to 10 kV/cm. This variation in the ionizing field is a result of having the Channeltron target plate slanted with respect to the Channeltron cone (Figure 7). The electric field is larger at points where the cone and the target plate are closer together. Thus, all HR states with $n \geq 16$ can be detected.

The resulting current pulses are converted to voltage pulses, which are amplified, shaped, and then catalogued according to excited-atom arrival time by a multi-channel scaler (MCS). The dwell time is 5.5 $\mu\text{sec}/\text{channel}$, and the scan reset pulse is derived from the cathode pulse. The result is that the MCS memory contains an excited-atom transit-time distribution.

Figure 12 shows a typical time-of-flight spectrum, together with the conditions under which it was obtained. The narrow peak occurring in the earlier channels is believed to be due to HR atoms produced by dissociative excitation of Li_2 molecules. This fast peak will be discussed further in Section 6.5. The broader thermal peak at the right of the spectrum is the major interest of this study.

5.3 Lifetime and Collision Measurements

Time-of-flight spectra were obtained with applied electric fields and introduced target gases, with a view to obtaining information

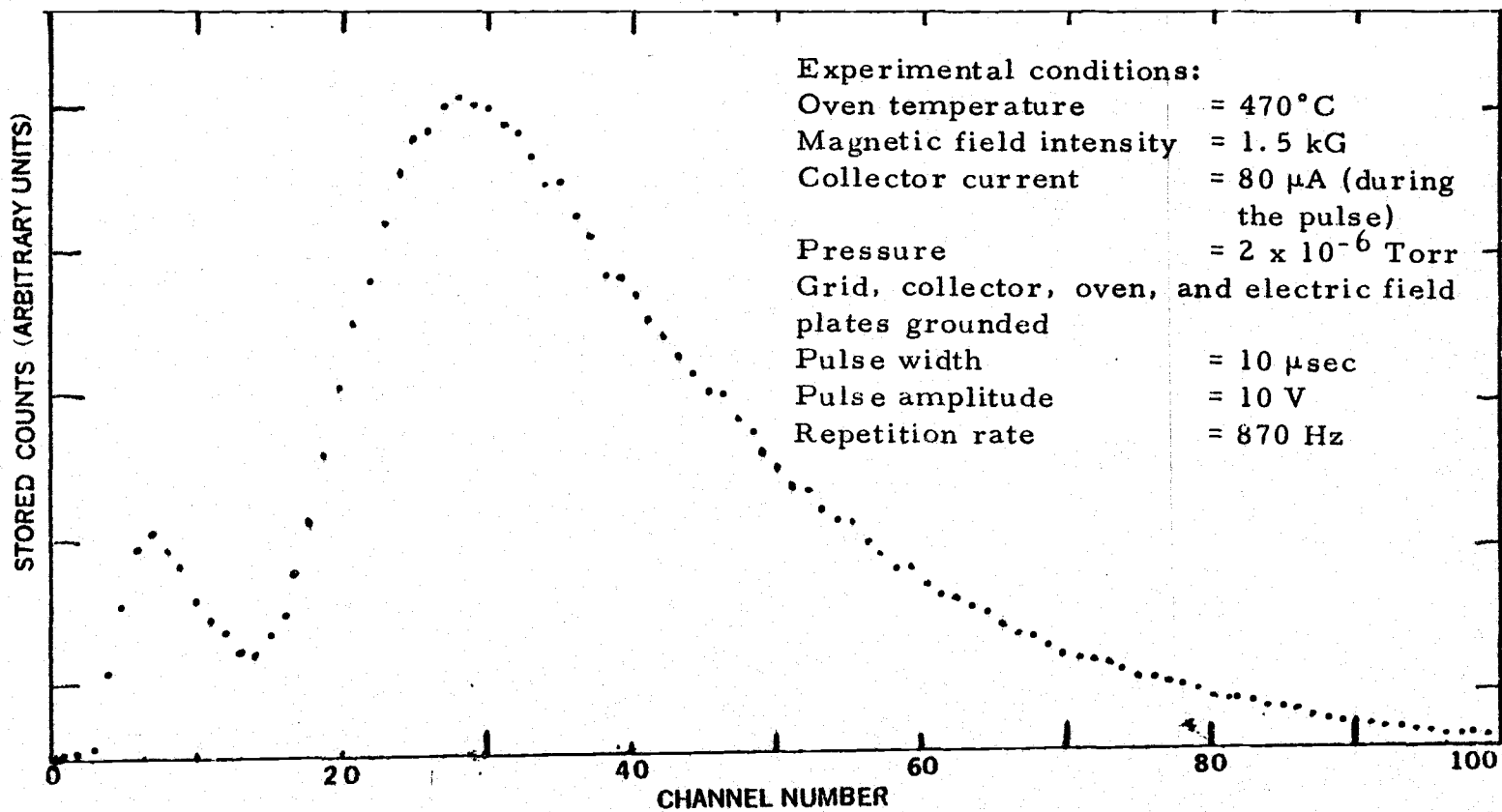


Figure 12. A typical time-of-flight spectrum obtained as a direct plot of the content of the analyzer memory channels. The fast peak to the left is discussed in the text; the broader peak to the right is due to high Rydberg lithium atoms.

concerning lifetimes and collision cross sections for HR lithium atoms. The special precautions taken during these measurements will now be described; the results obtained will be presented and discussed in Chapter 6.

During both lifetime and collision measurements a constant magnetic field, parallel to the electron beam and perpendicular to the atomic beam direction, was maintained over the circular portion of the experimental chamber (Section 4.1). The 1.5-kG magnetic field focuses the exciting electrons across the atomic beam and removes charged particles which are created in the excitation process. Electron currents to the collector increase by more than a factor 3 when the field is turned on. The field is measured by a commercial Hall probe, connected to a constant current supply. A digital millivoltmeter reads the magnetic field directly. The system is calibrated by an NMR gaussmeter, over a wide range of magnetic fields up to 10 kG. Pressure measurements with the ionization gauge were made with the magnetic field turned off. The motion of ions in the gauge is affected by the magnetic field, resulting in slightly different gauge readings with and without the field.

Normalization of TOF spectra is accomplished by conversion of the stored counts from each analyzer memory channel to a counting rate. Care is therefore taken to record the time of day, together with the ratemeter reading (Section 4.7), at the beginning and the end

of acquisition of each TOF spectrum. The time-of-day information is used to correct the number of multi-channel-scaling repeats (i. e. , the number of times the analyzer memory channels are swept through, which is stored in channel zero), in case of an overflow. (Each memory channel stores a maximum of six digits, losing the most significant digit in case of an overflow.) This provides an accurate record of the spectrum acquisition time. The ratemeter measurements give counting rates integrated over all channels, which are used to indicate long term drifts in the systems; beginning and end counting rates which differ by no more than 5% are acceptable.

At the highest electric fields and target gas pressures, the overall counting rates become very small (less than 10 counts/sec). Improved statistics (signal-to-noise ratios) are obtained for such spectra if they are recorded over a long period. Thus, for the TOF spectrum obtained at 5.0 kV/cm (which will be discussed in Section 6.1), over 8 hours of recording time were employed. Similarly, spectra obtained at 1.0 kV/cm and at the highest target gas pressures (Section 6.2) were recorded for at least 4 hours.

6. RESULTS, ANALYSIS AND INTERPRETATION

Two kinds of measurements will be presented and discussed in this section. Time-of-flight measurements at various electric fields will be described and then discussed with a view to obtaining information concerning lifetimes of HR lithium atoms. Collision measurements will then be considered, from which cross sections for interactions of HR atoms with various targets will be extracted and compared with theoretical calculations. The predictions of the HR collision model presented in Section 3.4 will also be compared with experiment in order to understand the shapes of the observed TOF spectra. Finally, a summary of the conclusions made in this study, as well as proposals for further study, will be presented.

6.1 Lifetime Measurements

For lifetime measurements TOF spectra were obtained at electric fields equal to 0.0, 0.5, 0.7, 1.6, 2.8 and 5.0 kV/cm. Figure 13 shows the observed spectra obtained at 0 and 2.8 kV/cm, together with the theoretical transit-time distribution for a non-decaying thermal beam, which was derived in Section 3.1 (Equation 3.4).

Higher electric fields were not used because of low signal and high background rates obtained at applied fields in excess of 5 kV/cm.

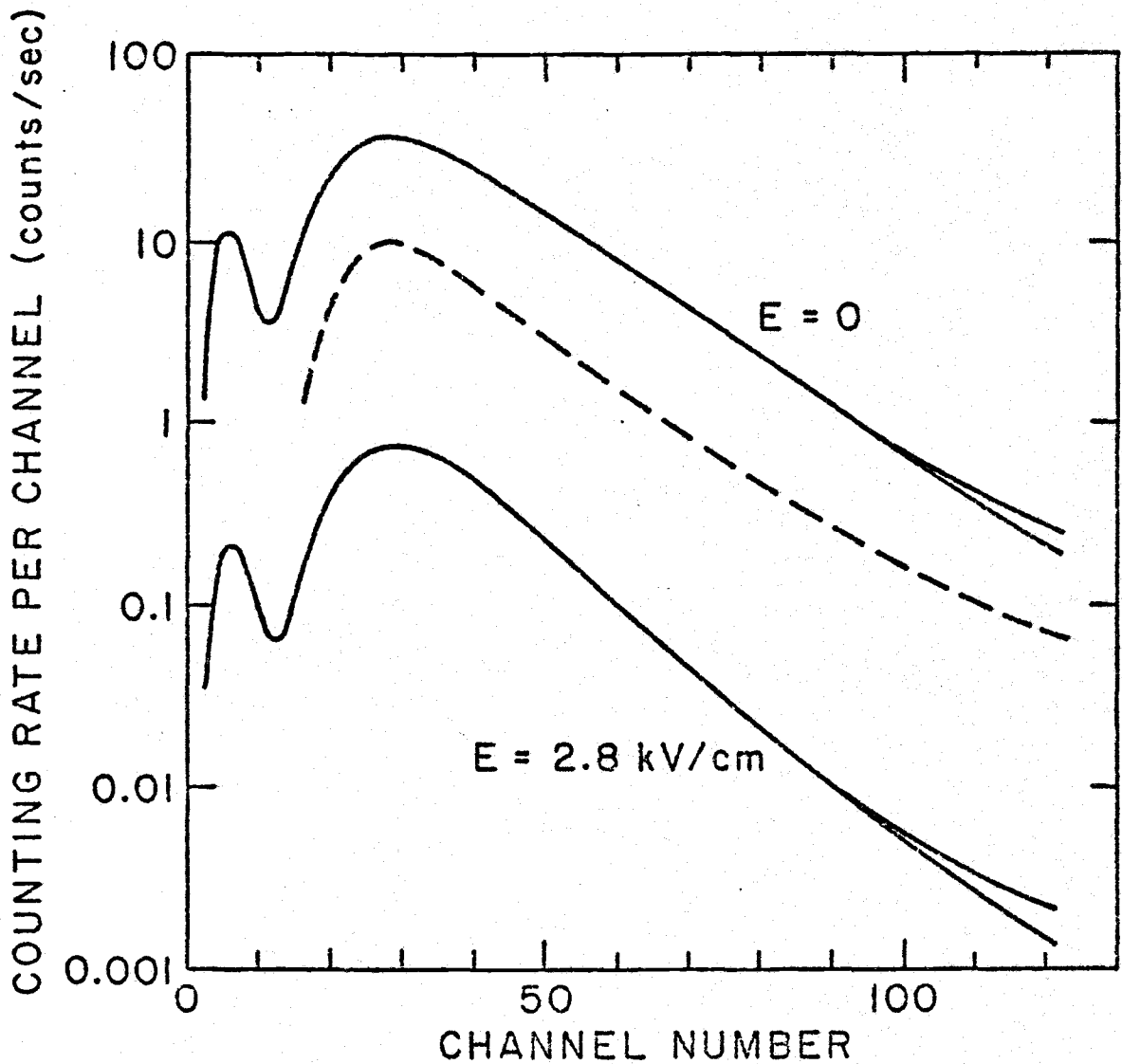


Figure 13. Observed time-of-flight spectra for electric fields $F = 0$ and 2.8 kV/cm . Observation times were 15 min and 8 hr, respectively. The dashed line is a theoretical transit-time distribution for a non-decaying thermal beam. The double lines indicate the scatter in the data.

Also, when high field measurements were attempted (7 kV/cm), large distorted pulses were observed at the output of the Channeltron. These pulses are probably due to corona discharge between the electric field plates, as they disappeared promptly when lower fields were applied. The experimental curves, shown in Figure 13, have shapes which are very similar to those of the theoretical distribution, indicating that the HR lithium atoms do not decay appreciably in flight.

The displayed spectra and those measured at other electric fields were obtained at a base pressure of 2×10^{-6} Torr and a magnetic field of 1.5 kG at the excitation region. A zero-field spectrum was obtained at the beginning and the end of the run and between nonzero-field spectra. In this way drifts in the apparatus could be detected and corrected for, as will be explained shortly.

The stored counts in the analyzer memory channels are printed out and punched onto paper tape by an ASR-33 Teletype. The punched data can be read directly into storage files in the memory of the Control Data 3300 computer operated by Oregon State University. Analysis of the stored data is accomplished by means of simple Fortran IV codes, which perform such tasks as background subtraction, normalization of spectra, integration of a spectrum over a specific number of channels, addition of one spectrum to another, and division of one spectrum by another. For example, the experimental

curves displayed in Figure 13 are obtained from the observed spectra by means of the following steps.

- 1) A fixed background is subtracted from the number of counts stored in each analyzer channel. The background is usually obtained by averaging the counts stored in the highest channels. Inspection of the printed data usually indicates clearly where the spectrum ends and the noise begins.
- 2) The spectrum is normalized by dividing each of the stored counts, corrected for background, by the spectrum acquisition time (obtained as described in Section 5.3).
- 3) Finally, the logarithms of the normalized counting rates so obtained are calculated and plotted.

The TOF spectra in Figure 13 as well as those obtained at the other electric fields show an overall reduction in counting rate as the electric field is increased. The fractional reduction in probability—the survival probability for an excited atom passing through an electric field, $R_F(t)$ —is the ratio of the normalized counting rate for an analyzer channel with an applied electric field to that for the same channel, but without the electric field. Since the transit-time distributions with and without the electric field are similar in shape, the survival probability may be calculated as a ratio of the total count rates, integrated over all analyzer channels. These survival probabilities are plotted in Figure 14 for electric fields up to 5.0 kV/cm. This

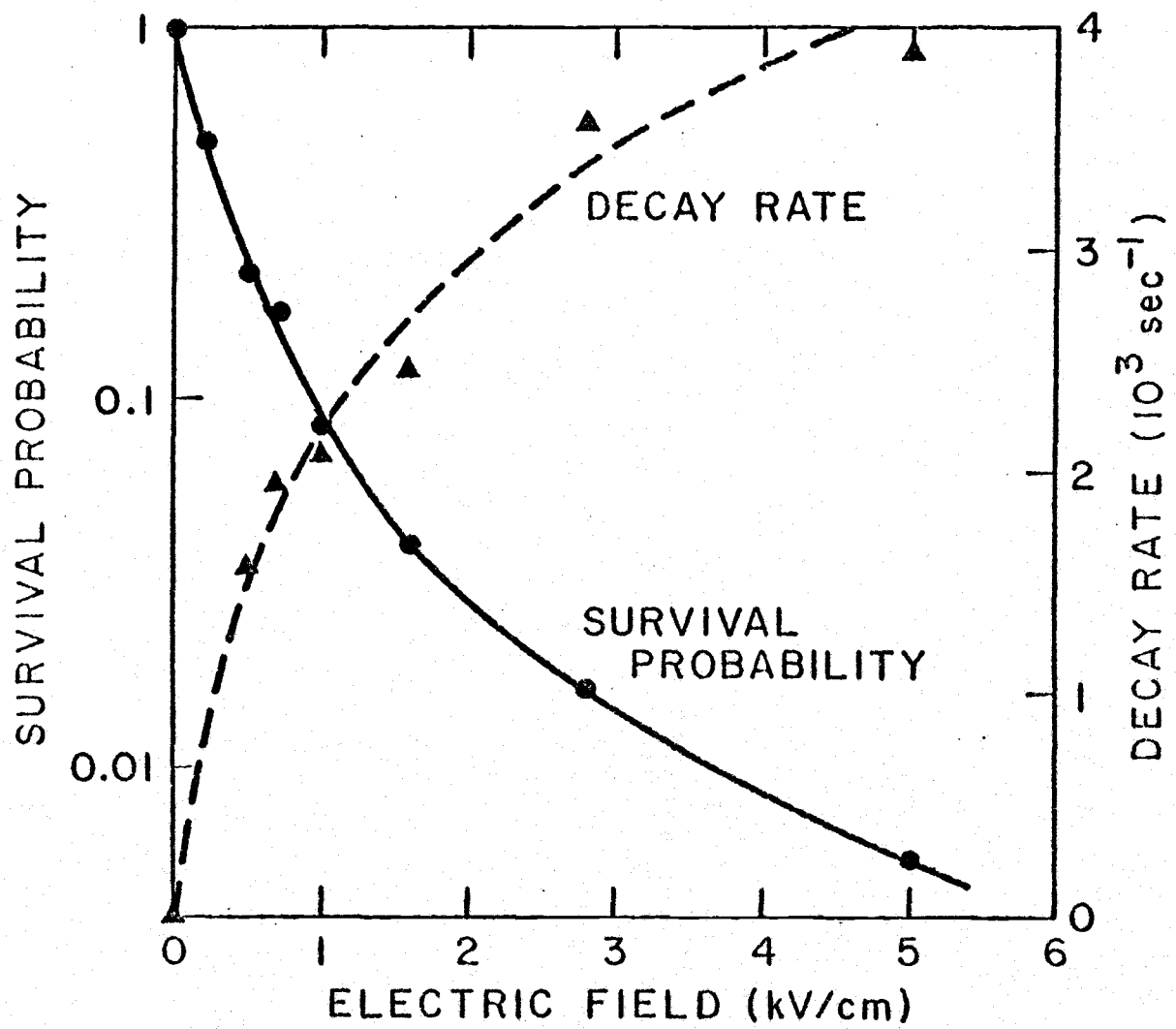


Figure 14. Survival probability (solid line) and radiative decay rates (dashed line) for high Rydberg lithium atoms as functions of applied electric field.

figure shows that a major portion of the HR signal ($> 90\%$) is removed by an electric field $F = 1.0 \text{ kV/cm}$, for which the critical quantum number is $n_c = 28$, as can be seen from Equation 2.7. Thus, most of the HR atoms detected at zero field are in principal quantum states $n > 30$. Since low- n states tend to decay in flight more rapidly than higher- n states, it is expected that at a given electric field F , the detected states are mainly those with n equal to or just below n_c . Figure 14 provides experimental support for this phenomenon, since the data show that for an increase in the electric field from 1.0 to 2.0 kV/cm the cutoff quantum number of the states observed changes from 28 to 24, while a further 75% reduction in signal occurs. This is an important result, because it indicates that any decay rates measured for the spectrum obtained at the electric field F can, to a good approximation, be associated with decay of HR states with principal quantum number $n_c [(F_0/F)^{1/4}]$.

A closer look at Figure 13 shows that at large transit time t (between channels 40 and 80) the experimental TOF distributions have nearly straight portions with negative slopes which increase in magnitude with increasing electric field. The applied electric field ionizes all HR states with $n \geq n_c$, leaving a HR signal with a larger fraction of lower- n states, which can decay radiatively more readily than higher- n states (as discussed in Section 2.3). The slowest atoms spend the most time in transit, hence the fractional loss of signal is

larger at the higher channels.

For each electric field the normalized counting rate, calculated as described at the beginning of this section, is divided by the normalized zero-field counting rate, obtained for the same analyzer channel. The logarithm of this channel-by-channel ratio, $\ln R_F(t)$, which displays the nearly constant slope characteristic of an in-flight decay process, is shown in Figure 15 for the 2.8 kV/cm data shown in Figure 13. The lower portion of this curve (channel 20 and below) is modified by the presence of the fast peak. This lower portion is therefore not shown in Figure 15. Similar plots were obtained for the spectra acquired at other electric fields. The slopes of the channel-by-channel ratios are also plotted in Figure 14 as functions of the applied electric field.

If the beam consisted of HR atoms in predominantly s, p, and d states, the experimental slopes measured above would represent radiative decay rates. These low- ℓ states are expected to be populated in direct electron impact excitation (Section 2.5). The radiative decay rates for s, p and d states of lithium with large values of n , obtained by extrapolation of tabulated low- n transition rates, are shown in Figure 4 (page 22). Also shown in Figure 4 are the slopes observed for the channel-by-channel ratios, together with the rates for circular orbit states. It is evident from Figure 4 that the observed slopes are at least a factor of 10 smaller than the low- ℓ

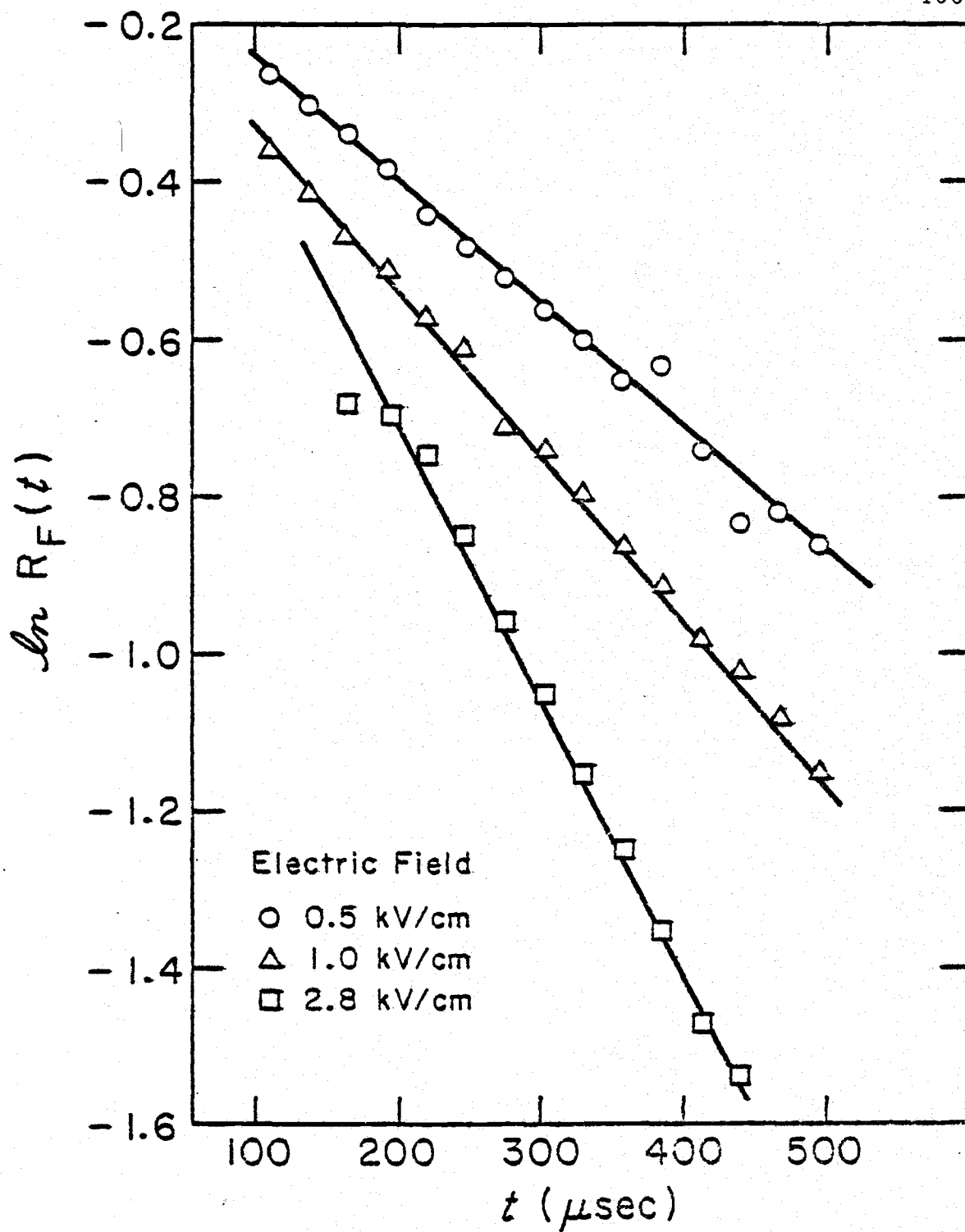


Figure 15. Logarithm of channel-by-channel ratios for the 2.8 kV/cm spectrum shown in Figure 13, together with those for the 0.5- and 1.0-kV/cm spectra.

rates and are in closer agreement with the high- ℓ rates. These observations imply the presence of high- ℓ states in the excited lithium beam.

For a fixed low- ℓ value at high n , the radiative decay rate of the n^{th} state in hydrogen is approximately proportional to n^{-3} .

However, if all the ℓ -substates at a given n are occupied, the statistical-average decay rate would be

$$\Gamma_n = \left[\sum_{\ell} \frac{2\ell+1}{n^2} \Gamma_{n\ell} \right] \propto n^{-4.5} \quad (6.1)$$

(see Section 2.3). Similar n -dependences hold for HR states of atoms other than hydrogen. If the experimental slopes represented radiative decay rates, they would be expected to be proportional to $n_c^{-\alpha}$, with $3 \leq \alpha \leq 4.5$, for an arbitrary ℓ -distribution. The α observed from Figure 17 is 1.7 ± 0.4 . That the observed α is not within the range 3 and 4.5 can be explained in terms of cascade effects.

Qualitatively, the experimental slope of $\ln R_F(t)$ represents only those decays which effectively remove the HR atoms from the beam. HR states with high n - and high ℓ -values do not decay directly to the ground state because of the $\Delta\ell = \pm 1$ selection rule. Rather, transitions are made to other HR levels, usually to the maximum- ℓ sublevel of the principal quantum state for which $\Delta n = -1$ and the

transition energy is a maximum. (The transition rate is proportional to the cube of the transition energy; see Section 2.3.) From the latter level, radiative decay proceeds only via $\Delta n = -1$ and $\Delta l = -1$ changes through successive circular orbit states, which have much lower transition rates than s, p and d states. The resulting states may still be detected and so do not contribute to the measured slopes. A mathematical model based on sequential cascade has been developed in our laboratory (Kocher, K9). This model uses the experimentally observed dependences of $R_F(t)$ and its slope on the electric field F , together with the assumption that the initial HR population P is proportional to $1/n^3$ (Section 2.5), to get $\alpha \approx 5.7$. This is seen to be consistent with $\alpha = 5$ for circular orbit states (Equation 2.9).

A possible mechanism for the electron impact excitation of high- l states has been proposed by Fano (Section 2.5). In the Fano process, which requires that the excitation energy be within a fraction of 1 eV of threshold, the incident and excited electrons become closely correlated, exchanging angular momentum as they move slowly away from the core-ion. In the present experiment, high- l states were observed at threshold energies but also at excitation energies having several times the threshold value; the shapes of the transit-time distributions were not affected by large changes in the amplitude of the cathode pulse. The shapes of the TOF spectra were

also not affected by large changes in the magnetic field. Thus, spectra obtained with and without a magnetic field of 1.5 kG have similar shapes. (When the magnet is turned off, the electron current to the collector is reduced and longer acquisition times are then necessary.) It may therefore be concluded that ℓ -mixing due to the quadratic Zeeman interaction—the A^2 term in the Hamiltonian which represents the interaction between a radiation field, described by a vector potential A , and matter—is not the source of high- ℓ states in the present beam. Schiavone et al. (S3) have speculated that ℓ -increases can arise from multiple electron collisions within the source during electron impact excitation. Thus, a HR atom excited to a low- ℓ state near the beginning of the excitation region can have its ℓ -value increased in one of more further encounters with electrons. If this were the dominant or only mechanism for high- ℓ excitation in the present experiment, the shapes of the transit-time distributions would depend very strongly on the electron current. Thus, for an n -electron process for example, the measured slopes would be expected to be proportional to the n^{th} power of the electron density. The observations of the present experiment do not verify this expectation. Even with a several hundred-fold reduction in the cathode current, so that the electron density is maintained well below $10^7/\text{cm}^3$, the shapes of the observed transit-time distributions are similar to that of the theoretical non-decaying beam. It is therefore

concluded that in the present experiment multiple electron collisions do not contribute significantly to the production of high- ℓ states.

Collisions between HR and neutral atoms can result in a change in ℓ (G5, G6). That this process can account for the high- ℓ production observed in this study is shown in the next section, where results of collision measurements are discussed.

6.2 Determination of Collision Cross Sections

In collision measurements the noble gases He, Ne and Ar, as well as molecular gases H_2 , N_2 and NH_3 were used as targets. Time-of-flight spectra were obtained at various target gas pressures up to 4×10^{-4} Torr and at electric fields of 0.0, 0.2 and 1.0 kV/cm (except for NH_3 , which was only studied at zero field). Figure 16 shows the TOF spectra obtained at the base pressure of 2×10^{-6} Torr, together with results obtained for a neon target gas at several partial pressures p . The measurements were made at an applied electric field of 0.2 kV/cm. The TOF spectra become narrower as the target gas pressure is increased. The narrowing is due to the removal of slower atoms (i. e., those with longer transit times) from the beam. Similar TOF spectra were recorded for each of the other target gases and at each of the electric fields used. The TOF spectra recorded at 1.0 kV/cm and the highest target gas pressures required the longest acquisition times (at least 4 hours), as was discussed in Section 5.3.

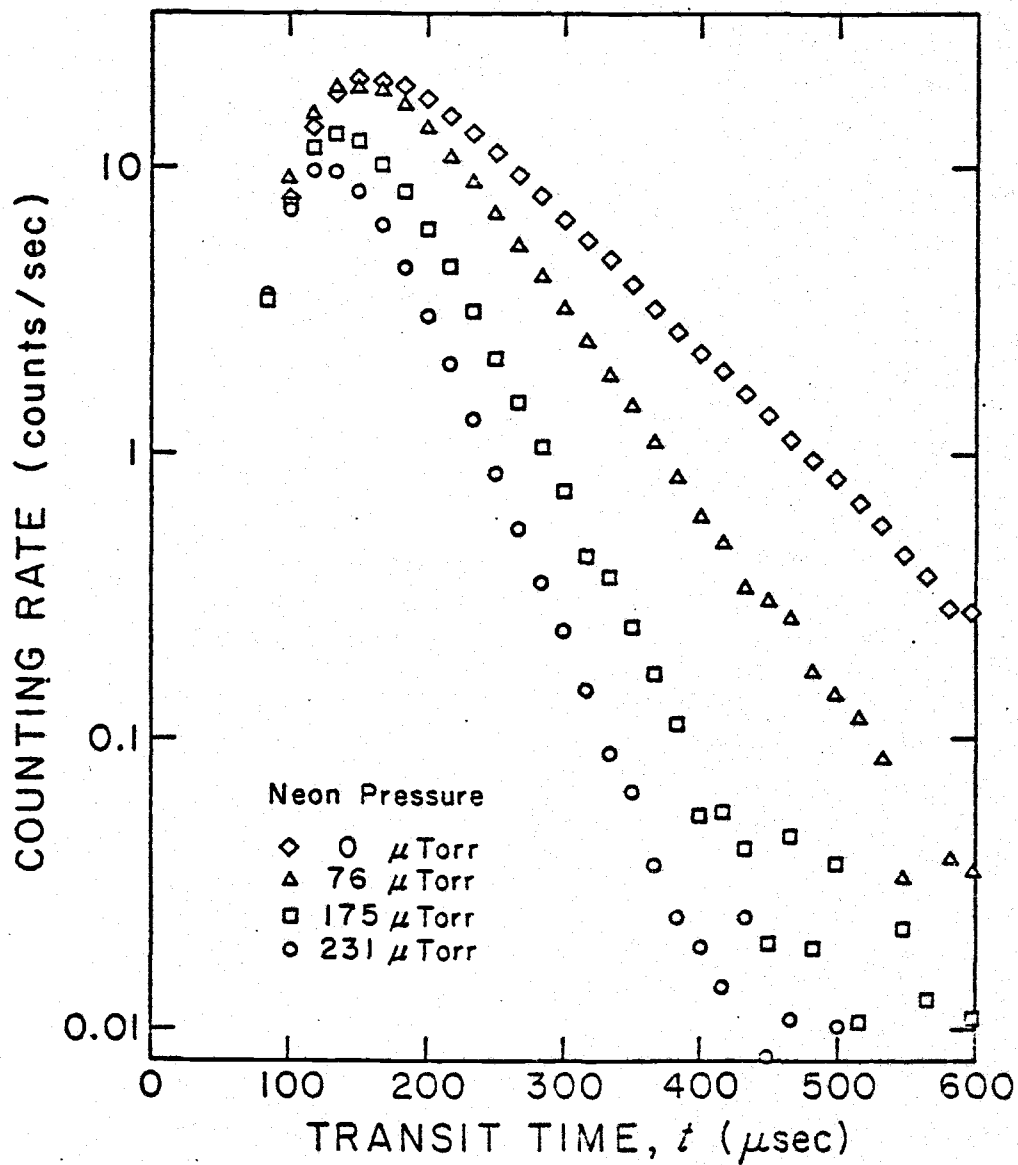


Figure 16. Normalized time-of-flight spectra with neon as target gas and an applied electric field of 0.2 kV/cm. Each point represents the counting rate averaged over three channels.

The excitation pulse amplitude was maintained at 10 V throughout these measurements. The exciting electrons therefore had energies well above the threshold for excitation of HR states in lithium; however, these energies were below the ionization limits for the target gases. Use of low cathode voltages avoids contributions to the HR signal from target gas excitation. That there was no such interference was verified in the following way: the oven was maintained at a temperature well below that at which a lithium beam can be formed, while the electron gun was operated normally and target gas was present in the chamber. No HR signal was detected under these conditions, indicating that there is probably no target gas excitation. Monitoring the collector current also revealed no reduction as target gas was admitted, indicating that at the pressures used the presence of the target gas does not affect the operation of the cathode. The Channeltron pulse height distribution was also monitored continuously and found to be negligibly affected by the target gas, even at the highest pressures used, implying that the Channeltron characteristics are not significantly changed during high pressure operation.

For each target gas species and each electric field, a channel by channel ratio $R_p(t)$ was computed, in which the counting rate with the target gas present was divided by the rate recorded in the same analyzer channel without the gas. The neon ratios at electric

fields 0.0, 0.2 and 1.0 kV/cm and the 0.2-kV/cm ratios for the target gases He, Ar, H₂, and N₂ are displayed in Figures 17 through 23. The zero-field data for NH₃ are shown in Figure 24. The channel-by-channel ratios were obtained by a computer program (Sections 5.3, 6.1).

On semi-log plots, each ratio $R_p(t)$ shows a nearly straight portion at large flight times t and a curved portion at small t . For the purpose of this analysis, these experimental ratios can be represented by

$$R_p(t) = F(t)e^{-\gamma t}, \quad (6.2)$$

so that

$$\ln R_p(t) = \ln F(t) - \gamma t. \quad (6.3)$$

Here $\ln F(t)$ is a factor which describes the curvature of $\ln R_p(t)$ at small flight times but is nearly constant at large t . The two terms on the right side of Equation 6.3 will be analyzed separately, starting with the linear term.

Since $\ln F(t)$ is nearly constant at large t , γ can be identified with the magnitude of the slope of the straight portion of $\ln R_p(t)$, as in Figures 25 to 29, where γ is plotted as functions of the target gas density. For each target gas species the plotted points lie on an approximately straight line. The slopes of

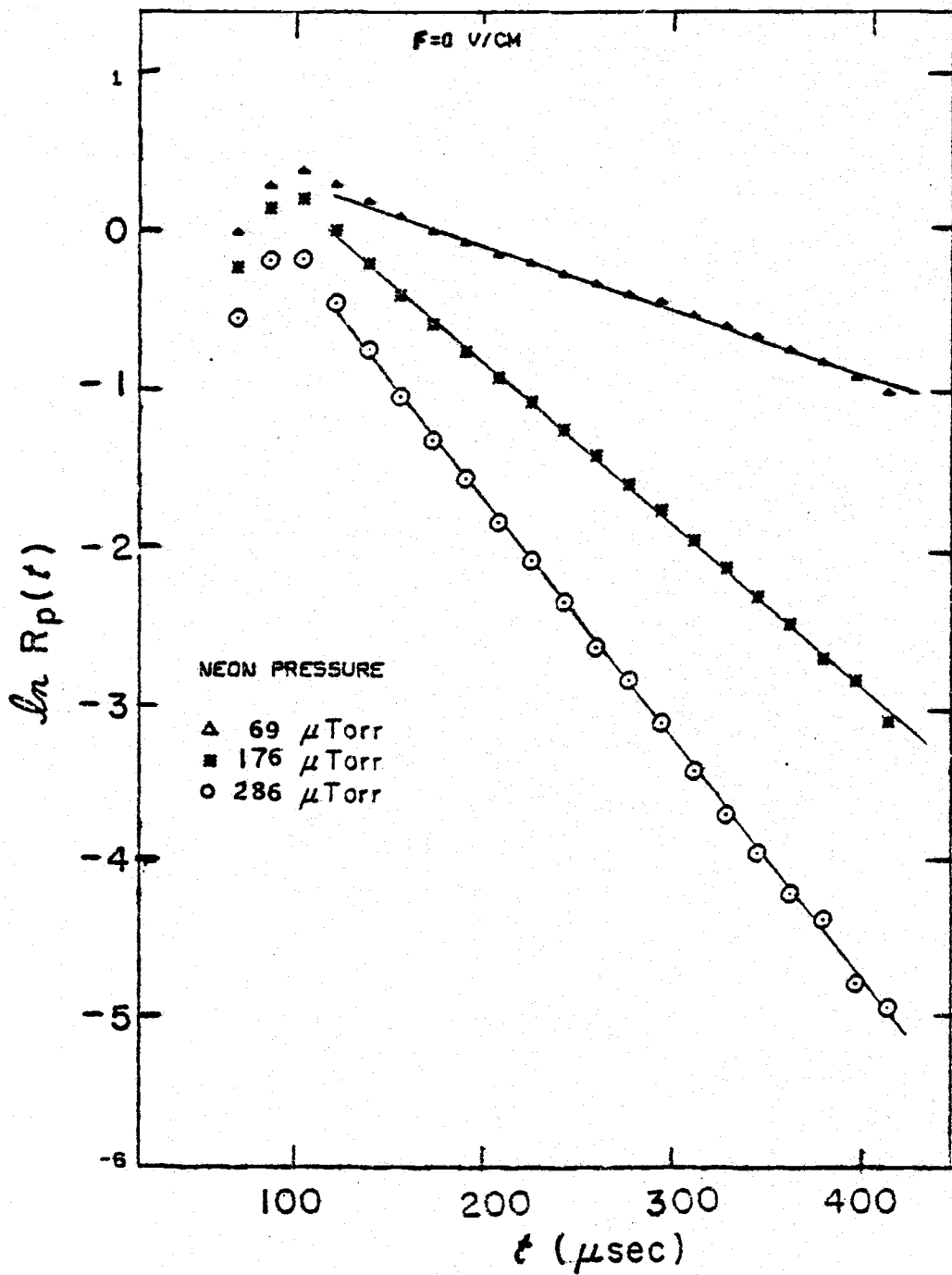


Figure 17. Logarithm of channel-by-channel ratios $R_p(t)$ for neon with no applied electric field.

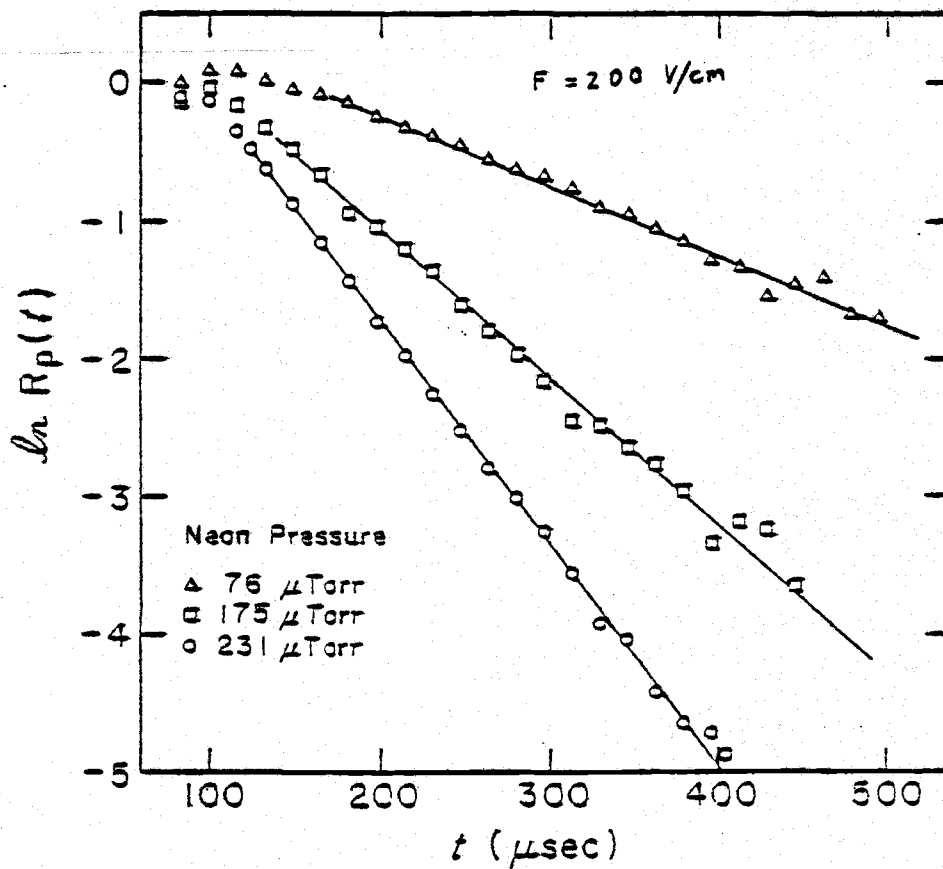


Figure 18. Logarithm of channel-by-channel ratios $R_p(t)$ for neon with applied electric field $F = 0.2 \text{ kV/cm}$.

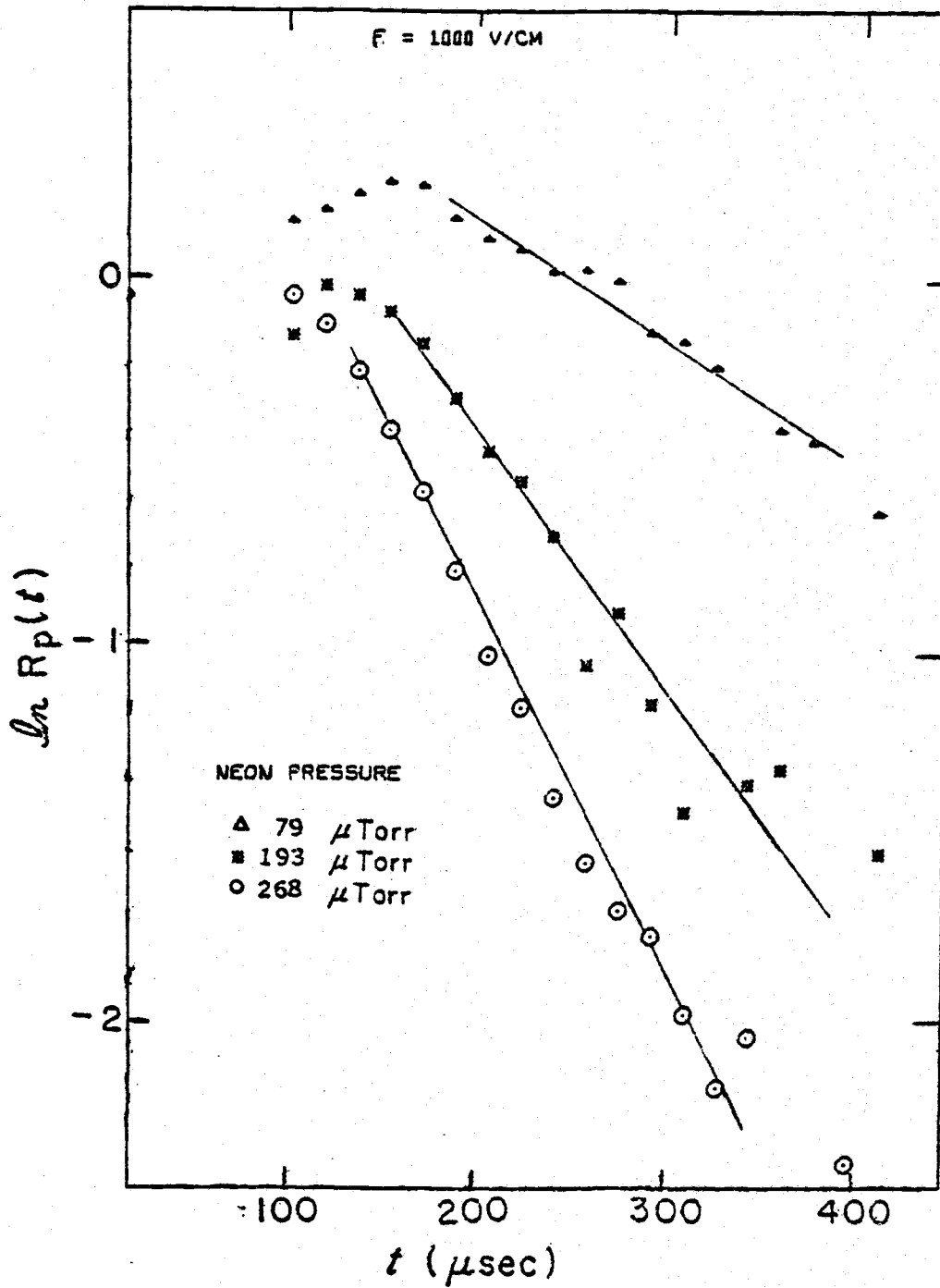


Figure 19. Logarithm of channel-by-channel ratios $R_p(t)$ for neon with applied electric field $F = 1.0 \text{ kV/cm}$.

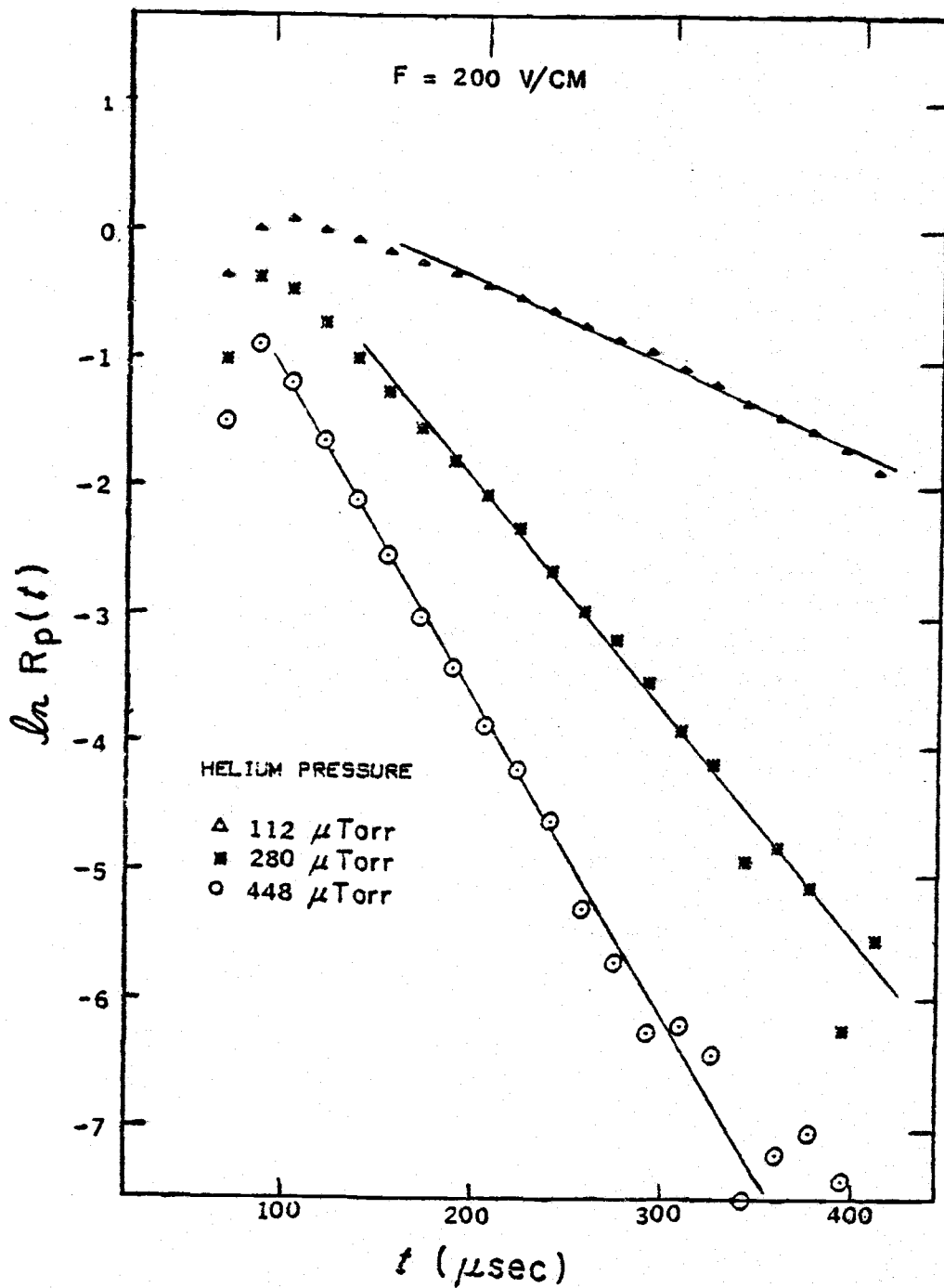


Figure 20. Logarithm of channel-by-channel ratios $R_p(t)$ for helium with applied electric field $F = 0.2 \text{ kV/cm}$.^P

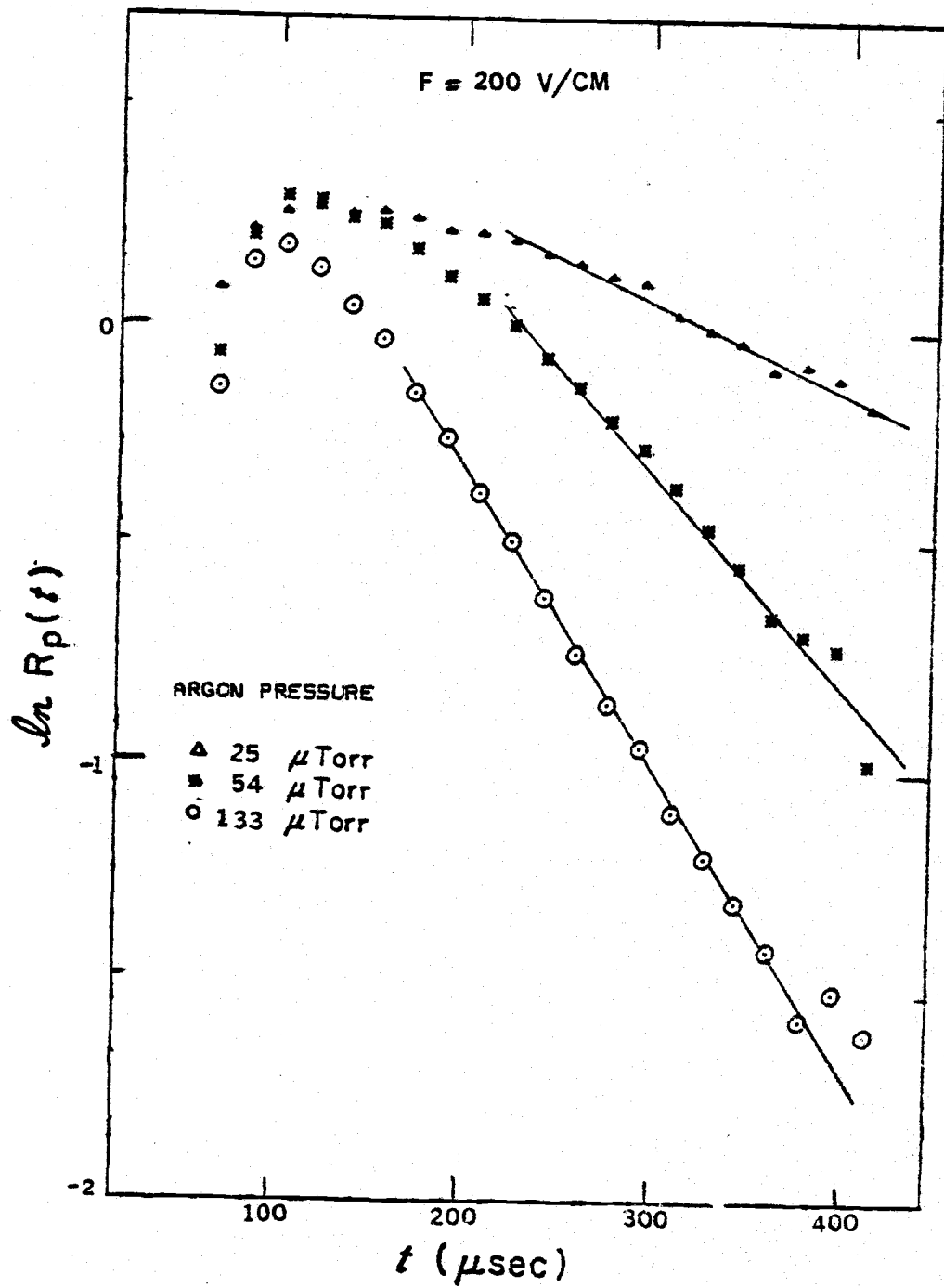


Figure 21. Logarithm of channel-by-channel ratios $R_p(t)$ for argon with applied electric field $F = 0.2 \text{ kV/cm}$.^P

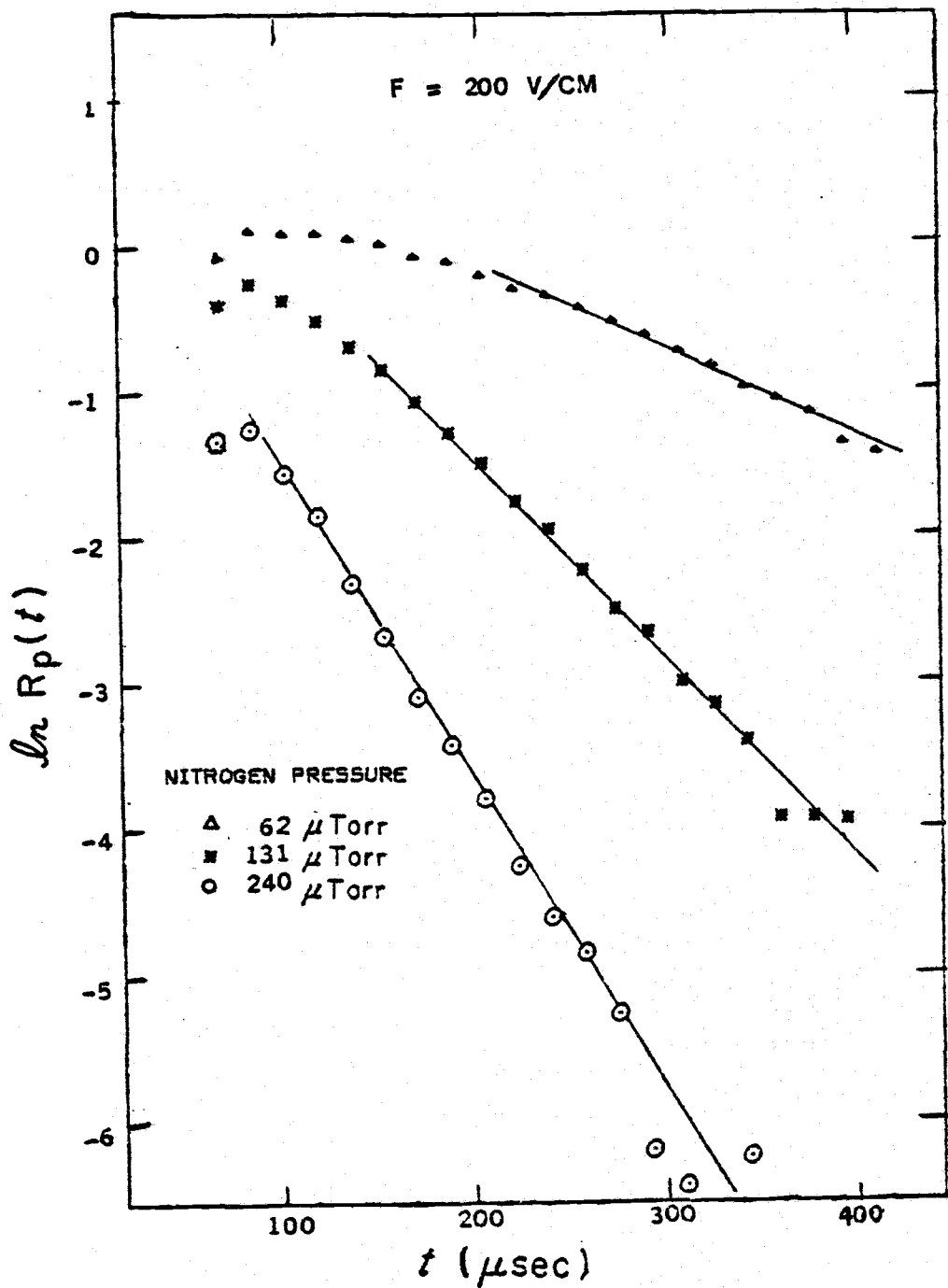


Figure 22. Logarithm of channel-by-channel ratios $R_p(t)$ for nitrogen with applied electric field $F = 0.2 \text{ kV/cm}$.

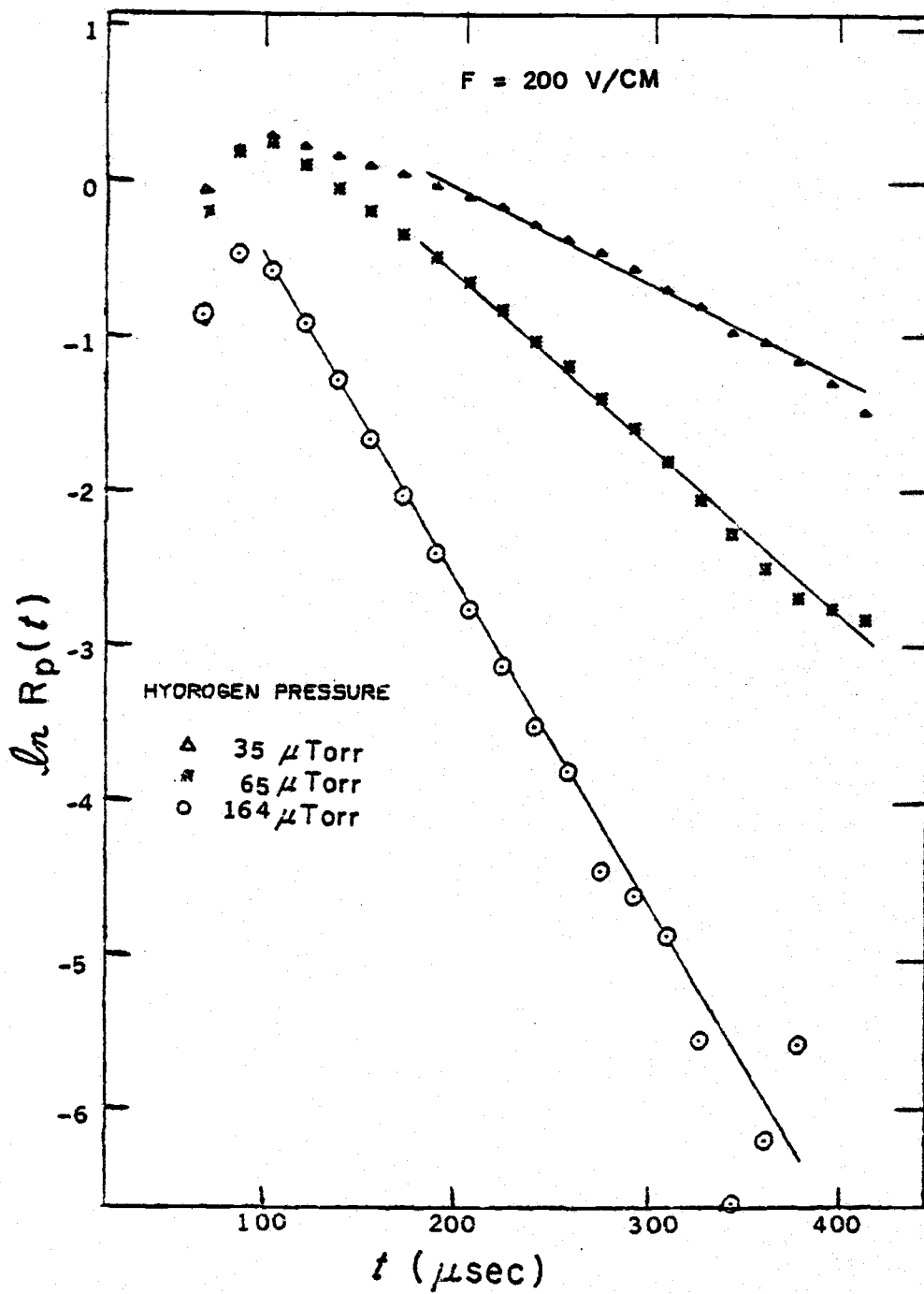


Figure 23. Logarithm of channel-by-channel ratios $R_p(t)$ for hydrogen with applied electric field $F = 0.2 \text{ kV/cm}$.

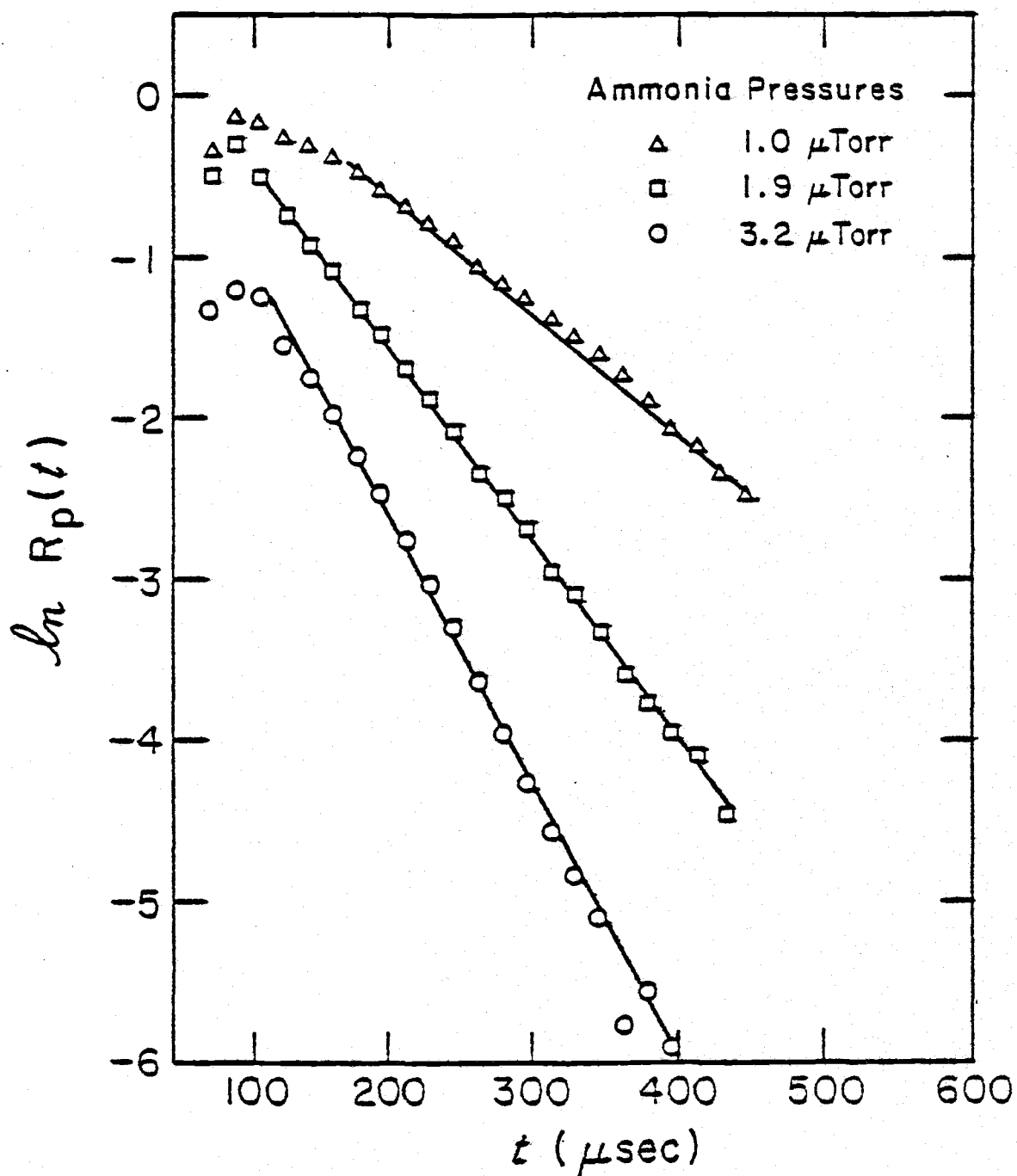


Figure 24. Logarithm of channel-by-channel ratios $R_p(t)$ for ammonia with no applied electric field.

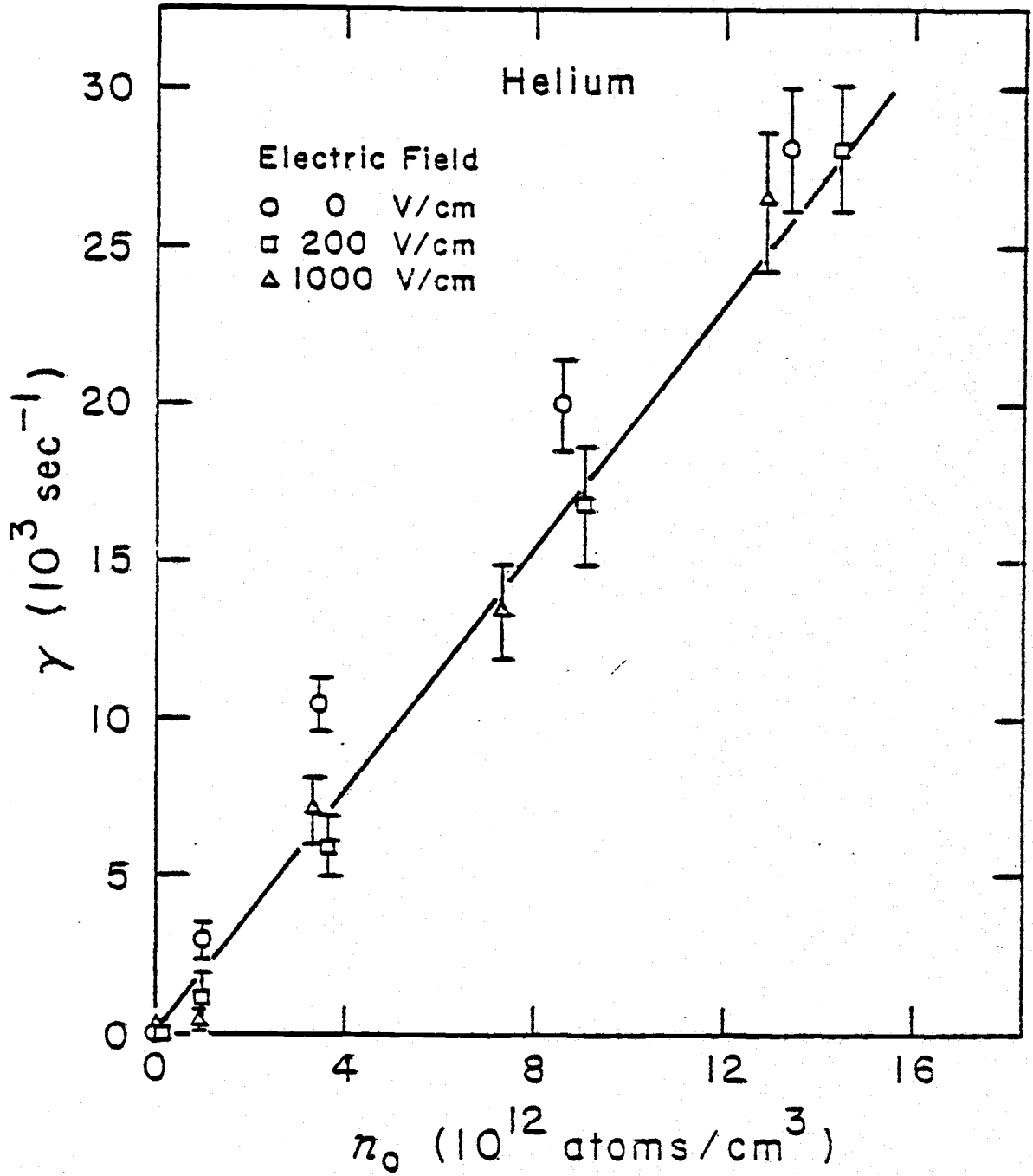


Figure 25. Slopes γ of \ln [channel-by-channel ratios] for helium, as a function of target gas density n_0 .

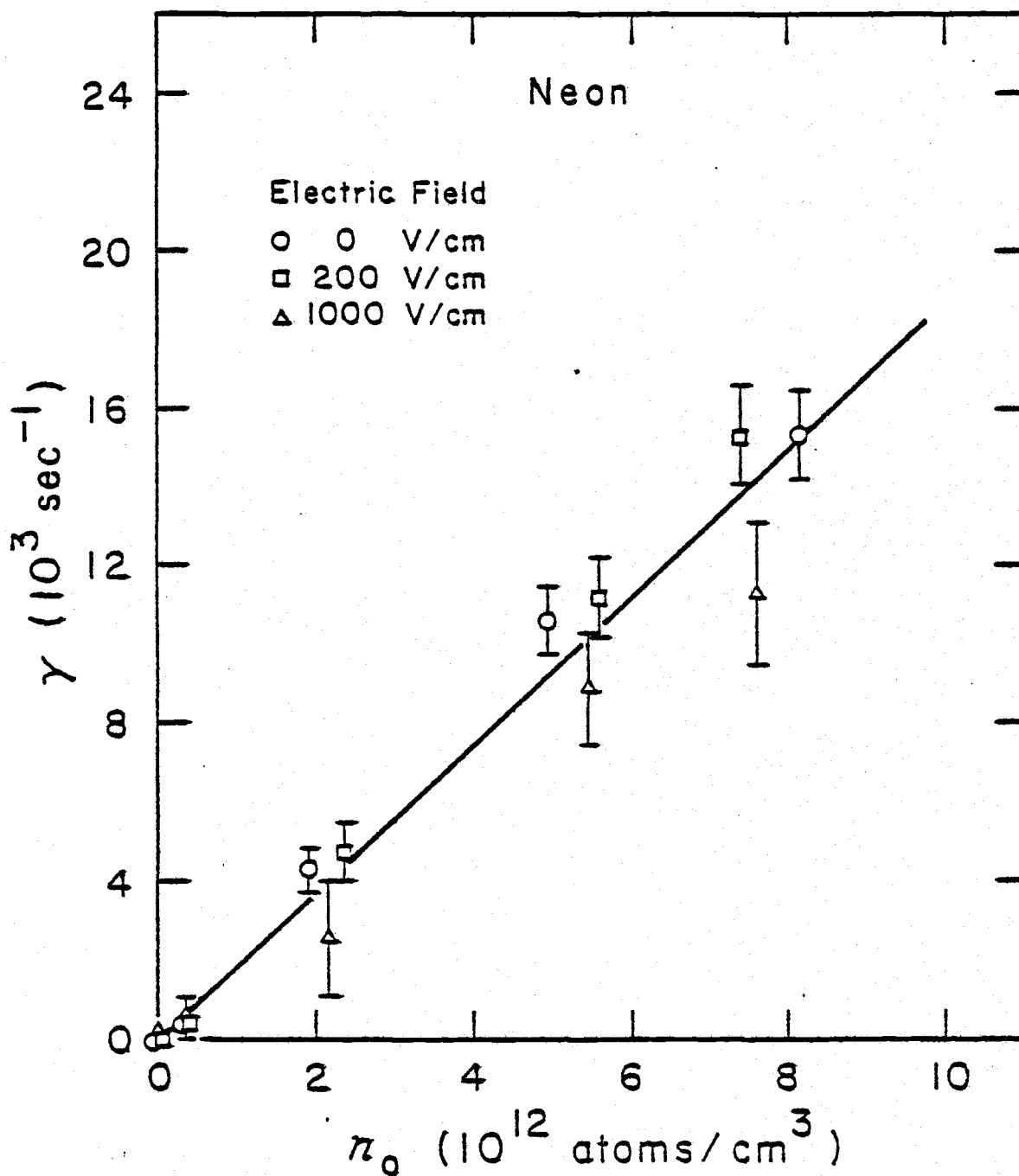


Figure 26. Slopes γ of \ln [channel-by-channel ratios] for neon as a function of target gas density n_0 .

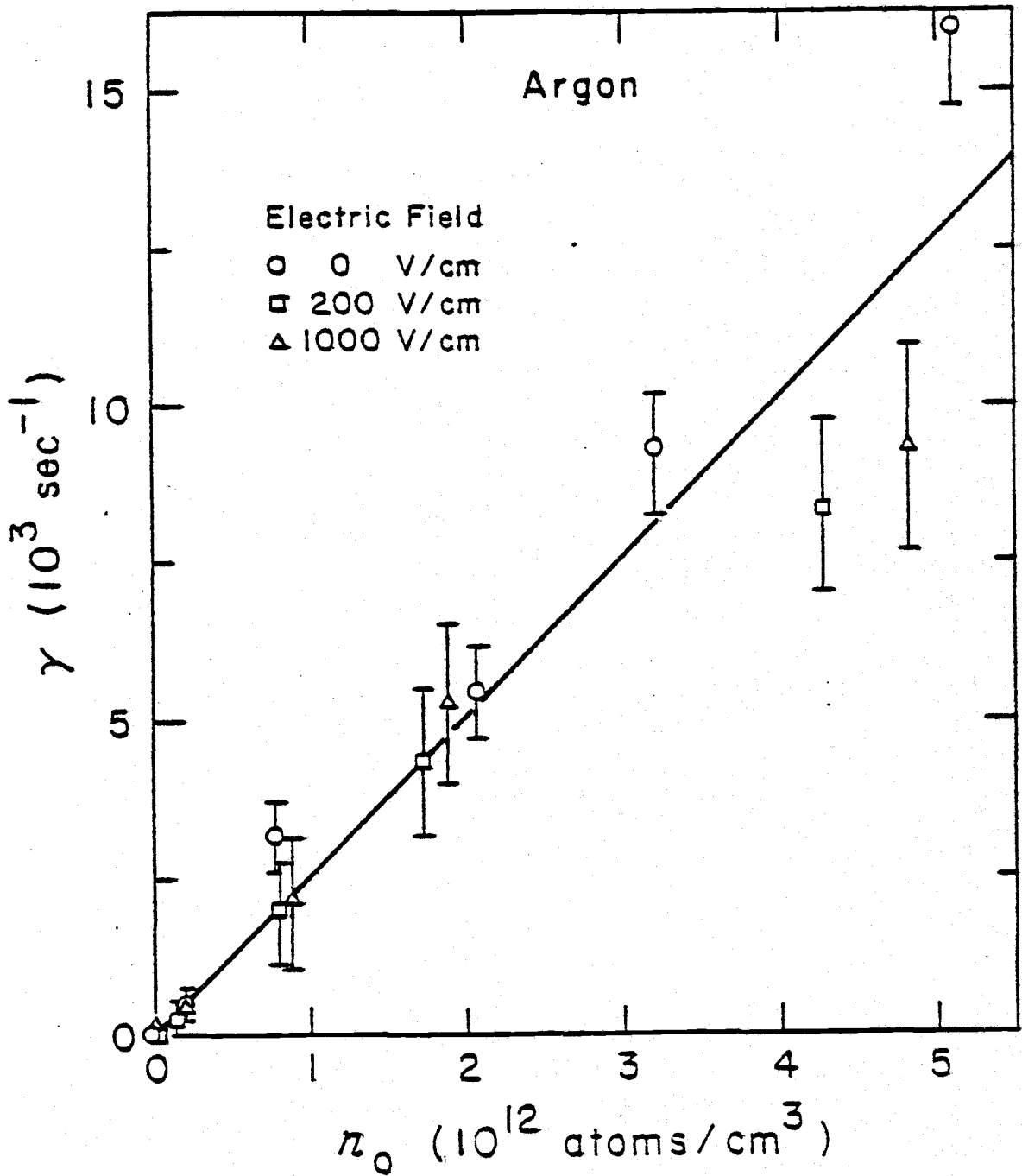


Figure 27. Slopes γ of \ln [channel-by-channel ratios] for argon as a function of target gas density n_0 .

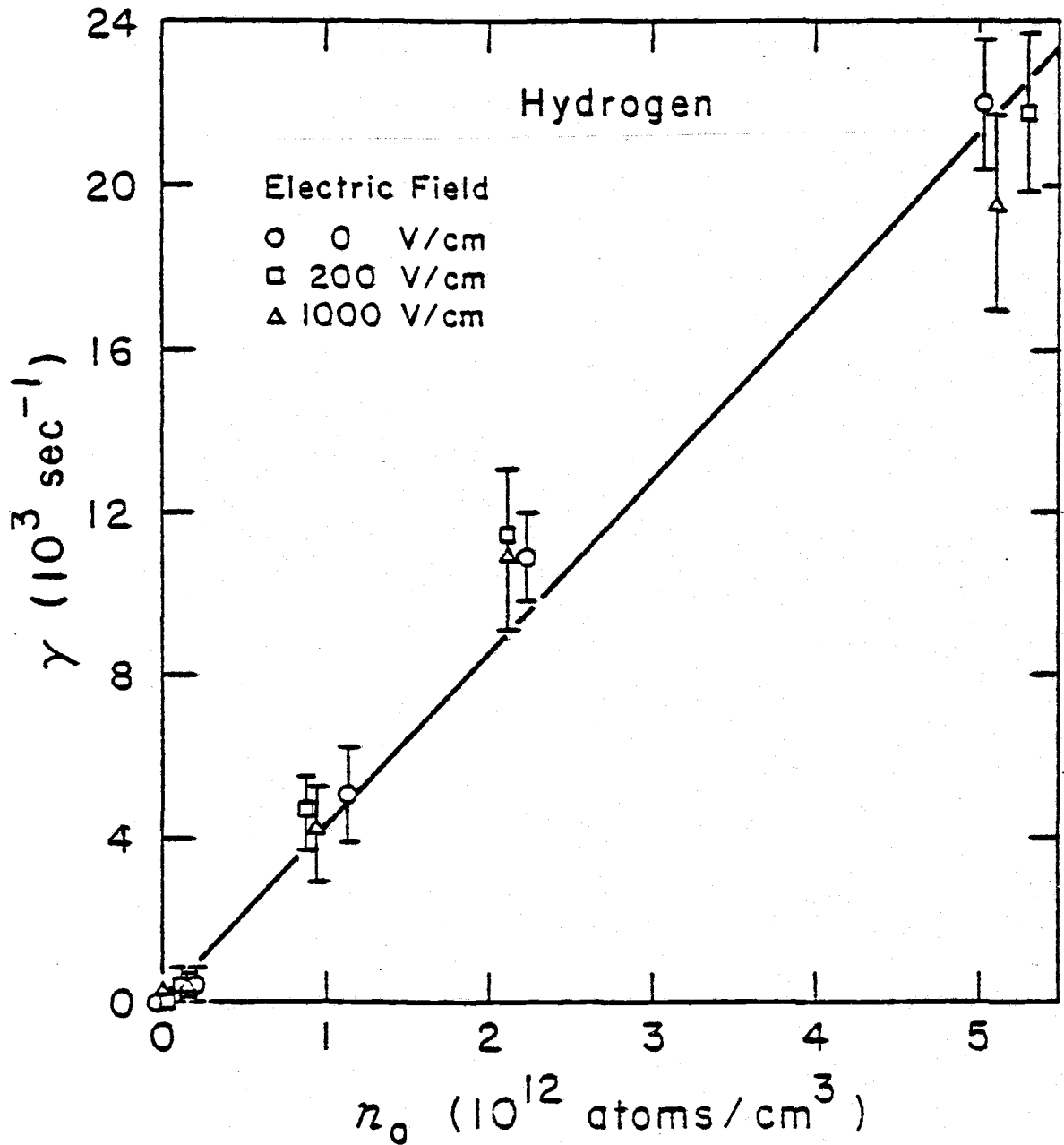


Figure 28. Slopes γ of \ln [channel-by-channel ratios] for hydrogen as a function of target gas density n_0 .

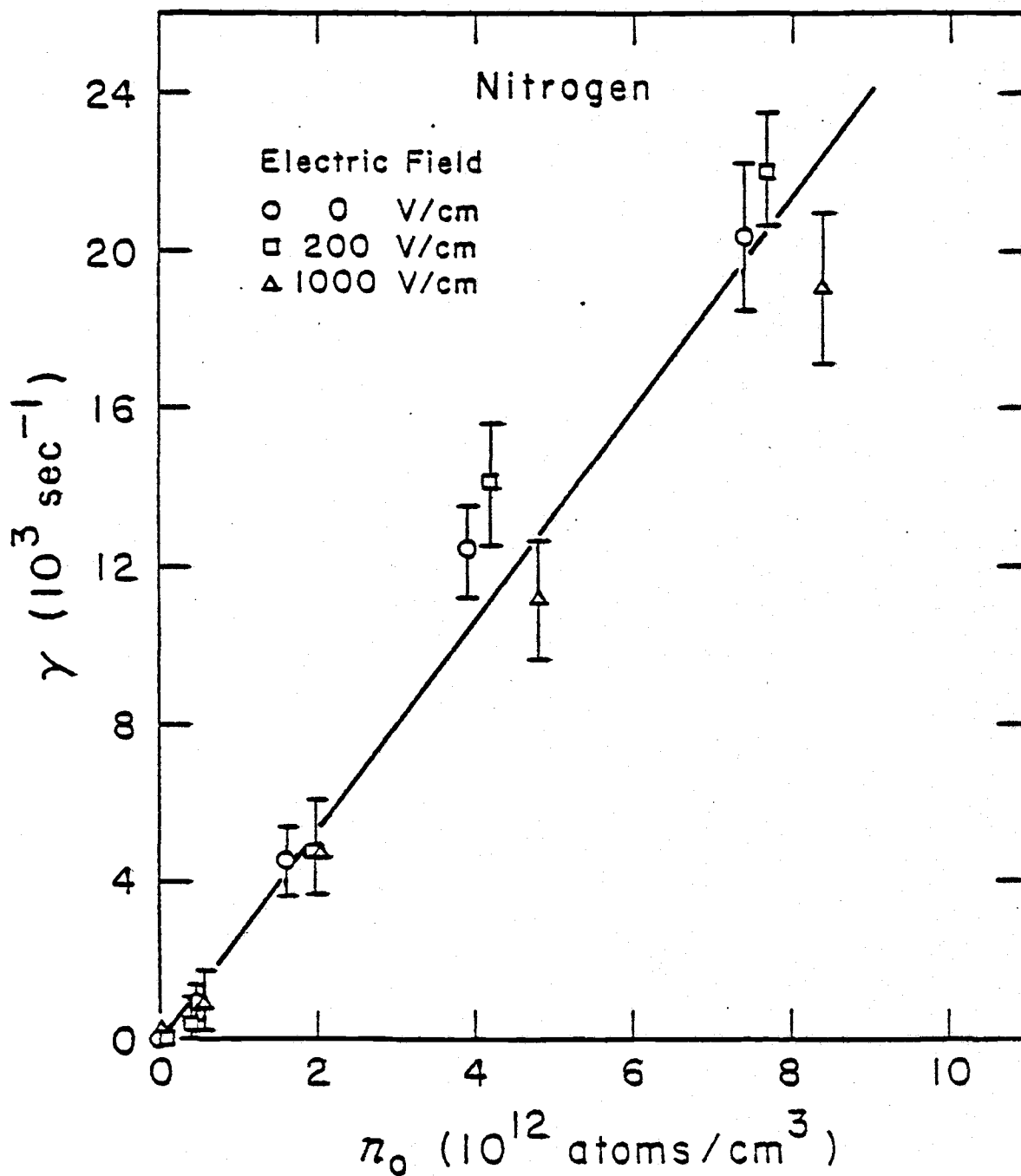


Figure 29. Slopes γ of \ln [channel-by-channel ratios] for nitrogen as a function of target gas density n_0 .

these lines, γ/n_0 , appear to be characteristic of the gas species and appear to be independent of the applied electric field. The error bars on the plotted points are determined from the lines of the maximum and minimum slopes which provide a reasonably good fit to the straight portions of $R_p(t)$ at large t .

The following discussion does not include the NH_3 data; these will be considered separately at the end of this section. The non-dependence of γ/n_0 on electric field is the major piece of experimental evidence against ionization as the beam loss mechanism, in agreement with Section 3.2, where the ionization probability in HR collisions with neutral atoms was shown to be negligible. It is therefore concluded that the loss of signal is due to the deflection of Li^* . Since the ratios $R_p(t)$ are calculated from TOF spectra obtained at the same electric field, radiative decay does not contribute to the exponential loss rates. And since ℓ -mixing collisions primarily shift the HR state distribution in the beam toward high- ℓ states, thereby reducing beam loss by radiative decay, it is reasonable to assume that ℓ -changing collisions do not contribute to the loss rates. Collisional de-excitation can also be eliminated as a possible mechanism, since such a process would depend on the principal quantum number n of the state that is de-excited; furthermore, it was shown in Section 3.2 that $\Delta n > 0$ transitions are of lower probability than $\Delta n = 0$ transitions.

It is therefore reasonable to conclude that of the two terms on the right side of Equation 6.3, $-\gamma t$ is associated with HR deflections. The two other physical processes occurring in the beam, radiative decay and ℓ -changing collisions, can be shown to account for $\ln F(t)$.

From gas kinetic theory, the deflection of HR atoms out of the beam is expected to lead to an exponential loss of signal

$$R'_p \approx e^{-n_o \sigma v t} \quad (6.4)$$

Here n_o is the density of the target gas and σ is the cross section for deflection of a HR atom with velocity v . The experimental loss rate γ can be identified with $n_o \sigma v$, giving

$$\gamma/n_o = \sigma v \quad (6.5)$$

The experimental values of γ/n_o are given in Table 2, together with calculated values of σv from Equation 3.53. The theoretical calculations are based on the assumption that the HR atom is scattered as a result of localized interaction between the core ion and the target gas atom (Section 3.3). The state of the distant Rydberg electron is approximately unaffected by this process. The lack of n -dependence of γ/n_o is consistent with this hypothesis. Similarly, Equation 6.5 suggests that

$$\sigma \propto 1/v, \quad (6.6)$$

which is consistent with the free-ion scattering cross sections described by Equation 3.48.

Table 2. Experimental and calculated values of σv for the five target gases.

Target Gas	α_p / a_o^3	Experimental $\sigma v = \gamma / n_o$ ($10^{-9} \text{ cm}^3 / \text{sec}$)	Calculated σv (Eq. 3.53) ($10^{-9} \text{ cm}^3 / \text{sec}$)
He	1.38	1.97 ± 0.40	1.75
Ne	2.67	1.88 ± 0.45	2.42
Ar	11.07	2.37 ± 0.65	4.94
H ₂	5.45	4.00 ± 0.65	3.47
N ₂	11.88	2.12 ± 0.60	5.12

The experimental and calculated values of σv are in excellent agreement for He, Ne, and H₂, and are within a factor of 2.5 for Ar and N₂. This agreement is to the author's knowledge the first experimental support of the free-ion interpretation of HR scattering. The theoretical values are subject to corrections from quantum scattering effects, which become important at the smallest scattering angles, and to short-range corrections to $V(r)$, which contribute to large-angle scattering. For the velocities in the present atomic beam, the observed cross sections are typically 10^{-14} cm^2 .

With NH_3 as target gas, the narrowing of TOF spectra observed was similar to that observed for each of the other target gases, but the effect occurred at much lower NH_3 partial pressures. Thus, as much narrowing was observed at an NH_3 partial pressure of $1 \mu\text{Torr}$ as was observed at a nitrogen pressure of $120 \mu\text{Torr}$. Channel-by-channel ratios and their slopes for the NH_3 data at zero electric field are shown in Figures 24 and 30, respectively. The maximum NH_3 partial pressure used was $3.2 \mu\text{Torr}$, because higher NH_3 densities poisoned the electron-emitting surface of the cathode.

The NH_3 data displayed in Figures 24 and 30 yield $\sigma v = 1.8 \times 10^{-7} \text{ cm}^3/\text{sec}$, which is about a factor of 100 larger than σv values measured for the other target gases. It appears that the beam loss mechanism with introduced NH_3 is different from the deflection process discussed above. Foltz, Latimer, West, Dunning and Stebbings (F3) measured the cross sections for the ionization of HR Xe atoms in (nf) states during collisions with various polar molecules, including NH_3 , as was discussed in Section 2.4. The measured cross sections increased sharply with n (approximately as n^4 , similar to Equation 2.20), and are in agreement with cross sections for a Matsuzawa-type process, also discussed in Section 2.4. With an average n of approximately 30, and a velocity of $2 \times 10^5 \text{ cm/sec}$ for the lithium beam in the present experiment, the cross section extracted from Figure 32 is $0.9 \times 10^{-12} \text{ cm}^2$, which is

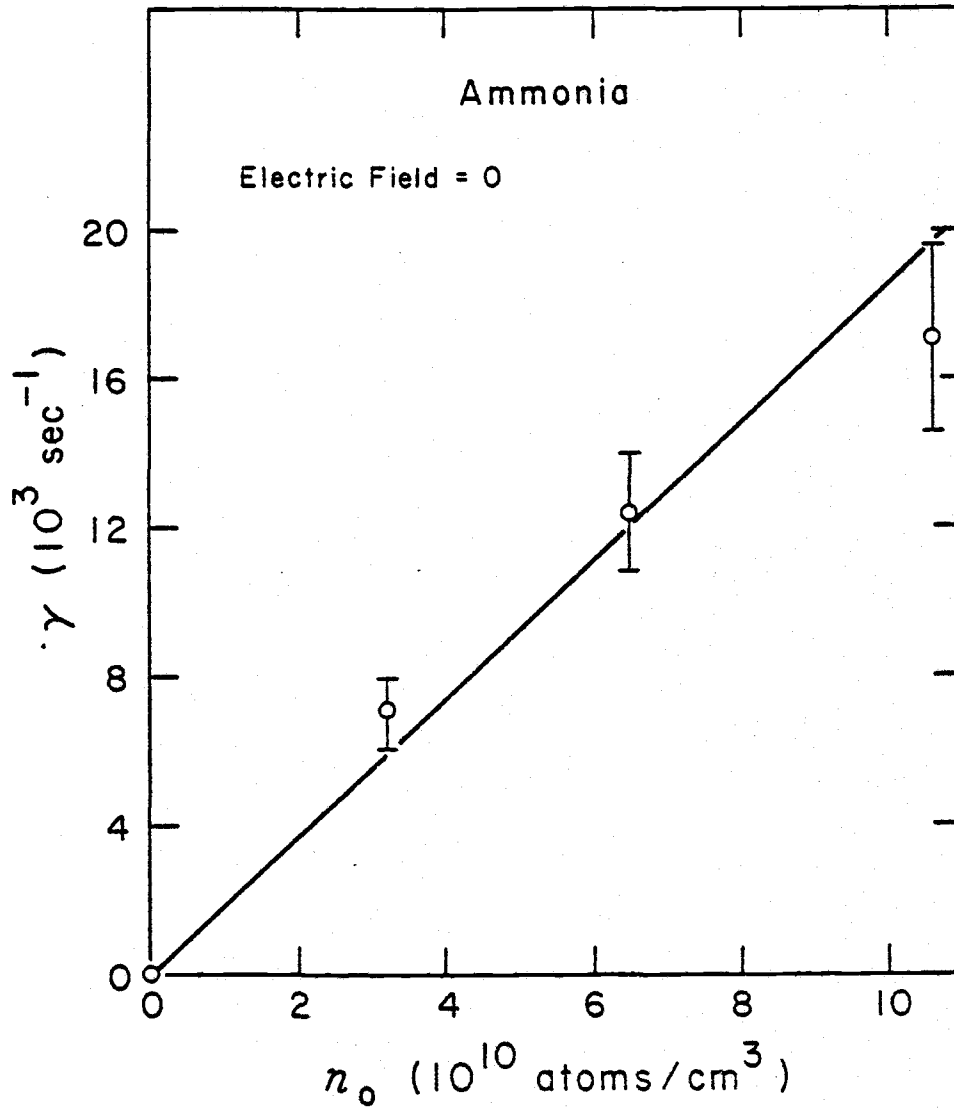


Figure 30. Slopes γ of \ln [channel-by-channel ratios] for ammonia as a function of target gas density n_0 .

within a factor of 2 of the Xe (30 f) ionization (by NH_3) cross section of $1.4 \times 10^{-12} \text{ cm}^2$ obtained by Foltz et al. It is evident from these NH_3 results that collisions between HR atoms and neutral atoms or non-polar and non-electronegative molecules proceed via a different mechanism than the nearly free HR electron interaction that has been proposed by Matsuzawa (M2). The results obtained in this experiment for target gases other than NH_3 support a free core-ion interaction with these target atoms. The classical scattering theory used to explain these results is adequate for the preliminary calculations presented here. However, a more complete theoretical effort is needed to provide a more thorough understanding of core-ion interactions at thermal energy. The results discussed in this section constitute the major findings of this thesis.

6.3 Angular-Momentum-Mixing Collisions

In this section, an analysis of the curved portions of $\ln R_p(t)$ in Figures 19 to 26 will be presented. A closer look at these $\ln R_p(t)$ plots and the rest of the collision data indicates that, in addition to the loss of signal rate at large flight times, there is also a gain in signal rate at smaller flight times, when the target gas pressure is low. This gain is best seen in channel-by-channel ratios as functions of pressure for preselected flight times (for example, analyzer channels 20, 40 and 60, corresponding to flight times of 110, 220 and

330 μ sec). The counting rates in each of these channels with the target gas present is divided by the counting rate in the corresponding channel with target gas absent. The resulting ratios, $R_t(p)$, for a helium target at electric fields 0.0, 0.2, and 1.0 kV/cm, are shown on a semi-log plot in Figure 31. Similar results were obtained for all the other target gases used, except NH_3 , and at all the electric fields. Only zero-field data were obtained for NH_3 , and they will not be considered in the rest of this analysis.

From the plots of $R_t(p)$ shown in Figure 31, and from the rest of the experimental data, it is seen that at lower pressures the counting rates recorded by the lower channels are larger than those recorded in the same channels at the base pressure. Thus, for all target gases studied, $\ln R_t(p)$ is positive for the lower channels at low pressures, becoming negative as the pressure is increased. This gain in signal rate is less evident at higher channels; for instance at channel 60, $\ln R_t(p)$ is negative at all pressures. There is more gain in signal rate for data obtained with applied electric fields than for zero-field data.

The following is a qualitative explanation of this phenomenon. It has been shown that the deflection cross section for HR atoms is inversely proportional to their velocity (Sections 3.3 and 6.2). The fastest atoms, those for which counting rates are stored in the lowest channels, are not scattered significantly at low pressures. These

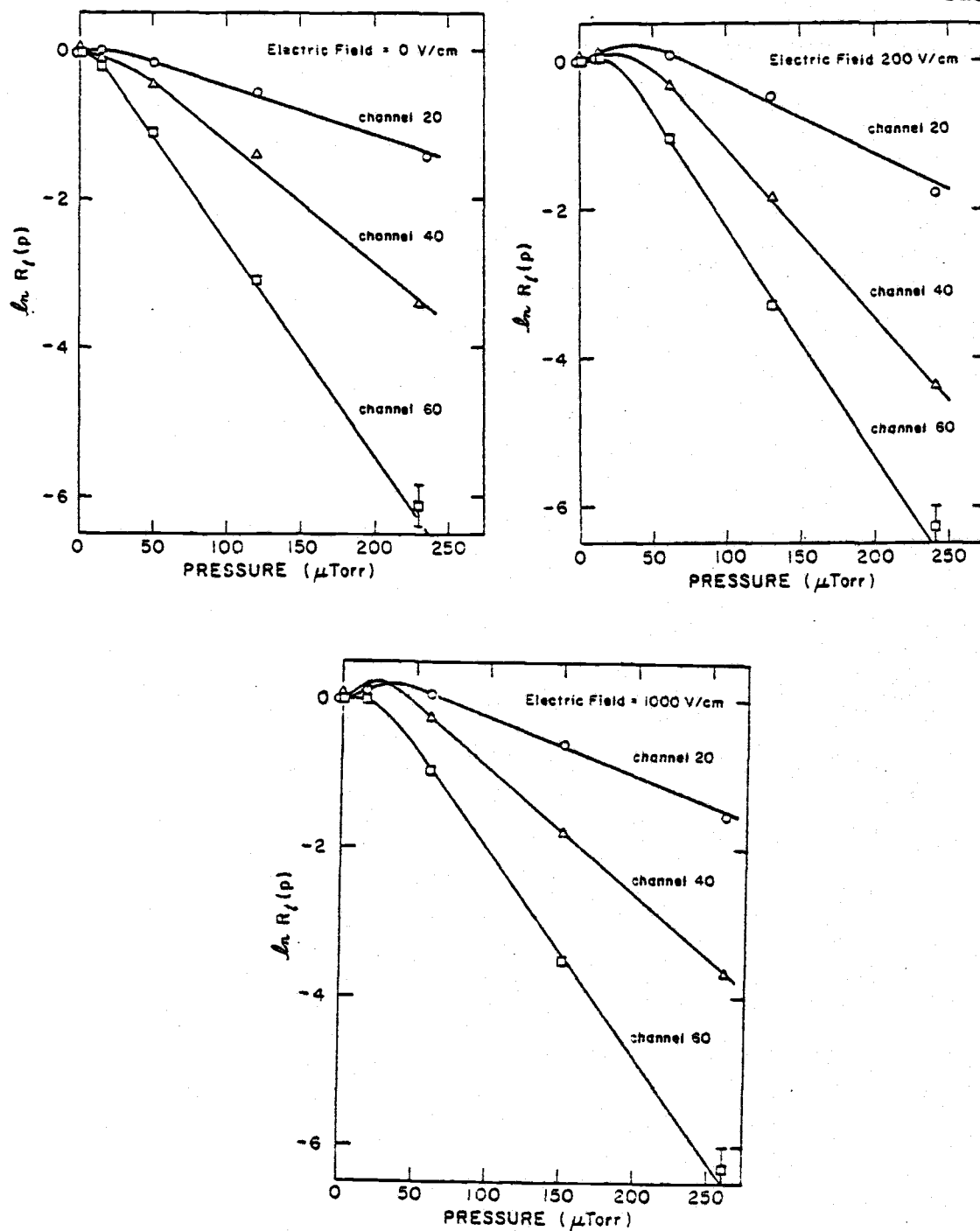


Figure 31. Logarithms of ratios of counting rates as functions of helium pressure. Results for analyzer channels 20, 40, and 60 are shown.

fast atoms experience an increased number of ℓ -mixing collisions as the pressure is increased, shifting the ℓ -distribution toward higher- ℓ values and smaller radiative decay rates. With the initial increase in pressure, the lower channels therefore record higher counting rates. As the pressure is raised further, the probability for the deflection of fast atoms increases until finally $\ln R_t(p)$ becomes negative, as the rates recorded in the low channels and at high pressures reduce to below base-pressure rates. With an applied electric field, the HR lithium atoms are in lower- n states, and in the absence of the target gas also in low- ℓ states, and therefore decay rapidly. When target gases are admitted, a large fraction of these lower- n states attain high ℓ -values and can survive in the beam. Higher- n states, on the other hand, have lifetimes long enough for them to survive the 35-cm flight, even when they are in low- ℓ states. The fractional increase in high- n states which survive in the beam is therefore expected to be smaller than that for low- n states, and therefore the enhancement in signal rate is larger with applied fields.

This explanation lends further support to the claim made earlier (Section 6.2), that of the two terms which make up $R_p(t)$, $F(t)$ is associated with ℓ -mixing collisions and radiative decay. These processes are thus seen to be responsible for the overall displacement of the experimental plots $\ln R_p(t)$, as well as their deviation from straight line behavior at low channel numbers. The function $F(t)$

therefore contains information concerning the cross sections for ℓ -mixing collisions.

If on one of the $\ln R_p(t)$ plots a line of slope $-\gamma$ is drawn through the point $(0,0)$, it would be parallel to the linear portion of $R_p(t)$ at large t , and it would represent $R_p(t)$ in the absence of radiative decay and ℓ -mixing collisions. The constant difference between this line and $\ln R_p(t)$ at large t is seen to be the intercept of the linear part of $\ln R_p(t)$ produced backwards toward $t = 0$. Since $\ln F(t)$ is the difference between $\ln R_p(t)$ and $-\gamma t$, this intercept is also seen to be equal to the value of $\ln F(t)$ at large t , and will be designated $\ln F_\infty$. Values of $\ln F_\infty(p)$, obtained as $t = 0$ intercepts of the experimental plots of $\ln R_p(t)$, are displayed in Figure 32 as functions of pressure for each of the target gases He, Ne, Ar, H_2 , and N_2 . The displayed points are seen to have large error bars and seem to show no electric field dependence. It is possible that there really is an n -dependence which is, however, masked by the scatter in the data. For the purpose of this analysis it will be assumed that there is no n -dependence. In Figure 32, it is seen that each $\ln F_\infty(p)$ initially increases with rising pressures up to about $50 \mu\text{Torr}$. It then remains constant with further increases in pressure. The maximum values $\ln F_{\text{max}}$ of $\ln F_\infty(p)$ for the five target gas species are shown in Table 3. While

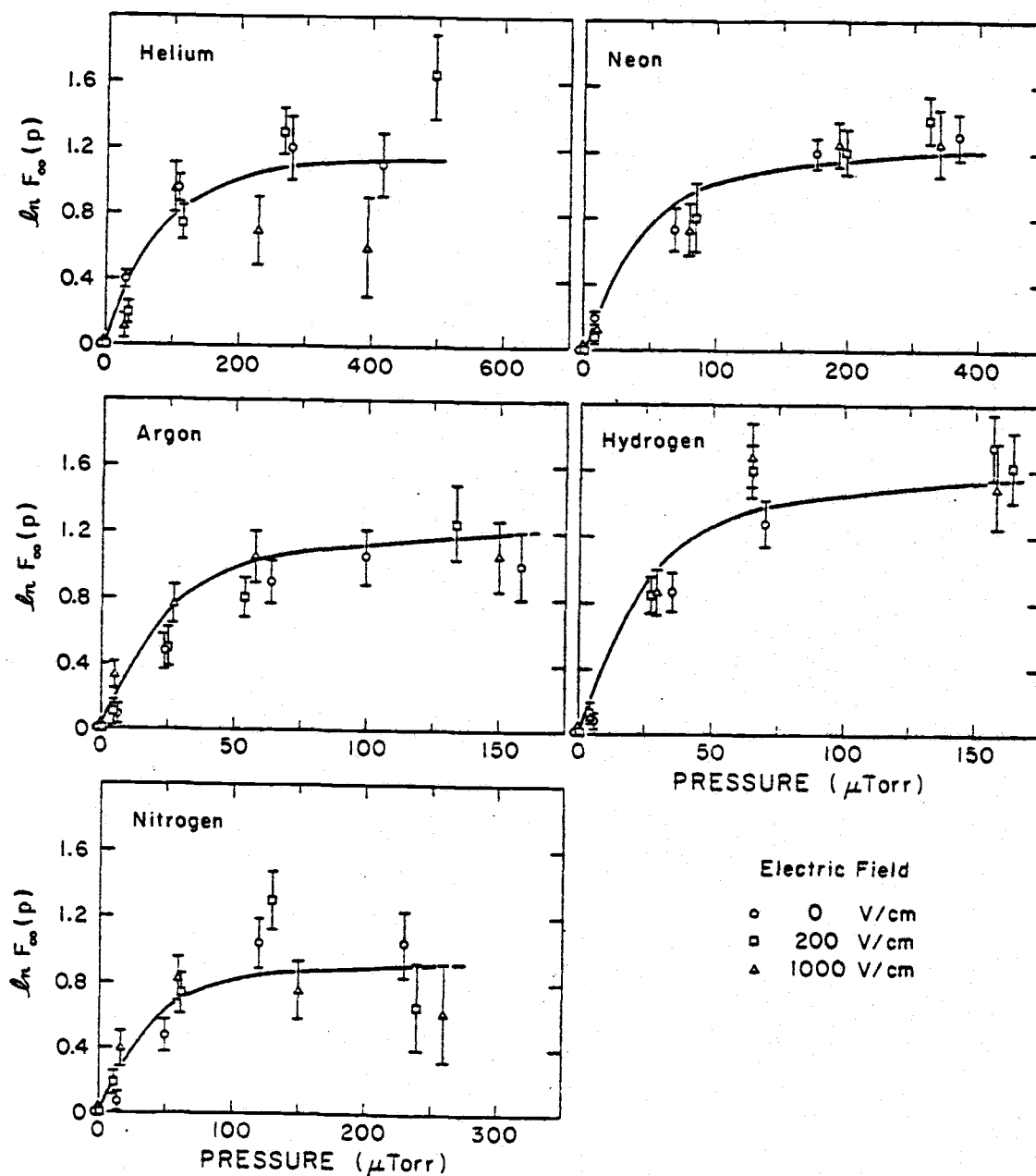


Figure 32. Intercepts $\ln F_\infty(p)$ of \ln [channel-by-channel ratios], as functions of target gas pressures. The line is a two-state model fit using the 30p decay rate for lithium (Figure 4), a value of $\ln F_{\text{max}}$ for the particular target gas (Table 3), and a pressure ratio p for best fit.

all of the rare gases have similar values $\ln F_{\max} \approx 1.2 \pm 0.4$, the hydrogen and nitrogen data yield the values 1.6 ± 0.2 and 0.9 ± 0.4 , respectively. However, the uncertainties in these values overlap each other, and the differences shown may not be significant. An average value $\ln F_{\max} = 1.2 \pm 0.5$ is obtained. This experimental quantity will be used both to parameterize the two-state collision model described in Section 3.4, and to serve as a goodness-of-fit measure for the complete collision model given by Equation 3.58, which is also discussed in the Appendix.

Table 3. Experimental values of $\ln F_{\max}$, obtained from the maxima of channel-by-channel ratio intercepts.

Target Gas	$\ln F_{\max}$
He	1.2 ± 0.4
Ne	1.3 ± 0.2
Ar	1.1 ± 0.3
H ₂	1.6 ± 0.2
N ₂	0.9 ± 0.4

The large t ($t \rightarrow \infty$) limit of the two-state model, Equation 3.70, is easily seen to be

$$F_{\infty}(p) = \frac{1 + \Gamma/\alpha_0}{1 + \Gamma/\alpha_p}. \quad (6.8)$$

This equation is independent of flight time t , depending only on the target gas pressure. At large pressures, Γ/α_p is small in comparison to 1. Thus in the double limit of large p and large t it is seen that

$$F_{\max} = 1 + \frac{\Gamma}{\alpha_0}, \quad (6.9)$$

which is independent of pressure, as has been verified experimentally. The experimental values of $\ln F_{\max}$ then imply

$$\frac{\Gamma}{\alpha_0} = e^{\ln F_{\max}} - 1 = 2.3 \pm 1.6. \quad (6.10)$$

It is convenient to rewrite Equation 3.70 in terms of this quantity, which will be denoted by ϵ . One other quantity will be required for complete parameterization of 3.70:

$$\frac{\alpha_p}{\alpha_0} = \frac{n_p}{n_0} = \frac{p}{p_0} = p', \quad (6.11)$$

where p' is the pressure ratio. Substitution of p' and ϵ into Equation 3.70 readily yields

$$F(t) = \frac{1+\epsilon}{1+\frac{\epsilon}{p'}} \frac{1+\frac{\epsilon}{p'} e^{-\Gamma(1+p'/\epsilon)t}}{1+\epsilon e^{-\Gamma(1+1/\epsilon)t}}, \quad (6.12)$$

from which

$$F_{\infty}(p) = \frac{1+\epsilon}{1+\frac{\epsilon}{p'}} \quad (6.13)$$

The use of Equations 6.12 and 6.13 to fit the experimental distributions $F(t)$ and $F_{\infty}(p)$, which were described earlier, will be discussed shortly.

The l -changing cross section $\sigma^{\Delta l}$ can now be extracted from the two-state model. Since

$$\alpha_0 = n_0 \sigma^{\Delta l} v \frac{g}{g+1}, \quad \text{where } g \gg 1,$$

Equation 6.10 gives an order of magnitude

$$\sigma^{\Delta l} = \frac{\Gamma}{n_0 \epsilon v} \approx 10^{-13} \text{ cm}^2,$$

which is in agreement with the values obtained by Gallagher et al. as discussed in Section 2.5. The lithium 30 p decay rate of $2 \times 10^4 \text{ sec}^{-1}$, obtained by extrapolation (Figure 4), has been used for Γ , since the model assumes a low- l state for state $|1\rangle$ and since the HR lithium atoms in the experimental beam have an average n of approximately 30. An average value $v \approx 2 \times 10^5 \text{ cm/sec}$ was taken for the Li atomic beam.

Cross sections for l -mixing are obtained from the complete collision model by numerical integration of Equation 3.58 (Appendix). The experimentally determined value $\ln F_{\max} \approx 1.2 \pm 0.5$, is used as the criterion for a good fit. Because the shape of $F(t)$ depends

on both ℓ -changing collisions and radiative decay, the value of $\sigma^{\Delta\ell}$ obtained by this procedure is determined by the model assumed for $\Gamma_{n\ell}$.

Radiative decay rates are well known for lithium p states and circular orbit states (Figure 4). However, the curve connecting these two points for a given n is not so well known. In Figure 33, three possible functional forms for the variation with ℓ of the decay rates of lithium with $n = 30$ are displayed. The first model, Curve 1, connects the p-state and the circular-orbit-state decay rates with an exponential function

$$\Gamma_{30\ell} = (1.841 \times 10^4 \text{ sec}^{-1}) e^{-0.128\ell}, \quad (6.14)$$

which has the least initial slope of the three models. The second formula

$$\Gamma_{n\ell} = \frac{1.91 \times 10^{10} \text{ sec}^{-1}}{n^{2.44} (\ell + 8.43)^{2.56}} \quad (6.15)$$

resembles an expression for hydrogen lifetimes, given by Herrick (H4), and has been modified to fit lithium decay rates at both end points. This is expected to be the most realistic model of the three, since the lifetimes of HR atoms other than hydrogen tend to be hydrogenic (Section 2.3). This model also attempts to incorporate the n -dependence, as well as the ℓ -dependence. In these first two models,

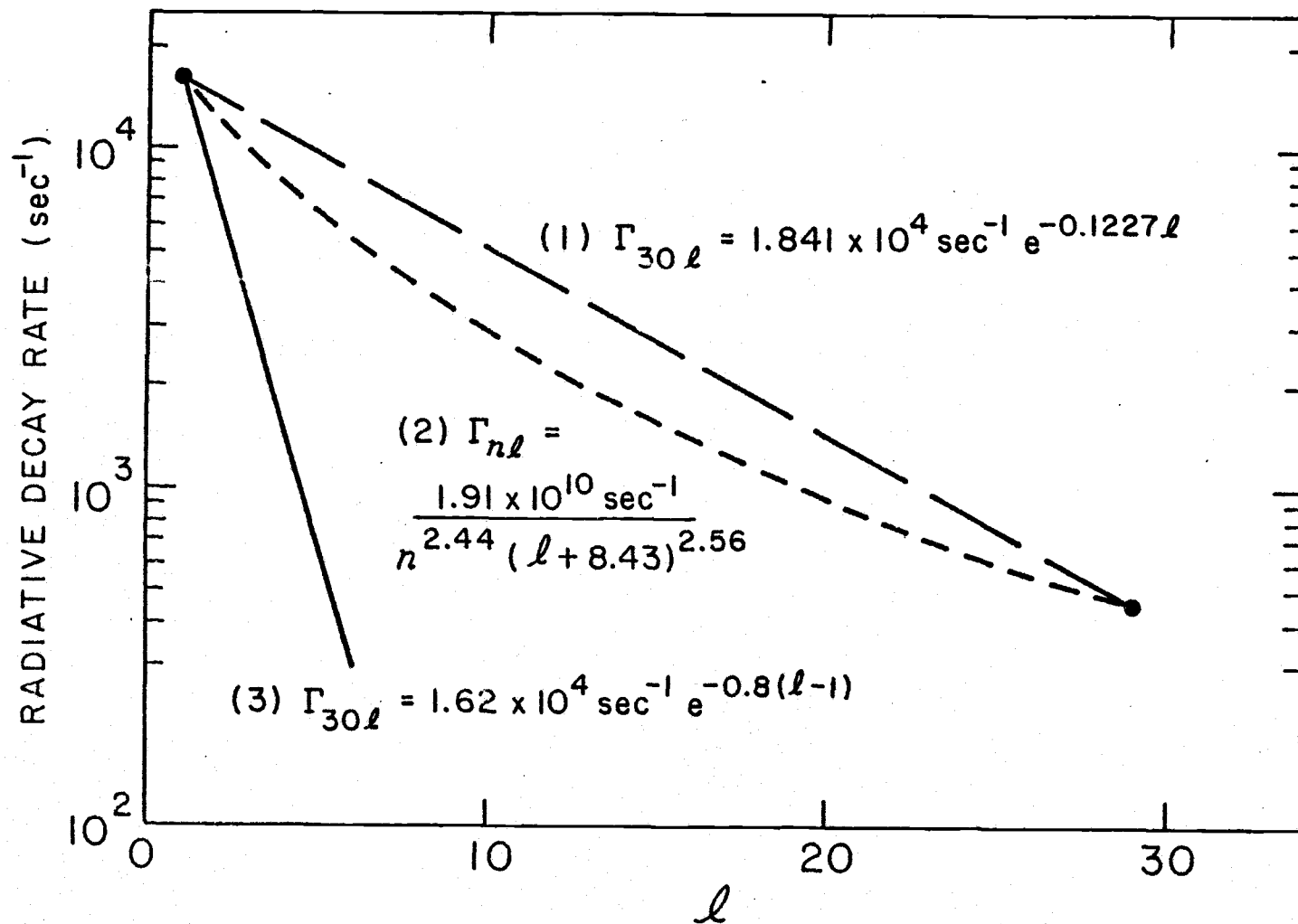


Figure 33. Three models for the variation of the radiative decay rate for lithium (in the $n = 30$ state) with l .

the decay rates are seen to be slowly varying functions of ℓ ; an atom which is initially in a p state requires a large change in ℓ to reduce its decay rate sufficiently to ensure its survival in the beam.

The third function,

$$\Gamma_{30\ell} = 1.62 \times 10^4 \text{ sec}^{-1} e^{-0.8(\ell-1)}, \quad (6.16)$$

also exponential, is seen to give decay rates which fall off very fast with increasing ℓ . For this model, only a small increase in ℓ is required to put an atom in the non-decaying category. This model is rather unrealistic, since it does not include the circular-orbit-state decay rate.

With each of these expressions for $\Gamma_{n\ell}$, $\ln F(t)$ is calculated and plotted for several values of $\sigma^{\Delta\ell}$ -guesses, at a fixed high pressure of 200 μ Torr. The values of $\sigma^{\Delta\ell}$ which give the best fit for each of the three models are shown in Table 4. All $\sigma^{\Delta\ell}$ so obtained are within a factor of 1.5 of each other. This is considered very good agreement among the models, since the two exponential functions were chosen to give the maximum and minimum variation of $\Gamma_{n\ell}$ with ℓ , within reasonable limits. Table 4 therefore indicates that the cross section $\sigma^{\Delta\ell}$ for ℓ -changing during HR and neutral gas atom collisions lies between the limits 0.5 and $2.2 \times 10^{-13} \text{ cm}^2$. The results are summarized by $\sigma^{\Delta\ell} = (1.3 \pm 0.8) \times 10^{-13} \text{ cm}^2$.

Table 4. Angular-momentum-mixing cross sections $\sigma^{\Delta l}$ calculated from the complete model, using the three decay models for the $n = 30$ state of lithium (Figure 33) and observed values of $\ln F_{\max}$.

$\ln F_{\max}$	$\sigma^{\Delta l} (10^{-13} \text{ cm}^2)$		
	Model 1	Model 2	Model 3
1.5	0.54	0.83	1.14
1.2	1.31	1.34	1.71
0.9	2.08	1.85	2.27

The l -changing cross sections

$$\sigma^{\Delta l} = [0.38(7) \text{ to } 5.4(7)] \times 10^{-13} \text{ cm}^2 \text{ observed by Gallagher et al.}$$

(G5, G6) for f states of Na depend on the target gas species as well as on n , as was discussed in Section 2, 4. Neither of these two dependences can be extracted from the present data; a detailed comparison between their results and those obtained in this section cannot be made. However, there is order of magnitude agreement. Please see a restricted model with $\Delta l = \pm 1$ at the end of the Appendix.

Calculations based on Equations 3.58 and 6.12, the complete and two-state models, have been used to fit experimental $\ln F(t)$ curves. All of these plots are shown in Figure 34, together with experimental $\ln F(t)$ distributions for neon at a pressure of 262 μTorr and an electric field of 0.2 kV/cm. The neon curve is obtained by addition of $-\gamma t$, Figure 28, to the channel-by-channel ratios shown in Figure 20. At lower channel numbers, below channel 20, the data are significantly affected by the presence of the

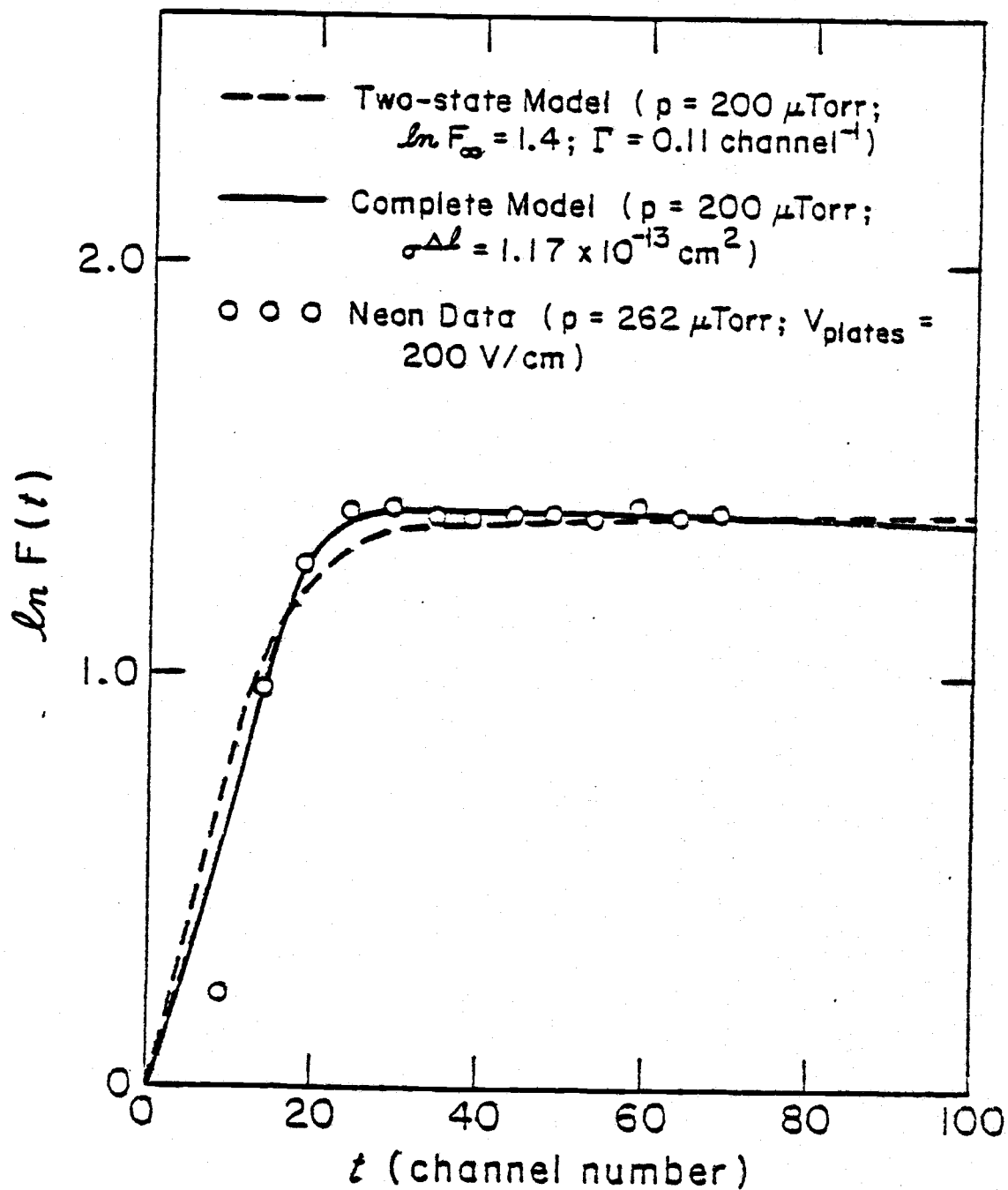


Figure 34. Complete (solid line) and two-state (dashed line) model fits to observed $\ln F(t)$ (dots) for neon target.

fast peak shown in Figure 14; these points are not shown in Figure 34.

The curves calculated from the complete model show a drop in $F(t)$ below the maximum value at the higher channels. This reduction is not apparent in the two-state model. It is, however, expected for the complete model, in which all ℓ -substates have equal transition probability and arbitrary ℓ -changes are allowed. Though initially only the low- ℓ states are populated, the population is transferred to the high- ℓ states quickly. Those atoms which are in high- ℓ states, and which have the longest lifetimes, can make further collisions which can change their angular momentum quantum numbers back to lower values, so that the atoms can decay radiatively. This repopulation of low- ℓ states then gives rise to the reduction in $F(t)$ at large flight times. The scatter in the experimental points at high channels prevents observation of this effect. The three decay-rate models discussed earlier lead to similar shapes for $F(t)$. The theoretical curves are in excellent agreement with the experimental ones, for the data shown in Figure 34, as well as the rest of the experimental data.

Similar agreement is obtained between theory and experiment when $\ln F_{\infty}(p)$ curves are fitted by calculations based on the complete model (Equation 3.58) as well as the two-state model (Equation 6.13). The fitted data are shown in Figure 32. For these two-state model curves, $\Gamma \approx 2 \times 10^4 \text{ sec}^{-1}$ and the experimentally

determined value of ϵ (Equation 6.10) are used; the pressure ratios p' are adjusted to fit. For example, the displayed nitrogen curve is obtained with a pressure ratio p' consistent with a base pressure of about 12 μ Torr. The base pressure in the present experiment was 2 μ Torr, as measured by an ionization gauge. However, the composition of the background gas is unknown. The correction factor which converts this pressure to an absolute pressure cannot be obtained by the MKS capacitance manometer, since the latter instrument cannot give reliable readings below 10^{-5} Torr. Use of the correction factor for dry air indicates that the true background pressure lies between 1 and 5 μ Torr, but it is probably not as high as 12 μ Torr.

The cross sections for the interaction of HR atoms with NH_3 , which were discussed in Section 6.2, are of the order of 100 times those obtained for HR collisions with the other target gases used in this experiment. Additional molecular gases such as NO_2 , NO , and H_2S have also been observed to have very large cross sections for interactions with HR atoms. Though these very large cross sections have been associated with ionizations of HR atoms, it is possible that electronegative and polar molecules have large l -changing cross sections as well (larger than those for rare gas atoms). If this were the case with H_2O , the presence of traces of water vapor in the reaction chamber would result in l -changes equivalent to those which would result from a higher pressure of a rare gas, and thus explain

the discrepancy between the experimental and theoretical base pressure values. This hypothesis is even more plausible when combined with the fact that ℓ -changing collisions are observed even at background pressures of order $1 \mu\text{Torr}$.

6.4 Summary of Conclusions

A time-of-flight study of lithium atoms, excited to high Rydberg states by electron impact, has been presented. The most important conclusion arrived at was that in collisions with neutral atoms or molecules (He, Ne, Ar, H_2 , N_2) at thermal energies, a HR atom can be deflected. The observed cross sections σ for this process, which are tabulated in Table 2, are inversely proportional to the HR atom velocity and independent of its state. They are in agreement with a theoretical calculation based on the idea of a localized core-ion interaction, and are typically of order 10^{-14} cm^2 . Momentum and kinetic energy conservation considerations were used to show that ionization was of negligible probability in these collisions. This conclusion was confirmed experimentally by the lack of electric field dependence of σ . Similar measurements with a polar molecule, NH_3 , yield a cross section which is at least 100 times those for the other gases and consistent with the cross section for a Matsuzawa-type HR atom ionization in collision with, NH_3 , thus confirming that the processes are different.

From lifetime measurements with applied electric fields it was concluded that the HR lithium atoms are in predominantly high angular momentum (high- ℓ) states, even though low- ℓ states are expected to be excited by electron impact.

Evidence was presented showing that the source of high- ℓ states in this experiment was not:

- (a) the Fano effect (high- ℓ excitation when exciting electron energy is within a fraction of 1 eV of threshold);
- (b) the quadratic Zeeman effect (ℓ -mixing via the A^2 term of the interaction Hamiltonian);
- (c) multiple collisions with exciting electrons (the first electron excites a HR state, with further collisions of the excited atom with electrons leading to ℓ -changes).

The results of the collision measurements, discussed in Section 6.3, indicate that the source of high- ℓ states is elastic collisions between HR and neutral atoms. An ℓ -changing cross section which is consistent with previous measurements was obtained. These results are explained by a collision model (and a two-state, simplified version of it) in which transitions to all ℓ -substates are equally probable and arbitrary ℓ -changes are allowed during collision. A similar model with the restriction $\Delta\ell = \pm 1$ was unsatisfactory, indicating that this selection rule is probably not applicable in ℓ -changing collisions.

6.5 Suggestions for Further Study

Various unanswered questions from this study, and a new technique which derives from it, will now be proposed for further investigation. The fast peak, introduced in Section 5.2 and shown in Figure 14, needs to be better understood. It is believed that this peak is due to dissociative excitation of Li_2 molecules. The flight times for HR atoms with counts stored in the fast peak correspond to kinetic energies of about 6 eV. If this were released kinetic energy from the dissociation of Li_2 molecules, it would imply a molecular binding energy of about 12 eV. Since the fast peak has been observed at exciting energies of 10 eV or less, with an appearance threshold of approximately 5.5 eV, it is possible that Li_2 dissociative excitation requires at least 2 electrons. One therefore expects the intensity of the fast peak to be proportional to the exciting electron density raised to a power n . Measurements of the ratio of the fast peak integral to the thermal peak integral as a function of the electron current indicate that n is between 2 and 3. However, the intensity of the fast peak is a problem. Lithium molecules are expected to constitute about 1% of natural lithium, at the temperature of the beam oven. With this information, an estimate of the cross section for a two-electron process that would yield the observed fast peak intensities is extremely large. The interaction process is also not well understood.

Further investigation of cross sections for HR collisions with polar molecules such as SO_2 , NO_2 , NH_3 , and NO is worthwhile. In particular, the electric field dependence of these cross sections, measured by the experimental technique used in the present study, can lead to a better understanding of the differences between HR deflection and ionization processes, and l -changing cross sections can be found.

This study also suggests a new method for ion-atom and ion-molecule experiments at thermal energies. Ion-neutral measurements can lead to a better understanding of the ion-neutral interaction potential. Ion beam investigations to date have been restricted to energies above 1 eV, because of the difficulty of producing and maintaining beams of charged particles at lower energies (McDaniel and Mason, M5). Drift tube techniques have been used at thermal energies, but these can only yield mobilities and not differential cross sections. In a thermal beam of HR atoms, such as used in this study, the excited electrons protect the core ions from residual fields, but apparently do not interfere during core ion-atom interactions. With this method, velocity dependences of the ion-neutral cross sections can be measured, while with slight modifications of the apparatus differential cross sections can be obtained.

BIBLIOGRAPHY

- A1. E. Amaldi and E. Segre, *Nuovo Cimento* 11, 145 (1934).
- B1. D.S. Bailey, J.R. Hiskes, and A.C. Riviere, *Nucl. Fusion* 5, 41 (1964).
- B2. J.E. Bayfield and P.M. Koch, *Phys. Rev. Lett.* 33, 258 (1974).
- B3. J.E. Bayfield, G.A. Khayrallah and P.M. Koch, *Phys. Rev. A* 9, 209 (1974).
- B4. H.A. Bethe and E.E. Salpeter, Quantum Mechanics of One and Two Electron Atoms (Springer-Verlag, Berlin, 1957) p. 248 ff.
- B5. D.R. Bates and A. Damgaard, *Phil. Trans. Roy. Soc. London* 242, 101 (1949).
- C1. V. Čermák and Z. Herman, *Collect. Czech. Chem. Comm.* 29, 953 (1964).
- C2. V. Chaplik, *Sov. Phys. -JETP* 27, 178 (1968) [*Zh. Eksp. Teor. Fiz.* 54, 332 (1968)].
- D1. T.W. Ducas, M.G. Littman, R.R. Freeman and D. Kleppner, *Phys. Rev. Lett.* 35, 366 (1975).
- D2. S. Dushman, Scientific Foundations of Vacuum Technique ed. J.M. Lafferty (John Wiley and Sons, Inc., New York 1962) p. 234.
- E1. B. Edlén, Atomic Spectra, Secs. 20 and 33 in Handbuch der Physik, Vol. 27 ed. S. Flugge (Springer-Verlag, Berlin, 1964).
- E2. D.S. Evans, *Rev. Sci. Instr.* 36, 375 (1965).
- F1. E. Fermi, *Nuovo Cimento* 11, 157 (1934).
- F2. R.R. Freeman and D. Kleppner, *Phys. Rev. A* 14 1614 (1976).
- F3. G.W. Foltz, C.J. Latimer, W.P. West, F.B. Dunning and R.F. Stebbings, *Abstr. Fifth Internat. Conf. on Atomic Physics, Berkeley Calif.* (1976) 256.

- F4. U. Fano, J. Phys. B: Atom. Molec. Phys. 7 L401 (1974).
- F5. N.V. Fedorenko, V.A. Akudinov, R.N. Il'in, Sov. Phys. - Tech. Phys. 10, 461 (1965) [Zh. Tekh. Fiz. 35, 585 (1965)].
- F6. R.S. Freund, J.A. Schiavone, and D.E. Donohue, Abstr. Fifth Internat. Conf. on Atomic Physics, Berkeley Calif. (1976) 376.
- G1. T.F. Gallagher, S.A. Edelstein and R.M. Hill, Phys. Rev. A 13, 1448 (1976).
- G2. T.F. Gallagher, S.A. Edelstein and R.M. Hill, Phys. Rev. A 14, 744 (1976).
- G3. T.F. Gallagher, S.A. Edelstein and R.M. Hill, Phys. Rev. A 11, 504 (1975).
- G4. T.F. Gallagher, S.A. Edelstein and R.M. Hill, Phys. Rev. A 14, 2360 (1976).
- G5. T.F. Gallagher, S.A. Edelstein and R.M. Hill, Phys. Rev. Lett. 35, 644 (1975).
- G6. T.F. Gallagher, S.A. Edelstein and R.M. Hill, Phys. Rev. A 15, 1945 (1977).
- G7. J.I. Gersten, Phys. Rev. A 14, 1354 (1976).
- G8. H. Goldstein, Classical Mechanics (Addison-Wesley Publishing Co., Inc. Reading Massachusetts 1965) Chapter 3 and pp. 87-89.
- H1. B. Hoglund and P.G. Metzger, Science 150, 339 (1965).
- H2. J.R. Hiskes, C. Tarter and D.A. Moody, Phys. Rev. 133 A, 424 (1964).
- H3. H. Hotop and A. Niehaus, J. Chem. Phys. 47, 2506 (1967).
- H4. D.R. Herrick, Phys. Rev. A 12, 1949 (1975).
- H5. J.B. Hasted, Physics of Atomic Collisions, (Butterworth Inc., Washington, D.C. 1964) p. 341.
- I1. R.N. Il'in, in Atomic Physics 3, ed S.J. Smith and G.K. Walters (Plenum, New York 1973) p. 309.

- I2. R.N. Il'in, V.A. Oparin, I.T. Serenkov, E.S. Solov'ev and N.V. Fedorenko, *Sov. Phys. -JETP* 32, 59 (1971) [*Zh. Eksp. Teor. Fiz.* 59, 103 (1970)].
- I3. R.N. Il'in, B.E. Kikiani, V.A. Oparin, E.S. Solov'ev, and N.V. Fedorenko, *Sov. Phys. -JETP* 20, 835 (1965) [*Zh. Eksp. Teor. Fiz.* 47, 1235 (1964)].
- I4. R.N. Il'in, V.A. Oparin, E.S. Solov'ev, and N.V. Fedorenko, *Sov. Phys. -Tech. Phys.* 11, 921 (1967) [*Zh. Tekh. Fiz.* 36, 1241 (1966)].
- J1. R.K. Janev, *J. Phys. B: Atom. Molec. Phys.* 7, L359 (1974).
- K1. N.S. Kardashev, *Sov. Astron. -AJ* 3, 813 (1959) [*Astron. Zh.* 36, 839 (1959)].
- K2. D. Kleppner, in *Atomic Physics* 5, ed. R. Marrus, M. Prior and H. Shugart, (Plenum, New York, 1977) p. 269.
- K3. S.E. Kupriyanov, *Sov. Phys.* 21, 311 (1965) [*Zh. Eksp. Teor. Fiz.* 48, 467 (1965)].
- K4. S.E. Kupriyanov, *Sov. Phys. -JETP* 24, 674 (1967) [*Zh. Eksp. Teor. Fiz.* 51, 1011 (1966)].
- K5. S.E. Kupriyanov, *Sov. Phys. -JETP* 28, 240 (1969) [*Zh. Eksp. Teor. Fiz.* 55, 460 (1968)].
- K6. P.M. Koch and J.E. Bayfield, *Phys. Rev. Lett.* 34, 448 (1975).
- K7. S.E. Kupriyanov, *JETP Lett.* 5, (1967) [*Zh. ETF Pisma* 5, 245 (1967)].
- K8. C.A. Kocher and C.E. Fairchild, To be published.
- K9. C.A. Kocher and A.J. Smith, *Phys. Lett.* 61A, 305 (1977).
- K10. C.A. Kocher and A.J. Smith, To be published.
- L1. C. Lanczos, *Z. Phys.* 68, 204 (1931).
- L2. L.D. Landau and E.M. Lifshitz, *Quantum Mechanics*, Sections 37 and 77, (Pergamon Press, London, 1958).

- L3. A. Lundberg and S. Svanberg, *Phys. Lett.* 56 A, 31 (1936).
- L4. M. G. Littman, M. L. Zimmerman, T. W. Lucas, R. R. Freeman and D. Kleppner, *Phys. Rev. Lett.* 36, 788 (1976).
- M1. C. E. Moore, Atomic Energy Levels, Natl. Bur. Std. Circ. 467 (U.S. GPO, Washington D. C. 1958) Vol III.
- M2. M. Matsuzawa, *J. Chem. Phys.* 55, 2685 (1971).
- M3. H. S. W. Massey and E. H. S. Burhop, Electronic and Ionic Impact Phenomena (Oxford University Press, London, 1952) p.
- M4. G. A. Martin, (Data Center on Atomic Transition Probabilities, Natl. Bur. Std.) private communication (1977).
- M5. E. W. McDaniel and E. A. Mason, The Mobility and Diffusion of Ions in Gases (Wiley, New York, 1973), Sec. 6-3.
- O1. R. F. Olson, *Phys. Rev. A* 15, 631 (1977).
- R1. A. C. Riviere, D. R. Sweetman, Proc. 6th Intern. Conf. Ionization Phenomena in Gases, Paris, 1963, p. 105.
- R2. M. H. Rice and R. H. Good, *J. Opt. Soc. Amer.* 52, 239 (1962).
- R3. A. C. Riviere and D. R. Sweetman, in Atomic Collision Processes, ed. M. R. C. McDowell (North Holland, Amsterdam 1964) p. 734.
- R4. N. Ramsey, Molecular Beams, (London, Oxford University Press 1963) p. 20 and 364f.
- S1. R. F. Stebbings, *Science* 193, 537 (1976).
- S2. T. Shibata, T. Fukuyama and K. Kuchitsu, *Bull. Chem. Soc. Jap.* 47, 2883 (1974).
- S3. J. A. Schiavone, D. E. Donohue, D. R. Herrick and R. S. Freund, *Phys. Rev. A* 16, 48 (1977).
- S4. R. F. Stebbings, C. J. Latimer, W. P. West, F. B. Dunning and T. B. Cook, *Phys. Rev. A* 12, 1453 (1975).

- S5. K. C. Smyth, J. A. Schiavone, and R. S. Freund, *J. Chem. Phys.* 59, 5225 (1973).
- S6. G. A. Surskii, S. E. Kupriyanov, *Sov. Phys. -JETP* 27, 61 (1968) [*Zh. Eksp. Teor. Fiz.* 54, 109 (1968)].
- S7. M. J. Seaton, *Proc. Phys. Soc.* 88, 801 (1966).
- T1. R. Von Traubenberg, R. Gebauer and G. Lewin, *Naturwiss* 18, 417 (1930).
- V1. E. A. Vainshtein, *Opt. Spectr.* 18, 1538 (1965).
- W1. W. L. Wiese, M. W. Smith, and B. M. Glennon, Atomic Transition Probabilities, Vol I Nat. Bur. Std. NSRDS-NBS4 (1966).
- W2. W. P. West, G. W. Foltz, F. B. Dunning, C. J. Latimer and R. F. Stebbings, *Phys. Rev. Lett.* 36, 854 (1976).

APPENDIX

APPENDIX

Numerical Solution for the Complete Collision Model

The following is a description of the numerical technique used to solve the complete, arbitrary ℓ -change collision model, Equation 3.58, which may be written as a difference equation

$$\Delta P(n, \ell, t) = \left\{ n_0 \sigma^v \frac{2\ell+1}{n} \sum_{\ell'} P(n, \ell', t) - [n_0 \sigma^{\Delta\ell} v + n_0 \sigma^s v + \Gamma_{n\ell}] P(n, \ell, t) \right\} \Delta t \quad (\text{A1})$$

Here n_0 is the target gas density, $\sigma^{\Delta\ell}$ and σ^s are the HR ℓ -changing and scattering cross sections, v is the velocity of the atom, n and ℓ are its principal azimuthal quantum numbers, and t is the transit time. Equation A1 can be solved for $P(n, \ell, t)$, if the initial population $P(n, \ell, 0)$ is assumed and the constants $\sigma^{\Delta\ell}$, σ^s , $\Gamma_{n\ell}$, v and n_0 are known. The flight-time t is divided into a number of small intervals, each of width Δt ; the change in $P(n, \ell, t)$ is then calculated from the right side of Equation A1 and added to the old value of $P(n, \ell, t)$ in order to obtain the current value. This process can then be repeated for each interval Δt .

If the term containing the summation did not appear in Equation A1, it would have an exponential solution

$$P \propto e^{-\alpha t}, \quad (\text{A2})$$

with

$$\alpha = \Gamma_{nl} + n_o v(\sigma^s + \sigma^{\Delta l}).$$

This would give $\Delta P \approx -\alpha \Delta t$, provided $\alpha \Delta t$ is small. Thus, the condition on the size of Δt is approximately

$$n_o v(\sigma^s + \sigma^{\Delta l}) \Delta t \ll 1. \quad (\text{A3})$$

Since the number of computations depends on the size of Δt , some care must be exercised in the choice of Δt . The value $\Delta t = 0.1$ channel (where 1 channel corresponds to $5.5 \mu\text{sec}$) satisfies condition A3, but does not require too many computations.

The procedure described above was carried out by an electronic computer. The Fortran IV program by which this is done uses three column matrices, PLT, PT and DPLT, corresponding to $P(n, l, t)$, $P(t) = \sum_{l'} P(n, l', t)$ and $\Delta P(n, l, t)$. The unit of time used in this calculation is one channel, which allows direct comparison of calculated and experimental time-of-flight distributions. Initially,

$$\left. \begin{aligned} \text{PLT}(1) &= 1 \\ \text{PLT}(i) &= 0, \quad \text{for } i \neq 1 \end{aligned} \right\}. \quad (\text{A4})$$

This corresponds to all the population in the p state at $t = 0$.

Similarly,

$$\left. \begin{aligned} PT(1) &= 1 \\ PT(i) &= 0 \quad \text{for } i \neq 1 \end{aligned} \right\} \quad (\text{A5})$$

corresponds to a total initial probability of unity. The inputs to the program include:

- a) σ^S , the scattering cross section, which was determined in Section 6.3;
- b) n_0 , the target gas density, which is calculated from the gas kinetic expression $n_0 = p/kT$, where p and T are the target gas pressure and temperature, and k is the Boltzmann constant;
- c) v , the velocity of lithium atoms, typically 2×10^5 cm/sec;
- d) $\sigma^{\Delta l}$, a trial value;
- e) Γ_{nl} , for which decay rate of the $n = 30$ state is chosen, since this corresponds to an average n in the lithium beam; n can be changed to include the effect of the electric field.

The program first computes a factor f which is used to make sure that Δt is always = 0.1 channel, regardless of the values of $\sigma^{\Delta l}$ and σ^S . For the first interval Δt , the program enters a loop in which the change in $P(n, l, t)$ is calculated for each l , from

$\ell = 1$ to $\ell = n - 1$, and stored in $\Delta P(n, \ell, t)$. For this first calculation $\sum_{\ell'} P(n, \ell', t) = P(1)$ is used. In a second loop the calculated values of $\Delta P(n, \ell, t)$ are added to the present values of $P(n, \ell, t)$ for each ℓ to give the new $P(n, \ell, t)$, which are then summed over all ℓ to give $P(2)$, the new value of the total probability. The program then goes back to the first loop, and this time $\sum_{\ell'} P(n, \ell', t) = P(2)$. For $\Delta t = 0.1$ channel, this process is repeated 1000 times in order to get a time of flight distribution over 100 channels. Every 10th $P(t)$ value corresponds to the count rate stored in an analyzer model.

Since channel-by-channel ratios are usually required, the program repeats the above procedure for two pressures, 5 μ Torr for the base pressure and then some larger value of pressure (input b above). The program then divides the high pressure distribution by the base pressure distribution, takes the logarithms, and plots as well as prints $\ln R_p(t)$. To calculate $\ln F(t)$ by this program, one merely sets $\sigma^S = 0$. The Fortran IV program and an example of the output are shown on the following.

When similar calculations were performed with the restricted model ($\Delta \ell = \pm 1$), the resulting $\ln F(t)$ did not reproduce the experimental distributions. An example of the output from the restricted model is also shown in Figure A3. The same values of the

parameters n_o , v and Γ_{nl} were used in the restricted- and unrestricted-model calculations which yield the displayed computer plots. Even with trial values of $\sigma^{\Delta l}$ over a broad range, the restricted model does not reproduce the experimental distributions $\ln F(t)$. It is therefore reasonable to conclude that the restriction $\Delta l = \pm 1$ may not be applicable in l -changing collisions.

INPUT PARAMETERS NP, NCL, NCH, AND, BND									
3G	1001	101	.6770E+13	.1667E+12					
CONSTANTS USED ARE COL, CSCT, DT, F, SIGCSCT, SIGDL									
.9979	0.	.1000	10.02	0.			.1340E-12		
1.000	.9445	.9212	.9981	.8994	.8894	.8816	.8736	.8657	.8579
.8501	.8425	.8348	.8273	.8198	.8124	.8051	.7978	.7906	.7835
.7764	.7694	.7624	.7556	.7487	.7420	.7353	.7286	.7220	.7155
.7191	.7127	.7063	.6993	.6938	.6876	.6815	.6754	.6694	.6635
.6476	.6417	.6359	.6302	.6245	.6189	.6133	.6077	.6022	.5968
.5914	.5861	.5808	.5755	.5703	.5652	.5601	.5550	.5500	.5450
.5401	.5352	.5304	.5256	.5209	.5162	.5115	.5069	.5023	.4978
.4933	.4884	.4844	.4800	.4757	.4714	.4671	.4629	.4587	.4546
.4505	.4464	.4424	.4384	.4344	.4305	.4266	.4228	.4190	.4152
.4114	.4077	.4040	.4004	.3968	.3932	.3896	.3861	.3826	.3792
.3757									
CONSTANTS USED ARE COL, CSCT, DT, F, SIGCSCT, SIGDL									
.2457E-01	0.	.1000	407.0	0.			.1340E-12		
1.100	.9214	.8514	.7979	.7337	.6791	.6326	.5906	.5527	.5185
.4977	.4598	.4345	.4117	.3910	.3723	.3554	.3400	.3260	.3133
.3017	.2912	.2816	.2729	.2649	.2576	.2508	.2447	.2391	.2338
.2290	.2245	.2204	.2166	.2130	.2097	.2065	.2036	.2009	.1983
.1969	.1936	.1914	.1893	.1873	.1854	.1836	.1819	.1802	.1786
.1771	.1756	.1741	.1727	.1713	.1700	.1687	.1674	.1661	.1649
.1637	.1625	.1614	.1603	.1591	.1580	.1569	.1559	.1548	.1538
.1527	.1517	.1507	.1497	.1487	.1478	.1468	.1459	.1449	.1439
.1430	.1421	.1412	.1403	.1394	.1385	.1376	.1367	.1358	.1350
.1341	.1332	.1324	.1315	.1307	.1299	.1291	.1282	.1274	.1266
.1259									
LN OF CH BY CH RATIO									
0.	.2437E-01	.7882E-01	.1420	.2067	.2703	.3320	.3915	.4487	.5034
.5958	.6056	.6530	.6979	.7403	.7803	.8178	.8530	.8859	.9166
.9451	.9715	.9959	1.018	1.039	1.059	1.075	1.091	1.105	1.119
1.130	1.141	1.150	1.159	1.166	1.173	1.179	1.184	1.189	1.192
1.195	1.198	1.201	1.203	1.204	1.205	1.206	1.206	1.206	1.206
1.206	1.205	1.205	1.204	1.203	1.201	1.200	1.199	1.197	1.195
1.194	1.192	1.190	1.188	1.186	1.184	1.181	1.179	1.177	1.175
1.172	1.170	1.168	1.165	1.163	1.160	1.158	1.155	1.153	1.150
1.147	1.145	1.142	1.140	1.137	1.134	1.132	1.129	1.126	1.124
1.121	1.119	1.116	1.113	1.110	1.109	1.105	1.102	1.100	1.097
1.094									

Figure A1. A sample of the computer printout for ln F(t) calculated by the complete model.

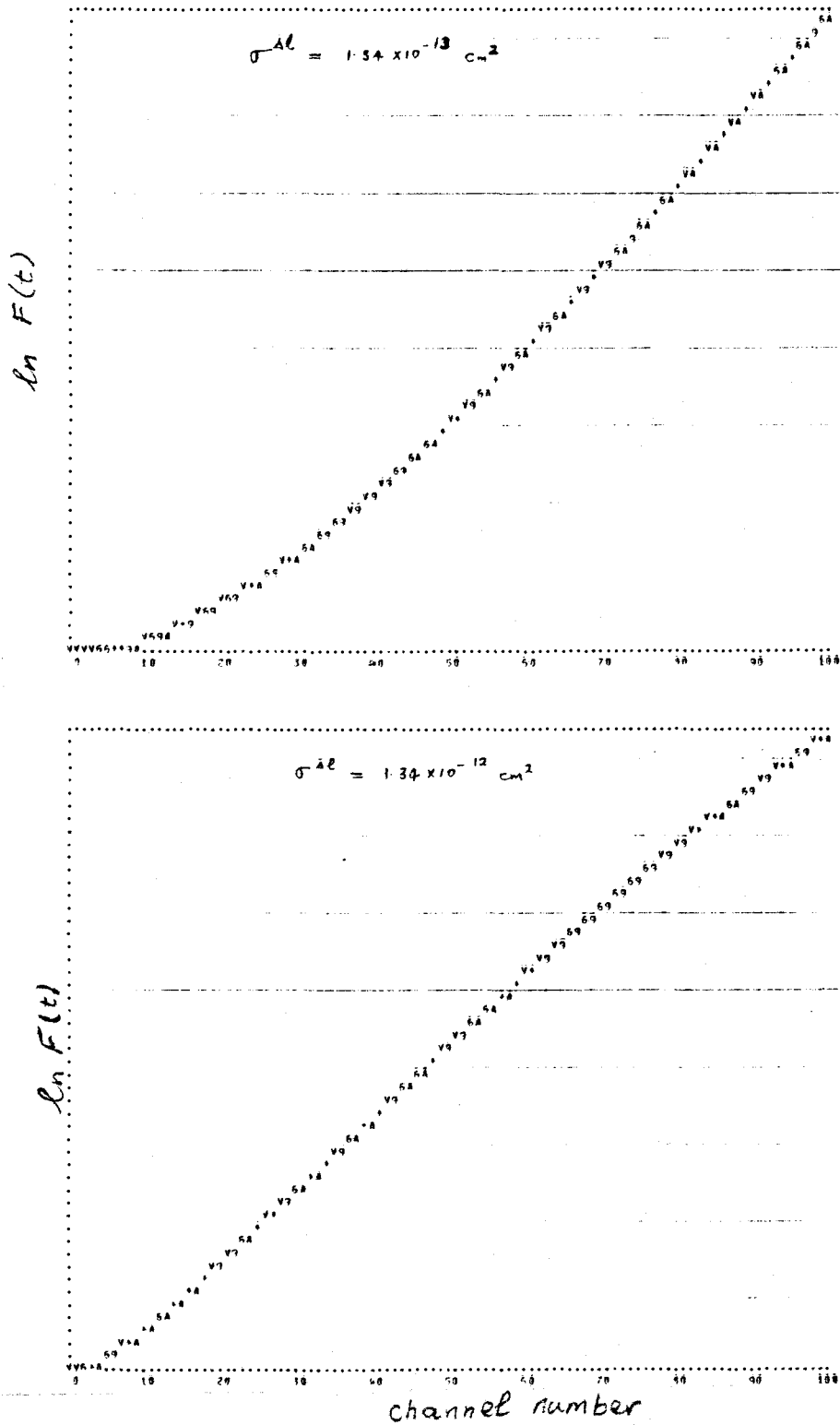


Figure A3. Computer plots of $\ln F(t)$ calculated by the restricted model. The values of the parameters (n_0, v, Γ_{nl}) used in this calculation are given in Figure A1.

```

PROGRAM XMLJ(INPUT,OUTPUT=64,TAPE60=INPUT,TAPE61=OUTPUT)
COMMON R(150),A(10001),P(10001)
WRITE(61,1113)
WRITE(61,1100)
1100  FORMAT(1X,#INPUT PARAMETERS NP,NCL,NCH,ANG,BNG#)
      READ(60,*)NP,NCL,NCH
1180  FORMAT(1X,3I10,2G1+.4)
      NGRIDS=NCL/NCH+1
      VNN=1.1
      READ(60,*)SIGSOT
      READ(60,*)ANG,BNG
      READ(60,*)SIGDL
      WRITE(61,1130)NP,NCL,NCH,ANG,BNG
      FA=10./((SIGDL+SIGSOT)*ANG*VNN)
      FB=10./((SIGDL+SIGSOT)*BNG*VNN)
      CALL XMLJMP(A,ANG,SIGDL,SIGSOT,NP,FA,NCL)
      WRITE(61,1130)(A(I),I=1,NCL,NGRIDS)
      CALL XMLJMP(B,BNG,SIGDL,SIGSOT,NP,FB,NCL)
      WRITE(61,1130)(B(I),I=1,NCL,NGRIDS)
1130  FORMAT(1X,10G11.4)
      K=0
      DO 1140 I=1,NCL,NGRIDS
      K=K+1
      R(K)=ALOG(A(I)/B(I))
1140  CONTINUE
      WRITE(61,1150)
1150  FORMAT(1X,#LN OF CH BY CH RATIO#)
      WRITE(61,1160)(R(I),I=1,NCH)
1160  FORMAT(1X,10G11.4)
      WRITE(61,1170)
1170  FORMAT(1H1)
      CALL MINMAX(R,RMIN,RMAX,NCH)
      CALL DTPLCT(R,50,NCH,50,NCH,RMIN,RMAX)
1113  FORMAT(1H1)
      WRITE(61,1113)
      STOP
      END

```

```

SUBROUTINE XMLJMP(PT,XN0,SIGDL,SIGSCT,NP,F,NCL)
DIMENSION CPLT(50),PLT(50),PT(1000)
DO 700 I=2,50
700  PLT(I)=0.
    DC 701 I=2,NCL
701  PT(I)=0.
    PLT(1)=1.
    PT(1)=1.
    VN=1.1
    CDL=XN0*SIGDL*VN
    CSCT=XN0*SIGSCT*/N
    G0=1.0235E05/(NP**2.44)
    NPSQ=NP**2
    DT=1./(F*(CDL+CSCT))
    LMAX=NP-1
    WRITE(61,705)
705  FORMAT(1X,'CONSTANTS USED ARE CDL,CSCT,DT,F,SIGSCT,SIGDL')
    WRITE(61,706)CDL,CSCT,DT,F,SIGSCT,SIGDL
706  FORMAT(1X,'6G14.4')
    DO 702 IT=2,NCL
    DO 703 L=1,LMAX
    GL=(2*L+1)*CDL/NPSQ
    GAMAL=CDL+CSCT+G0/((L+8.43)**2.36)
    DPLT(L)=(GL*PT(IT-1)-GAMAL*PLT(L))*DT
703  CONTINUE
    DO 704 L=1,LMAX
    PLT(L)=PLT(L)+DPLT(L)
    PT(IT)=PT(IT)+PLT(L)
704  CONTINUE
702  CONTINUE
    RETURN
    END

```

```

SUBROUTINE MINMAX(DAT, DATMIN, DATMAX, N1)
DIMENSION DAT(101)
DATMAX=DAT(1)
DATMIN=DAT(1)
DO 601 I=2,N1
601  DATMAX=AMAX1(DATMAX,DAT(I))
    DATMIN=AMIN1(DATMIN,DAT(I))
RETURN
ENC

```

```

SUBROUTINE DTPLOT(DAT, IV, IH, IDV, ICH, CATMIN, DATMAX)
DIMENSION A(135), DAT(150), IW(135), IC(135), SYMBOL(6)
DIMENSION AXLAB(11)
DATA (AXLAB=0,10,20,30,40,50,60,70,80,90,100)
DATA (SYMBOL=#V#, #6#, #+#, #9#, #A#, #.#)
DATA (BLANK=# #)
DELDAT=DATMAX-DATMIN
XIV=FLCAT(IV)-0.000001
DO 200 I=1,IH
200  IW(I)=TEMP=(DAT(I)-DATMIN)*XIV/(DELDAT)+1
    IC(I)=(TEMP-IW(I))*5.+1.
    IVP=IV+1
    DO 504 J=1,IVP
    K=IVP-J+1
    DO 503 I=1,IH
    A(I)=BLANK
    IF(MOD(K, IDV).EQ.1) A(I)=SYMBOL(6)
    IF(MOD(I, ICH).EQ.1) A(I)=SYMBOL(6)
    IT=IC(I)
    IF(IW(I).EQ.K) A(I)=SYMBOL(IT)
503  CONTINUE
    PRINT 630, (A(L), L=1, IH)
504  CONTINUE
600  FORMAT(2X,131A1)
    PRINT 1090, AXLAB
1090  FORMAT(1X,11(I3,7X))
RETURN
ENC

```